Doctoral Dissertation

In-situ transmission electron microscopy observation of fracture process in multilayer MoS_2 films

XIONG Wei

Supervisor: Yoshifumi Oshima

Graduate School of Advanced Science and Technology

Japan Advanced Institute of Science and Technology

[Materials Science]

September 2025

Preliminary defenses: 5th, June, 2025

Final defenses:

Degree conferral:

Reviewers

Yoshifumi Oshima (JAIST)

Yukiko Takamura (JAIST)

Toshu An (JAIST)

Kenta Hongo (JAIST)

Jiaqi Zhang (Zhengzhou University)

Abstract

In-situ transmission electron microscopy observation of fracture process in multilayer MoS_2 films

XIONG Wei

s2120421

Mechanical strain plays a pivotal role in modulating both the structural and electronic properties of two-dimensional (2D) materials. While small, controlled strains are widely utilized to tune functionalities such as bandgap and carrier mobility, such minor deformations are insufficient for probing the intrinsic mechanical response and failure mechanisms of atomically thin materials. In particular, the understanding of fracture behavior under uniaxial tensile stress at the atomic scale remains incomplete, largely due to limitations in experimental techniques that can simultaneously provide mechanical control and atomic-resolution imaging. In this study, we address these challenges by developing an integrated in situ transmission electron microscopy (TEM) tensile testing platform and applying it to the fracture investigation of few-layer molybdenum disulfide (MoS_2) nanosheets.

Our work begins with a comprehensive assessment of existing experimental approaches and the identification of key limitations in current tensile testing methods for 2D materials. To enable high-stability mechanical testing under TEM, we first constructed a dedicated *in situ* experimental system comprising a JEOL 2100Plus TEM equipped with a custom-built tensile holder. This holder features a piezoelectric actuator and a titanium support plate to enable voltage-controlled tensile displacement with sub-nanometer accuracy.

Recognizing the instability of conventional tensile chips, such as those relying on independent silicon fragments, we designed a new tensile chip architecture based on a monolithic silicon frame integrated with a SiN_x observation window. A key feature of our design is the introduction of long, narrow slits on the SiN_x membrane, which localize strain and improve stress uniformity within the imaging region. Finite element simulations and in situ performance validation confirmed the linear displacement behavior and mechanical robustness of the platform. Additional improvements, such as the implementation of T-shaped termini and the minimization of out-of-plane movement, further enhanced the reliability of atomic-resolution deformation tracking.

High-quality few-layer MoS_2 samples were prepared via modified mechanical exfoliation using PDMS, followed by a dry-transfer process facilitated by a PPC/PDMS stamp. We adopt contrast-thickness calibration protocol using optical microscopy (OM), atomic force microscopy (AFM), and Raman spectroscopy, allowing for real-time layer number identification during sample manipulation. Moreover, we introduced a practical method for determining the crystallographic zigzag (ZZ) edge orientation of MoS_2 flakes by correlating natural edge morphology with optical and TEM observations. This orientation calibration was critical for exploring the anisotropic fracture behavior of MoS_2 under uniaxial strain.

Using the custom tensile platform, we performed a series of in situ stretching experiments on few-layer MoS_2 nanosheets with controlled orientations and thickness. Our observations revealed a striking deviation from the brittle fracture behavior typically associated with 2D materials. Specifically, samples stretched along directions near the armchair (AC) axis exhibited clear signatures of ductile fracture, including stepped edge morphologies, irregular crack fronts, and sustained compressive strain near crack tips. These features were observed consistently across multiple samples and were supported by GPA-based strain mapping, which revealed localized strain bands

and interlayer sliding regions indicative of energy dissipation during deformation.

One of the most remarkable findings of this study is the consistent formation of ~10 nm-wide stepped fracture zones, which emerged during the near AC direction uniaxial tensile failure of few-layer MoS_2. These characteristic fracture regions suggest that crack propagation occurs along distinct paths. The fracture morphology further supports a scenario where cracks propagate preferentially along the ZZ direction, consistent with theoretical predictions of lower fracture energy along this direction. Similar ductile features were also observed in MoS_2 samples stretched along the ZZ orientation at low strain rates, reinforcing the generality of the observed behavior.

In addition to crack initiation and propagation, we identified the role of pre-existing structural features, such as holes and pre-cracks generated during the pre-straining process, as fracture precursors. These defects influenced the stress field and promoted crack nucleation, especially in regions characterized by ripple-like stress distributions formed propagated along two AC directions away from tensile axis. These intersecting ripples exhibit a periodicity of approximately 10 nm, which accounts for the formation of alternating stripes with ~10 nm spacing and varying contrast observed after the pre-strain treatment.

In summary, this study presents a comprehensive framework for investigating fracture mechanics in 2D materials at the atomic scale. By developing a stable, precise, and orientation-calibrated *in situ* TEM tensile testing platform, we successfully visualized the dynamic evolution of fracture processes in few-layer MoS_2. Our findings challenge the conventional view of 2D materials as inherently brittle and instead reveal a ductile failure mechanism characterized by stepwise fracture zones, interlayer sliding, and stress field redistribution. These insights not only deepen our understanding of mechanical failure in 2D systems but also provide practical guidance for designing mechanically robust nanoelectronic and optoelectronic devices based on van der Waals materials.

KEYWORDS: few layers 2H-MoS_2 nanosheet, tensile loading, ductile fracture, real-time *in situ* TEM, atomic resolution

Table of Contents

Chapter 1 background

Introduction

Mechanical strain significantly affects both the structural and electronic properties of 2D materials. While small strains are commonly used to enhance device performance, such limited deformation makes it difficult to fully understand the intrinsic mechanical response of the material and fracture behavior.

In this chapter, we will introduce the background of our research on nanoscale fracture mechanics of MoS_2 and recent progress on related topics, such as micro-/nano-scale mechanics of 2D materials.

1.1 Brief introduction to MoS_2

The crystalline MoS_2 is formed as a layer structure. To monolayer MoS_2 crystal, it contains three layers of atoms, that is S atoms, Mo atoms and S atoms. The molybdenum atoms are sandwiched between the atoms of sulfide on both sides. Three motifs of MoS_2 structure are most commonly reported, they are 2H, 1T, and 3R.[1] The numbers in 2H, 1T, and 3R indicate the number of layers per unit cell, while the letters H, T, and R describe the lattice symmetry, corresponding to hexagonal, tetragonal, and rhombohedral, respectively. MoS_2 can crystallize into two primary coordination geometries: trigonal prismatic and octahedral. The trigonal prismatic coordination yields the 2H and 3R motifs, both of which are semiconducting, as shown in Figure 1.1(a) and (c), respectively. These atomic models were constructed using VESTA. In contrast, the octahedral coordination forms the 1T motif, which is metallic, as depicted in Figure 1.1(b). Thus, the 2H and 3R phases exhibit semiconducting behavior, while the 1T phase is metallic.[2] The most stable state at room temperature is the 2H motif, which we investigated in this work.

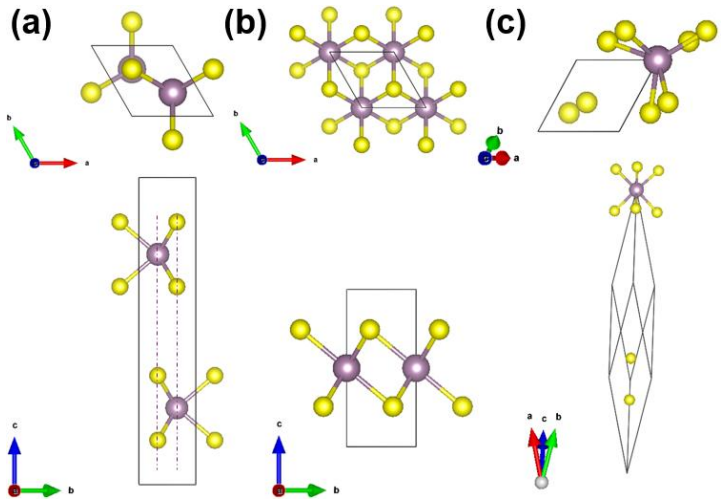

Figure 1.1 (a)-(c) The atomic structure 2H, 1T and 3R phase of MoS_2, respectively. Upper: the top view;

bottom: the lateral view.

Figure 1.2 shows the bilayer structure of 2H-MoS_2, which belongs to the $P6_3/mmc$ space group. This symmetry yields a structure that is repeatable every 60°, indicating its sixfold rotational symmetry. Because the properties of 2H-MoS_2 strongly depend on its edge configurations[3], it is important to investigate the fracture behavior along different edge types (armchair (AC) and zigzag (ZZ) directions) to better understand the material's edge-dependent mechanical response.

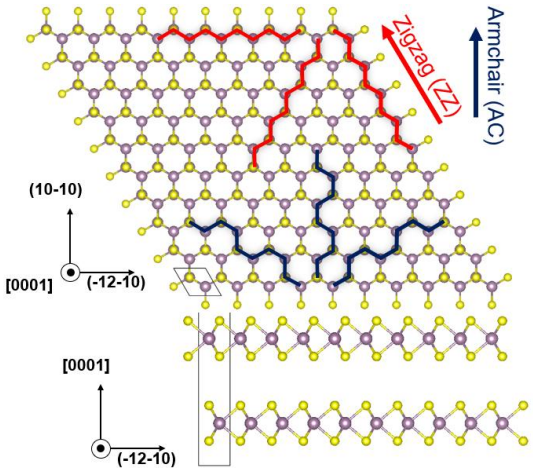

Figure 1.2 Bilayer 2H-MoS_2 structure

1.2 Strain induced properties changing in 2D materials

Since graphene was successfully prepared by mechanical exfoliation in 2004[4], two-dimensional (2D) materials have attracted significant attention in the past two decades due to their outstanding optical, magnetic, mechanical, and thermal properties[5,6]. Their atomically thin geometry, high carrier mobility, field-effect switching ratio, and mechanical flexibility make them ideal for applications ranging from nanoscale field-effect transistors (FETs)[7] to flexible

and transparent electronics[8] or digital logic transistors[9]. In practical applications, the intrinsic properties of 2D materials play a critical role in determining device stability. Therefore, to meet growing demands and broaden their application scope, a thorough understanding of their intrinsic elastic behavior, deformation characteristics, and fracture mechanisms is essential[10]. Extensive efforts have been devoted to understanding the intrinsic mechanical properties of 2D materials, with a growing number of studies reported each year[11,12].

In addition to their mechanical characteristics, the electronic properties of 2D materials also play a crucial role in determining their performance in electronic devices. Key parameters such as bandgap, carrier density, and mobility directly influence device functionality and efficiency. Notably, the electronic properties of 2D materials are highly sensitive to external strain, with mechanical deformation capable of inducing significant changes in both crystal symmetry and electronic band structure. Li et al. reveals that strain effectively tunes the electronic properties of graphene and GNRs by modulating Dirac points, bandgaps, and edge states, as shown in Figure 1.3(a)[13]. Two years later, Scalise et al. found that the bandgap of the MoS_2 was reported to reduce with applied tensile strain , as shown in Figure 1.3(b)[14]. These strain sensitivity highlights the importance of understanding their mechanical behavior, which plays a crucial role in optimizing device performance and informing structural design.

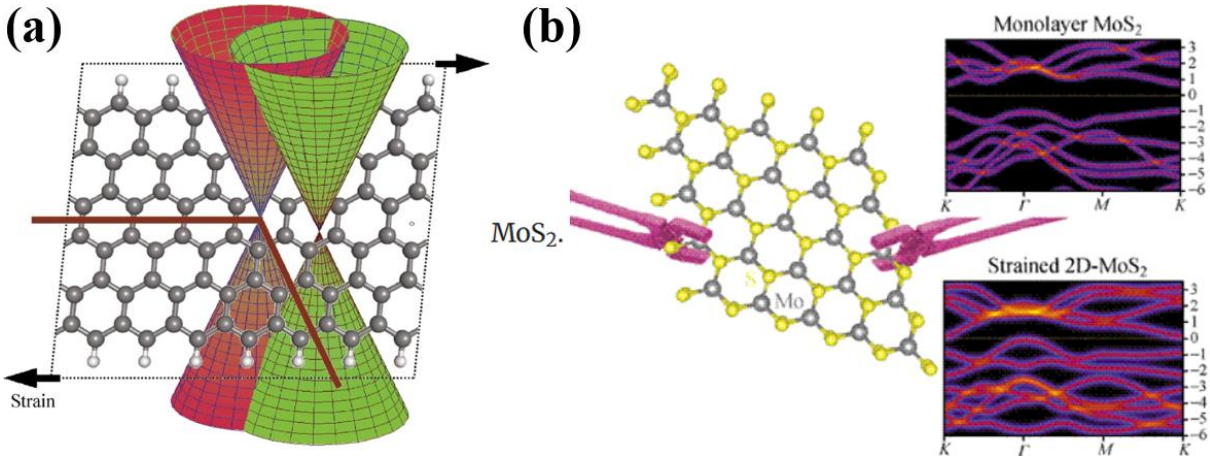

Figure 1.3 (a) Dirac cone shift in graphene under shear strain[13]. (b) Strain-induced band structure modulation in monolayer MoS_2[14].

Among various families of 2D materials, transition metal dichalcogenides (TMDs), especially for MoS_2, have emerged as a particularly promising class due to their intrinsic semiconducting properties and tunable band structures, which have been widely applied in semiconductor devices. Recent studies have demonstrated its potential in various scenarios. For instance, MoS_2-based field-effect transistors (FETs) exhibit strain-enhanced carrier mobility and tunable threshold voltages[7,15,16], as can be seen in Figure 1.4. Making them promising candidates for next-generation logic circuits.

Nevertheless, the strain applied in practical device applications is typically limited to small ranges to maintain operational reliability. This constraint hinders a comprehensive understanding of the material's behavior under large deformation, particularly near the limits of elasticity and fracture. Investigating the mechanical and electronic responses of MoS_2 under higher strain levels is thus crucial for advancing both fundamental research and the development of more robust, strain-adaptive devices.

Due to MoS_2 is the most widely studied and applied material for its moderate bandgap,

strong environmental stability, and compatibility with large-scale device fabrication, so we chose it as our main research object.

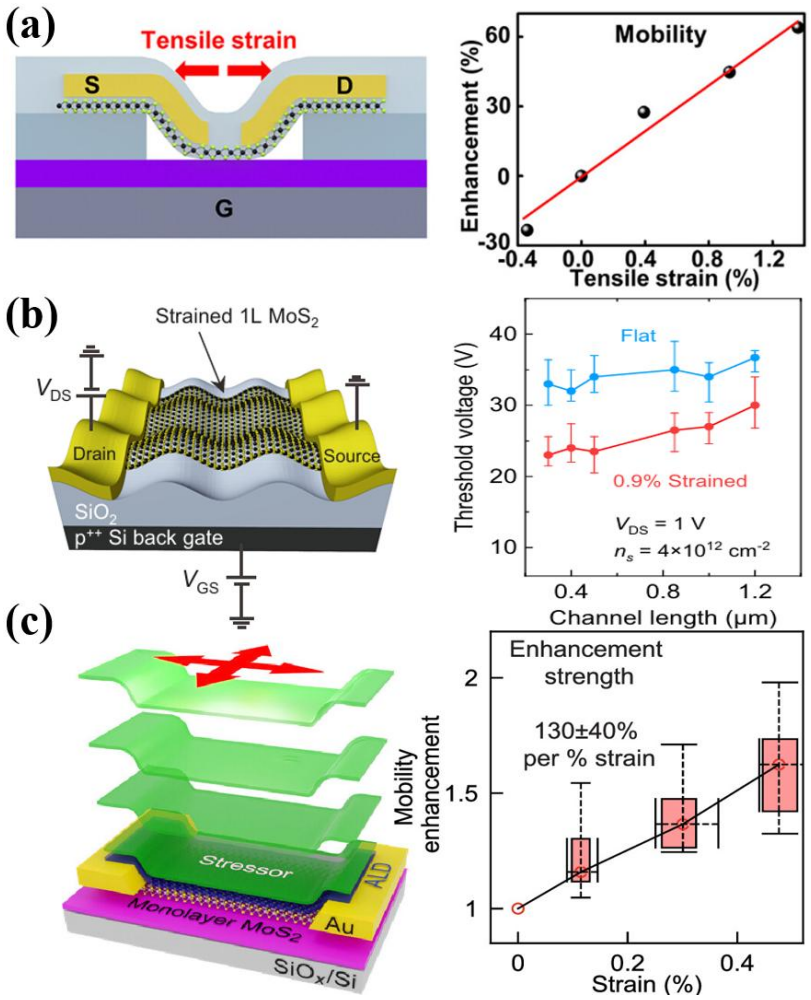

Figure 1.4 Strain-engineered monolayer MoS_2 devices and corresponding electrical performance enhancement. (a) Schematic of a field-effect transistor (FET) under tensile strain and the resulting improvement in carrier mobility with increasing strain. (b) Device layout showing strained monolayer MoS_2 and the threshold voltage shift under strain compared to flat devices. (c) Layered structure for applying controlled biaxial strain and the corresponding enhancement in carrier mobility, showing a linear increase with strain up to 0.5%.

1.3 Approaches on stress regulation and fracture studies in 2D materials

Understanding how two-dimensional (2D) materials respond to mechanical stress and ultimately fracture is critically important for both fundamental research and practical applications. Over the past decade, a variety of experimental techniques and theoretical simulations have been developed to regulate and analyze stress in 2D systems—not only to tune their physical properties, but also to explore their fracture mechanisms under extreme loading and simulated conditions[14,17,18].

1.3.1 Theoretical and simulation studies on stress engineering and fracture mechanisms in 2D materials

Theoretical and computational studies have played a crucial role in deepening our understanding of how 2D materials respond to stress and ultimately fracture. These approaches offer atomic-level insights that are often inaccessible by direct measurement, enabling precise analysis of deformation behavior, energy evolution, and defect dynamics under a wide range of conditions[19–21].

One of the major focuses in this area is strain engineering, where first-principles calculations (such as density functional theory, DFT)[22–24] have been extensively used to investigate how mechanical deformation influences the band structure[14] and mobilities[25]. As shown in Figure 1.5. These studies have revealed, for instance, that uniaxial or biaxial strain can induce direct-to-indirect bandgap transitions in TMDs, tune effective masses, and enhance carrier mobilities — effects that are vital for the design of next-generation flexible electronics.

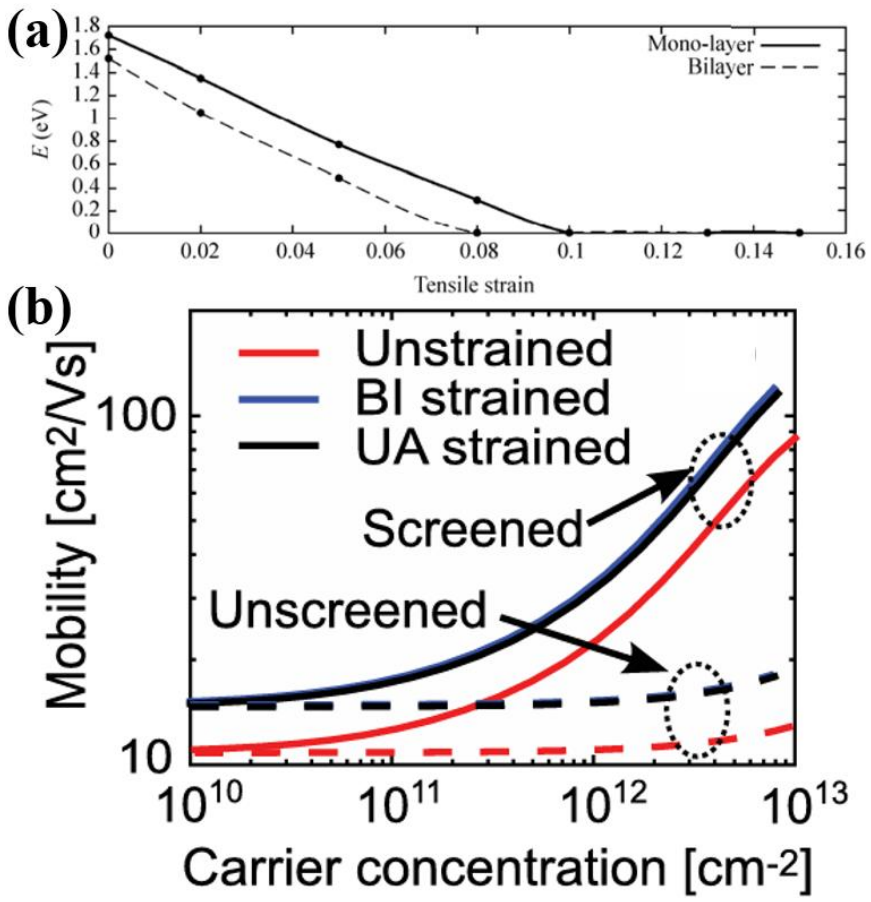

Figure 1.5 (a) Plots of energy band gap (E_g) versus applied strain for mono- and bi-layer MoS_2.[14] (b) The mobility versus carrier concentration with and without screening for the unstrained MoS_2, for a tensile biaxial strain of 5%, and for a uniaxial strain of 5% along the armchair direction.[25]

In addition, molecular dynamics (MD) and finite element simulations have become powerful tools for modeling the mechanical response of 2D materials under tensile or compressive loads[18,26,27]. By simulating atomistic interactions, MD simulations can reproduce the stress-strain behavior[18,28] and crack initiation[17,26]. As the related results described in Figure 1.6.

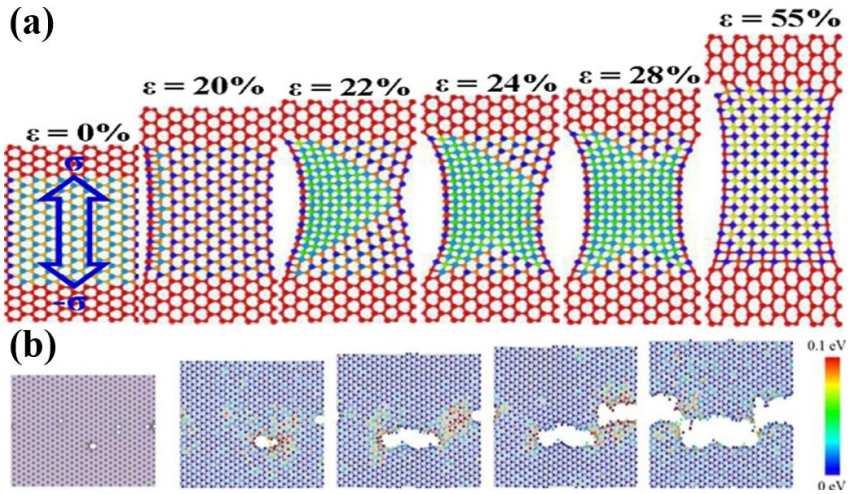

Figure 1.6 (a) Typical atomic configurations of the SLMoS_2 nanosheets with different widths under tensile loading along the zigzag direction.[18] (b) Phenomenological modeling of fracture surface propagation in the monolayer MoS_2 nanosheet of voids nucleation and growth in the small-defects specimen.[26]

Together, these computational efforts complement experimental studies and provide valuable guidance for interpreting observed phenomena, optimizing material design, and predicting failure modes under extreme mechanical environments.

1.3.2 Experimental approaches for stress regulation and fracture studies in 2D materials

To gain deeper insights into the mechanical behavior of 2D materials—particularly their stress response and fracture mechanisms—various experimental strategies have been continuously developed and refined over the past decade. One common approach is to introduce strain during synthesis, for instance, by using chemical vapor deposition (CVD) on lattice-mismatched substrates, which generates intrinsic strain within the grown material[29]. Post-growth modifications, such as doping, defect engineering, or heteroatom substitution, can also create localized stress fields and influence crack nucleation and mechanical robustness[30]. These methods induced built-in strain during the growth of the sample, as depicted in Figure

1.7. Despite these methods effectively induced built-in strain into the prepared samples, it still hard to refrain from the effect of substrate or the grain boundary, which are harmful for the thoroughly understood of the intrinsic properties of the strained samples.

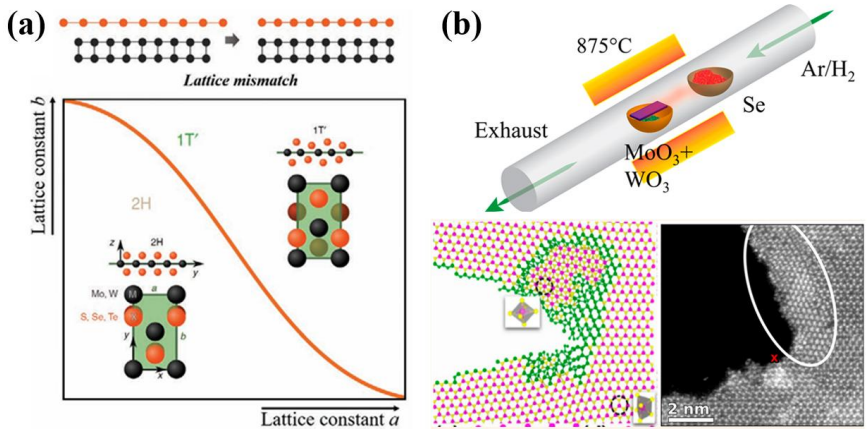

Figure 1.7 (a) Strain caused by lattice mismatch. For a TMD monolayer, its lattice parameters a and b by the growth substrate can be used to select a particular phase of the TMD monolayer.[29,31] (b) Schematic of CVD growth 2D $MoWSe_2$ alloy and the 2H-1T phase transformation as the crack propagates through the $MoSe_2/WSe_2$ alloy.[30]

In addition to synthesis-related methods, substrate-induced and support-assisted strain regulation provides another widely used means of stress control. Transferring 2D materials onto designed patterned[32,33], stretchable or thermally mismatched substrates allows for strain application via substrate bending[34], thermal expansion[35], or deliberate deformation patterns, such as wrinkling or delamination[32,33,36,37]. These methods are relatively easy to implement and provide useful insights into how deformation affects material stability, although the applied strain is often non-uniform and limited in magnitude and cannot avoid the interaction between the stretched sample and the affiliated substrate, making it challenging to probe fracture mechanism under extreme conditions.

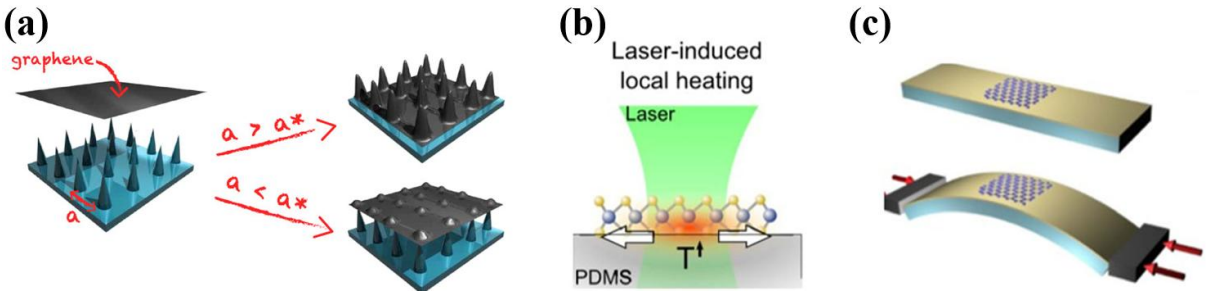

Figure 1.8 (a) Illustration of graphene tents formed by depositing onto a SiO_2 nanopillar array.[33] (b) Schematic picture of laser-induced local heating.[35] (c) 3D diagram of two-point bending apparatus.[34]

To more directly explore fracture mechanisms, experimental methods such as atomic force microscopy (AFM) nanoindentation[38–40] and micro-indenter testing[41,42] have been employed to evaluate localized stress response and fracture toughness. As illustrated in Figure 1.9.

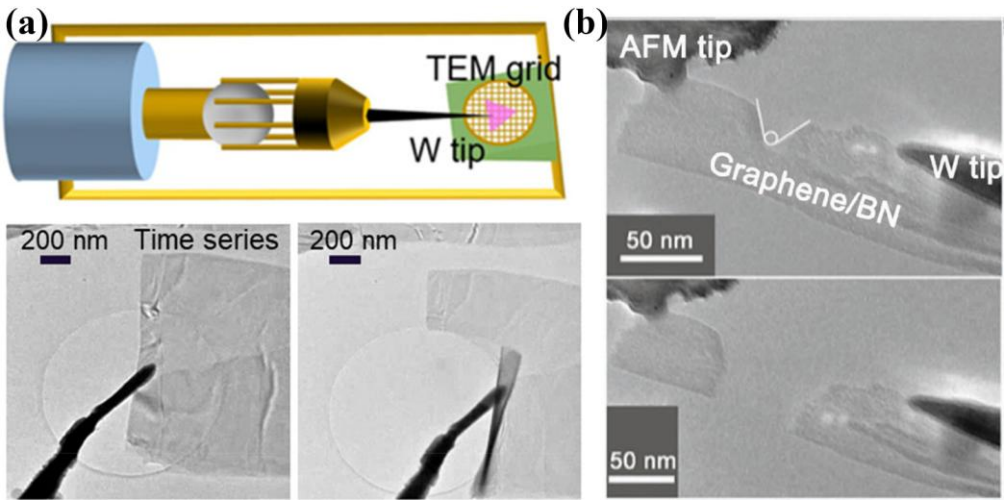

Figure 1.9 (a) Schematic showing the experimental set up for the *in situ* TEM deformation tests and InSe crystals before (down left) and after (dawn right) the *ex situ* compression test.[41] (b) Fracture toughness of graphene measured with a nanomanipulator controlled W tip and AFM cantilever.[40]

Furthermore, tensile testing using MEMS-based devices, such as push-to-pull (PTP) platforms[43–45] or custom-fabricated stretchable systems[46,47] enables uniform strain application and direct observation of stress–strain responses[28,48], crack propagation[17,43,49], and the ultimate fracture strength[17,43,48]. These techniques are often coupled with in situ imaging methods, such as electron microscopy (EM), to allow tracking of crack propagation. Despite these advances,

challenges remain challenges in achieving real-time recorded atomic resolution high-quality stretching induced fracture results, which limits our understanding of the fracture process at the atomic level.

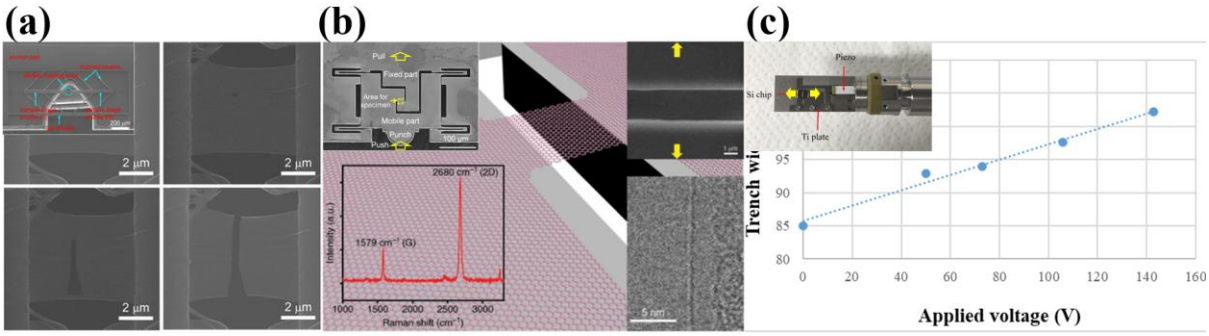

Figure 1.10 (a) SEM image of a nanomechanical device and SEM images showing the crack initiation, propagation, and fracture process of $MoSe_2$[43]. (b) Schematic showing a single-crystalline graphene sample sus pended over the push-to-pull (PTP) micromechanical device. Left top is an SEM image showing an overview of the PTP device actuated by an external pico-indenter.[45] Right top, zoom-in SEM image taken from the region marked by a rectangle in the left-top inset. The yellow arrows indicate the indentation or stress loading direction. Left-bottom inset showing a Raman spectrum taken from the graphene sample. Right-bottom inset showing a TEM bright-field image taken from the sample edge, where an amorphous edge can be observed.[44] (c) Top-view of the custom-fabricated stretchable systems and its stretch ability.[46,47]

1.3.3 Limitations of current studies on tensile fracture of 2D materials

Despite significant progress in both experimental and theoretical studies, our understanding of tensile fracture mechanisms in 2D materials, particularly at the atomic scale, has remained limited.

Most existing experimental investigations have been conducted using techniques such as scanning electron microscopy (SEM) and atomic force microscopy (AFM). While AFM offers atomic-scale resolution in ideal conditions and has proven valuable for mapping strain fields, surface topography, and mechanical properties at the nanoscale, its application to fracture

studies remains highly challenging. This is mainly due to the difficulty in directly observing dynamic fracture processes and the limited ability to resolve real-time structural evolution during crack nucleation and propagation.

On the other hand, SEM provides clear morphological information but lacks the atomic resolution necessary to capture atomic-level changes. TEM-based studies, which are capable of resolving atomic structures, have also been explored. However, many such studies do not involve true *in situ* tensile deformation. Instead, stress is often applied indirectly—using AFM tips for nanoindentation, mechanical probes, or focused electron beam irradiation—which may not accurately replicate the tensile fracture behavior under uniform loading conditions.

Although some progress has been made using in situ TEM setups, fully capturing the fracture process at atomic resolution during tensile loading remains technically demanding. These experiments require precise strain control, mechanical stability, and high imaging resolution simultaneously, which poses considerable challenges.

In summary, while tools like AFM and TEM have advanced our ability to probe 2D materials, direct atomic-scale observations of fracture under controlled in situ tensile loading are still scarce. Bridging this gap is essential for a deeper understanding of failure mechanisms in 2D materials and for the reliable design of strain-engineered nanodevices.

1.4 Approaches on fracture studies in 2D materials

1.4.1 Fracture mechanism in 2D materials

Since the PTP device was first used for the tensile study of 2D materials in the 2010s[50], in-situ studies of the tensile process have never stopped. As reported by Li *et al.* in 2017[26], the fracture behavior of multilayer MoS_2 evolves from intraplanar to interplanar as the thickness increases, as shown in Figure 1.11. The basic mechanism of the fracture can be explained as follows:

In monolayer or few-layer samples, fracture occurs through simultaneous rupture of all atomic layers (intraplanar). In contrast, thicker flakes tend to fail along pre-existing or defect-induced interlayer interfaces, leading to interplanar fracture and significant stress dissipation. For intermediate nanosheet thicknesses, a combination of both mechanisms is observed. Notably, despite the distinct fracture origins, both the intermediate and thicker flakes exhibit sudden brittle fracture, suggesting that once a critical stress condition is met, the final rupture proceeds rapidly, irrespective of whether the failure path is intraplanar, interplanar, or mixed.

This fracture mechanism is also the mainstream fracture mechanism at present. Similar results were achieved in $MoSe_2$[43] and Ta_2NiSe_5[48]. The fracture process was characterized by brittle fracture, where the fracture showing smooth and straight fracture shape, all layers rupture together and fractured with a sudden energy release.

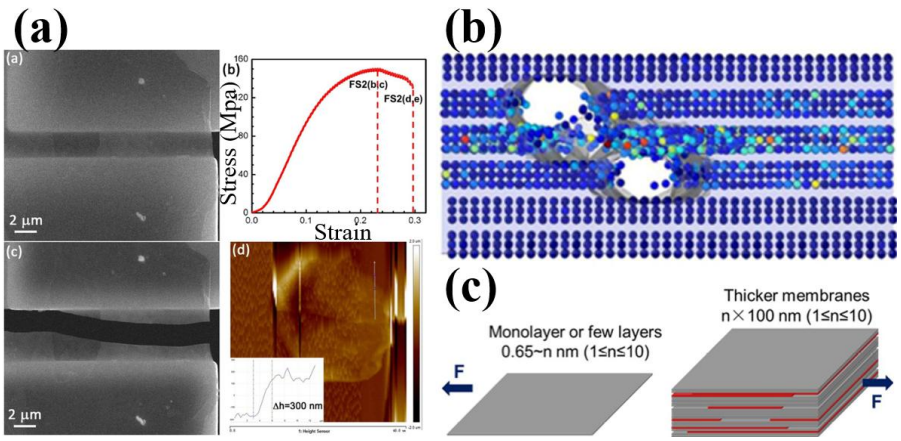

Figure 1.11 (a) Fracture in MoS_2 flakes with the tensile rate of 15 nm/s. (b) Intraplanar fracture mode in MoS2 flakes. (c) Interplanar fracture mode in MoS_2 flakes.

1.4.2 Ductile-like fracture process in 2D materials

In MoS_2, crack propagation has been studied using focused electron beams to introduce holes, from which branch cracks were observed to initiate and grow.

These results show that fracture in MoS_2 is typically brittle, with sharp crack tips and clean cleavage. However, by introducing defects, the fracture mode can be engineered toward ductile-like behavior, featuring blunt, split, or irregular tips, often initiated at pores or edge defects, and exhibiting crack deflection, branching, or rough edges[38,51].

Interestingly, even h-BN, which is traditionally considered a brittle 2D material, was found to exhibit surprisingly stable crack propagation with deflected and rough edges (intrinsic toughening), at a tensile rate of around 5 nm/s[17]. As depicted in Figure 1.12. It is worth noting that the tensile rate is very low, which makes us wonder whether low tensile strain rate will lead to different fractures.

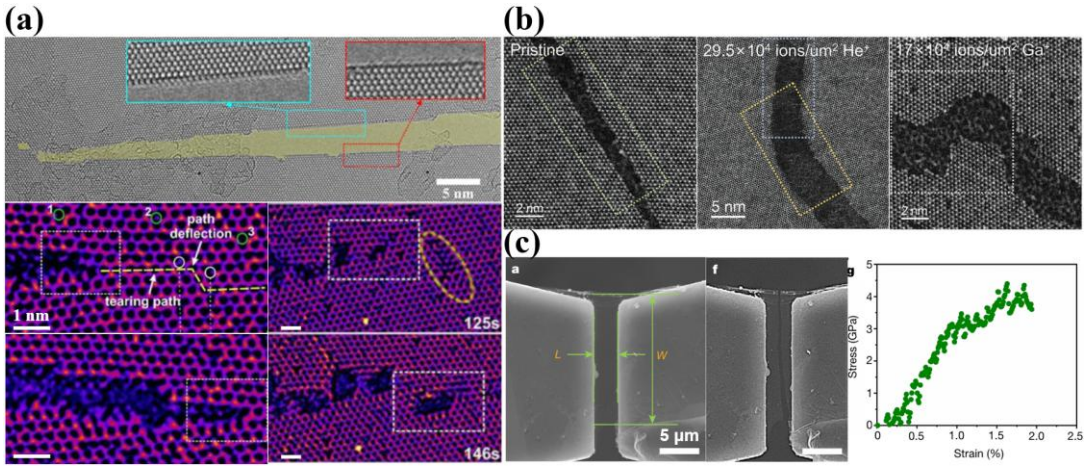

Figure 1.12 (a) and (b) Defect engineered fracture behavior from brittle to ductile-like.[38,51] (c) Intrinsic toughening in monolayer h-BN.[17]

1.5 Objectives and Scope of This Study

As discussed in the previous sections, significant advances have been made in exploring the mechanical and electronic properties of 2D materials, particularly under strain. However, current approaches face limitations in capturing the fracture behavior of 2D materials at the atomic scale under true uniaxial tensile loading conditions. In particular, a detailed, atomic-level understanding of crack initiation and propagation in transition metal dichalcogenides (TMDs) such as MoS_2 remains lacking.

In this study, we aim to address these challenges by developing an integrated *in situ* tensile testing platform that enables direct observation of MoS_2 fracture at atomic resolution under controlled loading. The main objectives of this work are:

1. To establish a reliable methodology for *in situ* tensile testing of 2D materials at the atomic scale, combining high-resolution transmission electron microscopy (HRTEM)

imaging with a stable and controllable uniaxial strain loading mechanism.

2. To implement a full-dry transfer process for MoS_2 that enables precise layer-number selection and crystalline orientation control, ensuring consistent sample quality for mechanical testing.

3. To investigate the fracture behavior of MoS_2 nanosheets, including crack initiation, propagation paths, and their correlation with crystallographic directions and defects.

This work aims to provide a more comprehensive understanding of the fracture behavior of MoS_2 under uniaxial tension.

Conclusion

In this chapter, we provided an overview of the motivation and current status of mechanical and fracture studies in two-dimensional (2D) materials, with a particular focus on MoS_2. We first introduced the fundamental properties of 2D materials and their critical role in next-generation electronic and optoelectronic devices. Special attention was given to strain-sensitive properties such as bandgap modulation and carrier mobility, which highlight the need for precise mechanical control and characterization.

We then reviewed recent experimental and theoretical strategies for stress regulation and fracture investigation in 2D materials. Although significant progress has been made in manipulating stress and probing mechanical responses, current studies still face limitations in capturing fracture behavior at the atomic scale, especially under real-time with *in situ* uniaxial loading, leaving a gap in our understanding of the intrinsic failure mechanisms of 2D materials.

Additionally, in MoS_2, fractures are typically brittle with sharp, clean cracks. However, defects can induce ductile-like features such as crack deflection and rough edges. Similarly, h-BN, normally brittle, also exhibits stable, deflected crack propagation at a low strain rate (~5 nm/s), suggesting that lowering the strain rate may also encourage tougher fracture behavior in 2D materials.

Finally, we outlined the objectives of this work, which aims to develop an improved in situ tensile testing method, implement a controlled sample preparation process, and explore the atomic-scale fracture mechanisms of MoS_2. This study seeks to bridge the current gap between

macroscopic mechanical characterization and atomic-level understanding, thereby advancing the fundamental knowledge required for the rational design of robust 2D devices.

References

1. Song, I., Park, C. & Choi, H. C. Synthesis and properties of molybdenum disulphide: from bulk to atomic layers. *RSC Adv.* **5**, 7495–7514 (2015).
2. Wypych, F. & Schöllhorn, R. 1T-MoS_2 , a new metallic modification of molybdenum disulfide. *J Chem Soc Chem Commun* 1386–1388 (1992) doi:10.1039/C39920001386.
3. Pan, H. & Zhang, Y.-W. Tuning the Electronic and Magnetic Properties of MoS_2 Nanoribbons by Strain Engineering. *J. Phys. Chem. C* **116**, 11752–11757 (2012).
4. Novoselov, K. S. *et al.* Electric Field Effect in Atomically Thin Carbon Films. *Science* **306**, 666–669 (2004).
5. Manzeli, S., Ovchinnikov, D., Pasquier, D., Yazyev, O. V. & Kis, A. 2D transition metal dichalcogenides. *Nat. Rev. Mater.* **2**, 17033 (2017).
6. Wang, Q. H., Kalantar-Zadeh, K., Kis, A., Coleman, J. N. & Strano, M. S. Electronics and optoelectronics of two-dimensional transition metal dichalcogenides. *Nat. Nanotechnol.* **7**, 699–712 (2012).
7. Liu, X. *et al.* Deterministic grayscale nanotopography to engineer mobilities in strained MoS2 FETs. *Nat. Commun.* **15**, 6934 (2024).
8. Singh, E., Singh, P., Kim, K. S., Yeom, G. Y. & Nalwa, H. S. Flexible Molybdenum Disulfide (MoS_2) Atomic Layers for Wearable Electronics and Optoelectronics. *ACS Appl. Mater. Interfaces* **11**, 11061–11105 (2019).
9. Radisavljevic, B., Radenovic, A., Brivio, J., Giacometti, V. & Kis, A. Single-layer MoS2 transistors. *Nat. Nanotechnol.* **6**, 147–150 (2011).

10. Ji, H., Song, Z., Wu, A., Zou, Y.-C. & Yang, G. Recent advances in the fundamentals and *in situ* characterizations for mechanics in 2D materials. *Nanoscale* **17**, 7574–7599 (2025).

11. Mounet, N. *et al.* Two-dimensional materials from high-throughput computational exfoliation of experimentally known compounds. *Nat. Nanotechnol.* **13**, 246–252 (2018).

12. Desai, S. B. *et al.* MoS_2 transistors with 1-nanometer gate lengths. *Science* **354**, 99–102 (2016).

13. Li, Y., Jiang, X., Liu, Z. & Liu, Z. Strain effects in graphene and graphene nanoribbons: The underlying mechanism. *Nano Res.* **3**, 545–556 (2010).

14. Scalise, E., Houssa, M., Pourtois, G., Afanas'ev, V. & Stesmans, A. Strain-induced semiconductor to metal transition in the two-dimensional honeycomb structure of MoS_2. *Nano Res.* **5**, 43–48 (2012).

15. Chen, Y. *et al.* Mobility Enhancement of Strained MoS_2 Transistor on Flat Substrate. *ACS Nano* **17**, 14954–14962 (2023).

16. Zhang, Y., Zhao, H. L., Huang, S., Hossain, M. A. & Van Der Zande, A. M. Enhancing Carrier Mobility in Monolayer MoS_2 Transistors with Process-Induced Strain. *ACS Nano* **18**, 12377–12385 (2024).

17. Yang, Y. *et al.* Intrinsic toughening and stable crack propagation in hexagonal boron nitride. *Nature* **594**, 57–61 (2021).

18. Bao, H. *et al.* Tensile loading induced phase transition and rippling in single-layer MoS 2. *Appl. Surf. Sci.* **404**, 180–187 (2017).

19. Asle Zaeem, M. *et al.* Multiscale computational modeling techniques in study and design of 2D materials: recent advances, challenges, and opportunities. *2D Mater.* **11**, 042004 (2024).

20. Liu, R. *et al.* Recent advances in machine learning guided mechanical properties prediction and

design of two-dimensional materials. *Thin-Walled Struct.* **213**, 113261 (2025).

21. Patra, L. & Pandey, R. Mechanical properties of 2D materials: A review on molecular dynamics based nanoindentation simulations. *Mater. Today Commun.* **31**, 103623 (2022).

22. Liu, F., Ming, P. & Li, J. *Ab initio* calculation of ideal strength and phonon instability of graphene under tension. *Phys. Rev. B* **76**, 064120 (2007).

23. Xiong, Z., Zhong, L., Wang, H. & Li, X. Structural Defects, Mechanical Behaviors, and Properties of Two-Dimensional Materials. *Materials* **14**, 1192 (2021).

24. Lee, C., Wei, X., Kysar, J. W. & Hone, J. Measurement of the Elastic Properties and Intrinsic Strength of Monolayer Graphene. *Science* **321**, 385–388 (2008).

25. Hosseini, M., Elahi, M., Pourfath, M. & Esseni, D. Strain induced mobility modulation in single-layer MoS_2. *J. Phys. Appl. Phys.* **48**, 375104 (2015).

26. Li, P. *et al.* In situ nanomechanical characterization of multi-layer MoS_2 membranes: from intraplanar to interplanar fracture. *Nanoscale* **9**, 9119–9128 (2017).

27. Wang, J., Namburu, R. R., Dubey, M. & Dongare, A. M. Origins of Ripples in CVD-Grown Few-layered MoS2 Structures under Applied Strain at Atomic Scales. *Sci. Rep.* **7**, 40862 (2017).

28. Hou, Y. *et al.* Tuning instability in suspended monolayer 2D materials. *Nat. Commun.* **15**, 4033 (2024).

29. Duerloo, K.-A. N., Li, Y. & Reed, E. J. Structural phase transitions in two-dimensional Mo- and W-dichalcogenide monolayers. *Nat. Commun.* **5**, 4214 (2014).

30. Apte, A. *et al.* Structural Phase Transformation in Strained Monolayer $MoWSe_2$ Alloy. *ACS Nano* **12**, 3468–3476 (2018).

31. Dai, Z., Liu, L. & Zhang, Z. Strain Engineering of 2D Materials: Issues and Opportunities at the

Interface. *Adv Mater* **31**, 1805417 (2019).

32. Choi, J. *et al.* Three-Dimensional Integration of Graphene via Swelling, Shrinking, and Adaptation. *Nano Lett.* **15**, 4525–4531 (2015).

33. Reserbat-Plantey, A. *et al.* Strain Superlattices and Macroscale Suspension of Graphene Induced by Corrugated Substrates. *Nano Lett* (2014).

34. Mohiuddin, T. M. G. *et al.* Uniaxial strain in graphene by Raman spectroscopy: G peak splitting, Grüneisen parameters, and sample orientation. *Phys. Rev. B* **79**, 205433 (2009).

35. Plechinger, G. *et al.* Control of biaxial strain in single-layer molybdenite using local thermal expansion of the substrate. *2D Mater.* **2**, 015006 (2015).

36. Ahn, G. H. *et al.* Strain-engineered growth of two-dimensional materials. *Nat. Commun.* **8**, 608 (2017).

37. Castellanos-Gomez, A. *et al.* Local Strain Engineering in Atomically Thin MoS_2. *Nano Lett.* **13**, 5361–5366 (2013).

38. Wang, G. *et al.* Engineering the Crack Structure and Fracture Behavior in Monolayer MoS_2 By Selective Creation of Point Defects. *Adv. Sci.* 2200700 (2022) doi:10.1002/advs.202200700.

39. Li, P., You, Z., Haugstad, G. & Cui, T. Graphene fixed-end beam arrays based on mechanical exfoliation. *Appl. Phys. Lett.* **98**, (2011).

40. Wei, X. *et al.* Comparative Fracture Toughness of Multilayer Graphenes and Boronitrenes. *Nano Lett.* **15**, 689–694 (2015).

41. Wong, L. W. *et al.* Deciphering the ultra-high plasticity in metal monochalcogenides. *Nat. Mater.* **23**, 196–204 (2024).

42. Zheng, X. *et al.* Phase and polarization modulation in two-dimensional In_2Se_3 via in situ

transmission electron microscopy. *Sci. Adv.* **8**, (2022).

43. Yang, Y. *et al.* Brittle Fracture of 2D MoSe2. *Adv. Mater.* **29**, 1604201 (2017).

44. Cao, K. *et al.* Elastic straining of free-standing monolayer graphene. *Nat. Commun.* **11**, 284 (2020).

45. Loginov, P. A., Sidorenko, D. A., Orekhov, A. S. & Levashov, E. A. A novel method for in situ TEM measurements of adhesion at the diamond–metal interface. *Sci. Rep.* **11**, 10659 (2021).

46. Xie, L. & Oshima, Y. Nonlinear mechanical response of rippled MoS2 nanosheets evaluated by in situ transmission electron microscopy. *Appl. Surf. Sci.* **597**, 153708 (2022).

47. Xie, L. & Oshima, Y. Quantitative estimation of atom-scaled ripple structure using transmission electron microscopy images. *Nanotechnology* **32**, 185703 (2021).

48. Li, B. *et al.* Anisotropic Fracture of Two-Dimensional Ta_2NiSe_5. *Nano Lett.* **24**, 6344–6352 (2024).

49. Huang, L. *et al. In Situ* Scanning Transmission Electron Microscopy Observations of Fracture at the Atomic Scale. *Phys. Rev. Lett.* **125**, 246102 (2020).

50. Zhang, P. *et al.* Fracture toughness of graphene. *Nat. Commun.* **5**, 3782 (2014).

51. Ye, G. *et al.* Defects Engineered Monolayer MoS_2 for Improved Hydrogen Evolution Reaction. *Nano Lett.* **16**, 1097–1103 (2016).

Chapter 2 Experimental methods

Introduction

In this chapter, we present the experimental methods and the construction of the experimental platform, including an overview of the instruments used, the implementation of the stretching experiments, and the calibration of both thickness and orientation of molybdenum disulfide (MoS_2). Section 2.1 introduces the fundamental principles of transmission electron microscopy (TEM) and the geometric phase analysis (GPA) method. Section 2.2 describes the stretching holder and the titanium (Ti) plate used to support the stretching chip and the dry transfer method. In Section 2.3, we detail procedures for calibrating the orientation and thickness of the MoS_2.

To investigate the properties of MoS_2 on atomic scale, the transmission electron microscope (TEM) is performed, which is a powerful tool to characterize the structure on atomic scale. The TEM-2100plus (JEOL), with the accelerating voltage of 120 kV, is used in our experiment. The photograph is shown in Figure 2.1.

Figure 2.1 the photograph of TEM-2100plus

2.1 Brief introduction of TEM related technology

2.1.1 Fundamentals of TEM Imaging and HR-TEM analysis

Transmission Electron Microscopy (TEM) is a powerful imaging technique that utilizes a beam of transmitted electrons to form high-resolution images of a specimen. Unlike optical microscopy (OM), which relies on visible light and glass lenses, TEM employs an electron beam as the illumination source and magnetic lenses to focus the electrons. Despite these

differences, the resolution of TEM can still be approximately estimated using the Rayleigh criterion, analogous to the approach in OM, as shown below [1]:

$$\delta = \frac{0.61\lambda}{\mu \sin \beta}, \tag{2.1}$$

In Equation (2.1), λ represents the wavelength of the electron wave, μ is the refractive index of the viewing medium, and βdenotes the acceptance angle of the objective lens. This equation defines the resolution limit, indicating that reducing λ is an effective way to enhance image resolution. For a TEM operating at an accelerating voltage of 200 kV, the electron wavelength is approximately 0.00251 nm—significantly smaller than the diameter of an atom—enabling imaging at atomic-scale resolution. The schematic of a conventional TEM is illustrated in Figure 2.2(a), in comparison with that of an optical microscope (OM) shown in Figure 2.2(b)[2].

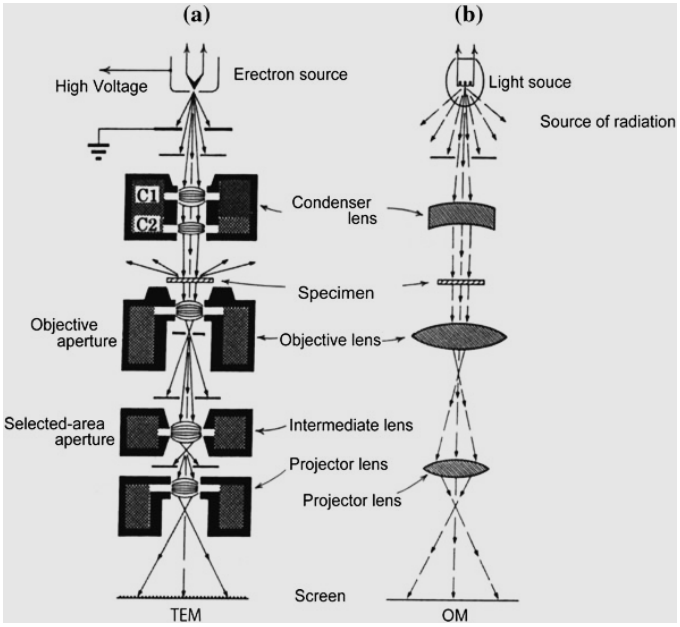

Figure 2.2. The structure of the transmission electron microscope (TEM) (a) and an optical microscope (b)[2].

As illustrated in Figure 2.2, a typical TEM consists of several key components: the electron gun, vacuum system, electromagnetic lenses, sample stage, apertures, and image recording system. The electron gun serves as the source of the electron beam. The vacuum system maintains a high-vacuum environment within the TEM chamber, which minimizes the scattering of electrons by gas molecules—thereby increasing their mean free path—and reduces beam-induced contamination on the sample.

The electromagnetic lens system, comprising the condenser lens, objective lens, intermediate lens, and projector lens (as shown in Figure 2.2(a)), is responsible for focusing and manipulating the electron beam throughout its path. The sample stage secures the sample holder within the TEM and enables the formation of images or diffraction patterns by positioning the sample in the path of the electron beam. It supports a variety of holders, allowing for specialized observations depending on the experimental requirements.

Apertures are employed to selectively filter portions of the electron beam, enhancing contrast and resolution in imaging or diffraction modes. Finally, the image recording system captures the electron-transmitted information, typically via a camera or a fluorescent screen, for further analysis.

2.1.2 Imaging and diffraction in TEM

TEM imaging is accomplished using transmitted electrons. The process begins with the electron gun, which emits and accelerates a beam of electrons. These electrons are first focused by the condenser lens and then directed toward the sample. As the electron beam interacts with

the specimen, some electrons are transmitted while others are scattered, depending on the internal structure of the material.

The objective lens collects and focuses these transmitted and scattered electrons to form an initial image. This image is further magnified by the intermediate and projector lenses, ultimately resulting in a high-resolution image that can be observed on a screen or recorded by a camera.

TEM operates in two primary modes: imaging and diffraction, as illustrated in Figure 2.3(a) and (b). In diffraction mode, a diffraction pattern is formed in the back focal plane of the objective lens, whereas in imaging mode, an intermediate image is formed in the image plane. Switching between these modes is achieved by adjusting the focus of the intermediate lens, which determines whether the image or diffraction pattern appears in the second intermediate image plane. The projector lens then magnifies the selected output, which is finally displayed or captured by a CCD camera.

In this study, atomic-scale images of the sample structure are acquired in imaging mode and recorded using a CCD camera.

To resolve atomic details, high-resolution transmission electron microscopy (HR-TEM) is used. In HR-TEM, contrast arises from the interference between transmitted and scattered electron waves. For very thin specimens, the amplitude of the incident wave is largely unaffected, while its phase is slightly altered by interactions with the sample. These phase changes are correlated with the positions of atomic columns and produce an interference pattern

upon exit. By capturing the amplitude of this phase interference with a CCD camera, the HR-TEM image reveals the projected atomic structure of the sample.

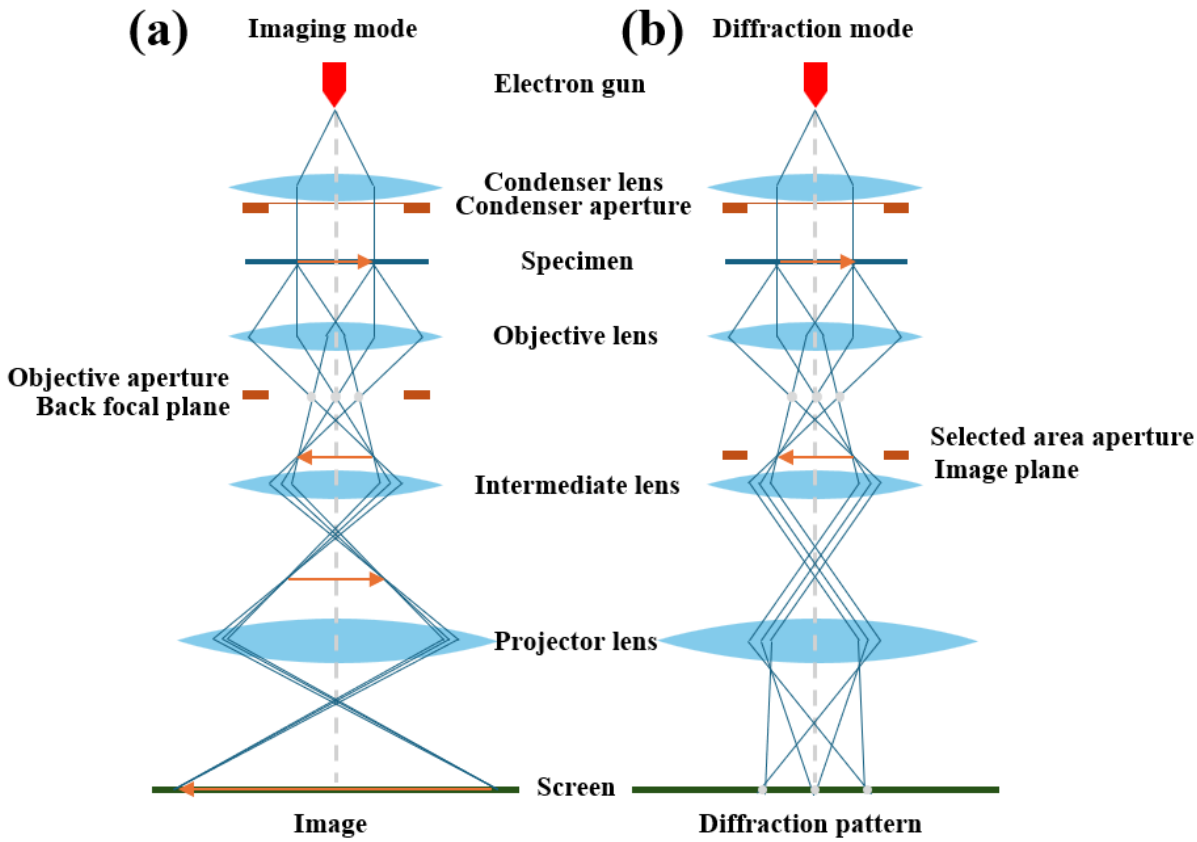

Figure 2.3. Schematic of the imaging mode (a) and diffraction mode (b) of TEM. Imaging/diffraction mode is adjusted when the image/diffraction pattern is showing in the plane of the second intermediate image by adjusting the intermediate lens.

2.1.3 Geometric phase analysis

Geometric Phase Analysis (GPA) is a quantitative technique used in transmission electron microscopy (TEM) to measure strain and displacement fields at the nanoscale. It is particularly valuable in high-resolution TEM (HR-TEM) and scanning TEM (STEM) images for the analysis of lattice distortions, interfaces, and defects in crystalline materials.

The fundamental concept of GPA is based on the analysis of phase shifts in the periodic

lattice fringes of an HR-TEM image. These fringes can be interpreted as the result of interference between transmitted and diffracted electron waves. By applying a Fourier transform to the HR-TEM image, the periodic lattice information is transferred into reciprocal space, where specific diffraction spots corresponding to chosen lattice planes can be isolated using a mask.

The inverse Fourier transform of a selected spot, combined with appropriate filtering, yields a complex image that contains both amplitude and phase information. The phase component reflects the local displacement field relative to a reference lattice, and the gradient of the phase gives access to the local strain. This allows for the mapping of strain tensor components with nanometer or even sub-nanometer resolution.

GPA is a non-destructive, post-processing technique and does not require specific sample preparation beyond that used for HR-TEM. It provides high sensitivity to small changes in lattice spacing and orientation, making it ideal for the analysis of heterostructures, grain boundaries, dislocations, and other structural inhomogeneities. The brief theoretical explanation can be written as follows[3,4]:

Simply, the intensity of an HR-TEM image, $I(\boldsymbol{r})$, can be described as:

$$I(\boldsymbol{r}) = \sum_g I_g(\boldsymbol{r}) e^{2\pi i g \bullet \boldsymbol{r}} \tag{2.2}$$

In the context of GPA, g denotes the reciprocal lattice vectors of an ideal, undistorted crystal. The local Fourier components of a high-resolution TEM image can be expressed as:

$$I_g(\boldsymbol{r}) = A_g(\boldsymbol{r})e^{iP_g(\boldsymbol{r})}, \tag{2.3}$$

Here, $A_g(\boldsymbol{r})$ represents the local amplitude, which reflects the image contrast, and $P_g(\boldsymbol{r})$ is the local phase, which encodes positional information related to the lattice distortion.

The phase $P_g(\boldsymbol{r})$ is directly related to the local displacement field $\boldsymbol{u}(\boldsymbol{r})$ of the lattice through the following relation:

$$P_g(r) = -2\pi g \bullet \boldsymbol{u}(r). \tag{2.4}$$

Given two non-collinear reciprocal lattice vectors $g1$ and $g2$, with corresponding real-space basis vectors $\boldsymbol{a}_1$ and $\boldsymbol{a}_2$, the displacement field $\boldsymbol{u}(r)$ can be determined as:

$$u(\boldsymbol{r}) = -\frac{1}{2\pi}[P_{g1}(\boldsymbol{r})\boldsymbol{a}_1 + P_{g2}(\boldsymbol{r})\boldsymbol{a}_2], \tag{2.5}$$

where, $\boldsymbol{a}_1$ and $\boldsymbol{a}_2$ are the basis vectors of the lattice in real space corresponding to the $g1$ and $g2$. Then, the strain field can be retrieved from the gradient of the displacement field:

$$\varepsilon = \begin{pmatrix} \varepsilon_{xx} & \varepsilon_{xy} \\ \varepsilon_{yx} & \varepsilon_{yy} \end{pmatrix} = \begin{pmatrix} \frac{\partial u_x}{\partial x} & \frac{\partial u_x}{\partial y} \\ \frac{\partial u_y}{\partial x} & \frac{\partial u_y}{\partial y} \end{pmatrix}. \tag{2.6}$$

By applying this analysis to HR-TEM images, a two-dimensional strain map with atomic-scale resolution can be reconstructed. In this study, we utilize GPA to extract quantitative strain information from HR-TEM images obtained during in-situ TEM observations. This allows us to investigate the local deformation behavior and structural evolution of the material at the atomic level.

2.1.4 Focused ion beam (FIB)

The SMI3050 focused ion beam (FIB) system was employed for nanoscale patterning and sample preparation due to its exceptional milling precision and versatility. This instrument enables the fabrication of well-defined slits and gaps at the sub-100 nm scale while minimizing damage to surrounding areas. Moreover, its localized milling capability ensures that the structural integrity of the suspended membranes is preserved, allowing highly customized geometries tailored to our experimental requirements. Figure 2.4 illustrates the SMI3050 system and a representative sample with a precisely milled gap, demonstrating its capability for high-quality nanofabrication.

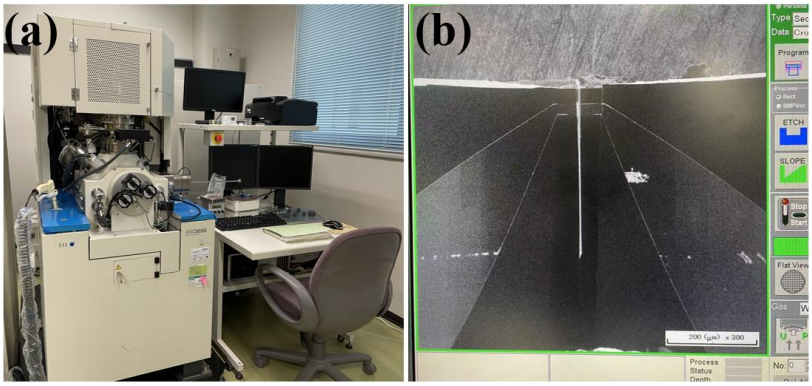

Figure 2.4 The photograph of SMI 3050 and a gap after milling

2.2 Stretching TEM holder and dry transfer process

2.2.1 Stretching TEM holder

To investigate the mechanical properties of MoS_2 thin films under transmission electron microscopy (TEM), our laboratory has developed a custom-designed in-situ stretching sample holder. This holder enables real-time tensile testing of MoS_2 thin films during TEM observation. A top view of the in-situ TEM holder is presented in Figure 2.5.

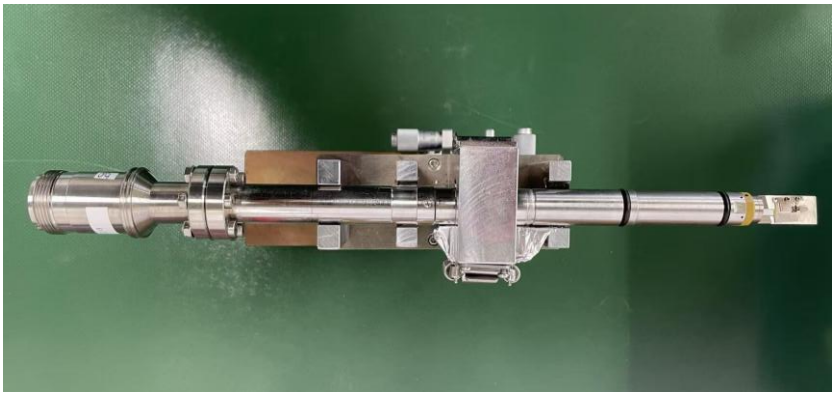

Figure 2.5 Top view of the overall structure of the holder

As shown in Figure 2.6(a), the top view of the holder reveals the sample loading side, where the MoS_2 film is mounted. A corresponding three-dimensional model of the same configuration is provided in Figure 2.6(b) to better visualize the structural layout. Figure 2.6(c) presents a simplified schematic diagram illustrating the stretching principle, in which the displacement is driven by voltage-controlled actuation to achieve uniform in-plane tensile strain.

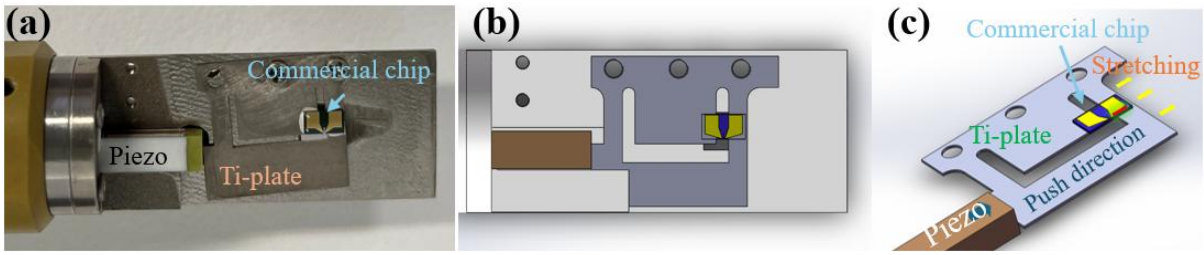

Figure 2.6 (a) Top view of the stretching holder, sample loading side. (b) The 3D model diagram of (a). (c) Simple schematic diagram of the holder stretching principle.

To verify the performance of the holder, two separate Si chips were placed at both ends of the stretching stage and imaged using an optical microscope, as shown in Figure 2.7(a). This test setup allows visual tracking of the stretching displacement under increasing voltage. As demonstrated in Figure 2.7(b), the stretching distance exhibits a linear correlation with the applied voltage, achieving a maximum displacement of approximately 4 μm. This value reflects the tensile deformation capacity of the Ti-plate embedded in the holder and confirms the suitability of the device for in-situ straining experiments at the micro- and nanoscale.

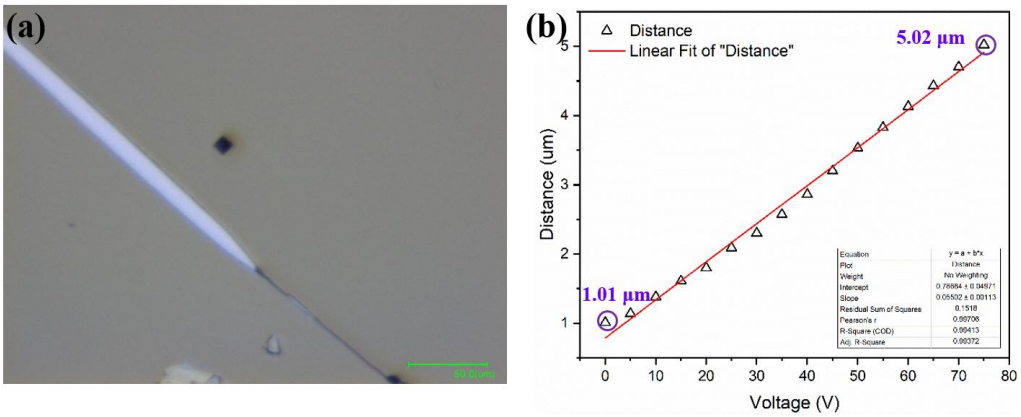

Figure 2.7 (a) Optical microscope image showing a cracked silicon wafer placed at both ends of the stretching stage to evaluate the stretching capability of the device. (b) The stretching distance exhibits a linear relationship with the applied voltage, reaching a maximum of approximately 4 μm. This value represents the tensile deformation capacity of the Ti-plate.

2.2.2 Dry transfer process

2.2.2.1 MoS_2 exfoliation

In this study, mechanical exfoliation of MoS_2 was carried out using PDMS (polydimethylsiloxane) as a cleaner alternative to conventional adhesive tape. As shown in Figure 2.8(a), the process begins with a natural bulk MoS_2 crystal. A PDMS stamp is gently pressed onto the surface of the crystal and then peeled off, allowing thin layers to be exfoliated due to the weak van der Waals forces between atomic layers. The resulting MoS_2 flakes adhere to the surface of the PDMS, as seen in Figure 2.8(b).

Next, the PDMS carrying the exfoliated flakes is brought into contact with a 285 nm SiO_2-coated silicon wafer, which serves as an intermediate substrate. As shown in Figure 2.8(c) and (d), the flakes are transferred by aligning the PDMS stamp with the Si chip and applying gentle pressure, optionally with mild heating. The PDMS is then carefully peeled away, leaving a distribution of MoS_2 flakes on the SiO_2 surface. This intermediate step provides a stable, optically compatible platform for locating and selecting suitable flakes in the subsequent transfer process.

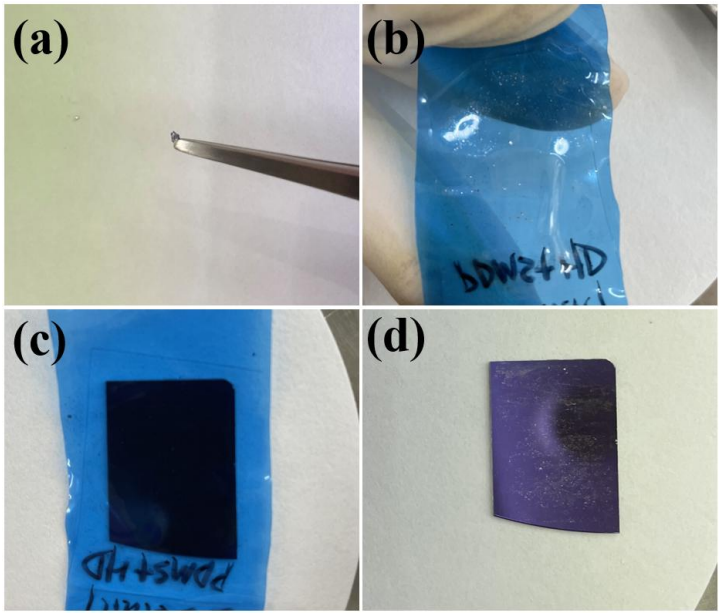

Figure 2.8. Mechanical exfoliation of MoS_2. (a) Photograph of the natural MoS_2 bulk. (b) Exfoliated MoS_2 flakes on PDMS. (c) Transferring MoS_2 flakes on SiO_2 coated Si chip.

2.2.2.2 Polypropylene carbonate stamp preparation

Polypropylene carbonate (PPC) is a widely used stamp material for the dry transfer of two-dimensional (2D) materials due to its excellent physical and chemical properties[5]. As a polymer, PPC provides strong adhesion to 2D materials, enabling reliable pickup of ultrathin layers such as graphene, MoS_2, or h-BN without causing damage or contamination. In this paper, we prepare PPC solution by resolve 3 g PPC grain in 10 ml Anisole solvent with a stirring speed of 500 rpm for 24 h, the resolve temperature was kept at 80 ℃.

A key advantage of PPC is its thermal responsiveness. At moderately elevated temperatures (typically 80–120°C), PPC becomes soft and tacky, conforming closely to the surfaces of 2D materials and substrates. This ensures effective contact during pickup and release[6]. Upon cooling or gentle mechanical detachment, PPC releases the 2D flake cleanly onto the target substrate with minimal residue. The PPC stamp preparation process is illustrated

in Figure 2.9.

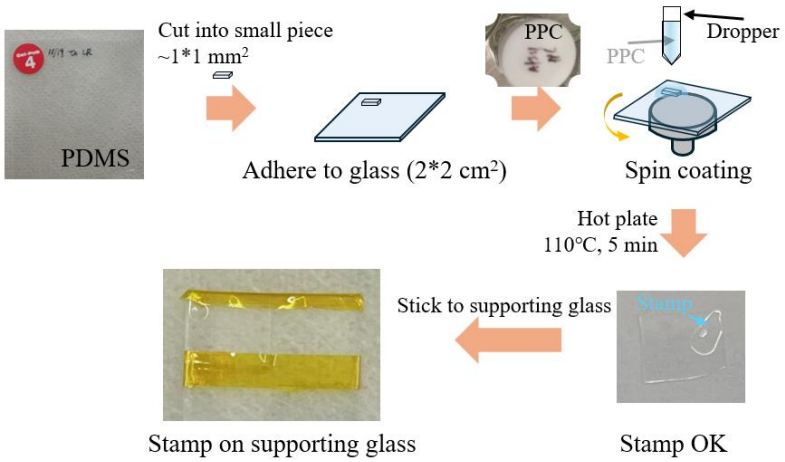

Figure 2.9. PPC stamp preparation process

2.2.2.3 Target flakes transfer

To perform precise dry transfer of selected MoS_2 flakes, a custom-built transfer platform was used. As shown in Figure 2.10(a), the platform is equipped with a digital optical microscope, which enables real-time observation and alignment of flakes during the transfer process. The microscope provides sufficient magnification and clarity to accurately locate and position individual 2D flakes on the target substrate.

In addition, a small lifting instrument, shown in Figure 2.10(b), is integrated into the setup to allow for controlled 3-axis movement during the transfer. This tool enables high-precision manipulation of the PDMS/PPC stamp or other transfer medium, ensuring gentle contact and precise control. Together, the microscope and lifting mechanism facilitate reliable, repeatable transfer of 2D materials with minimal risk of damage or misalignment.

Figure 2.10. (a) Transfer platform integrated with a digital optical microscope for flake alignment and observation. (b) A precision vertical lifting device enables delicate and controlled transfer operations.

To prepare MoS_2 samples for in-situ TEM analysis, a dry transfer technique utilizing a PDMS/PPC (polypropylene carbonate) stamp was employed to ensure precise placement of the selected flakes. As illustrated in Figure 2.11, the process begins by aligning the transparent PDMS/PPC stamp to a target MoS_2 flake exfoliated onto a heated SiO_2/Si substrate. After warming the substrate for 2 minutes and subsequently cooling it down to 40 °C to promote adhesion, the flake is gently picked up by the stamp. It is then realigned over the slit window area of a Si/SiN_x chip, which features a thin silicon nitride membrane designed for electron transparency and in-situ observation. To complete the transfer, the system is gently heated to 75 °C, enabling controlled release of the flake onto the chip surface. As shown in Figure 2.12, the MoS_2 flake is accurately positioned on the gap region—panel (a) shows the chip prior to transfer, while panel (b) confirms the successful and precise placement. The Si chip for stretching was then fixed on the Ti-plate by silver paste, the curing parameter of the silver paste is 140 ℃, 2 h, then the samples for TEM observation were prepared. This dry transfer approach minimizes contamination and mechanical damage, offering a reliable method for preparing clean and well-positioned samples for high-resolution and in-situ TEM studies.

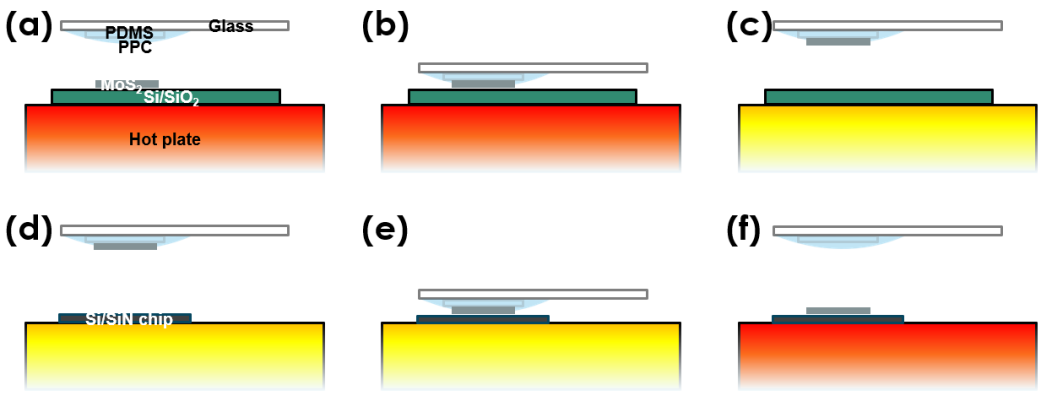

Figure 2.11. Schematic illustration of the dry transfer process using a PDMS/PPC stamp. The stamp is first aligned to pick up the target MoS_2 flake from the SiO_2/Si substrate, followed by precise placement onto the desired location on the Si/SiN_x chip.

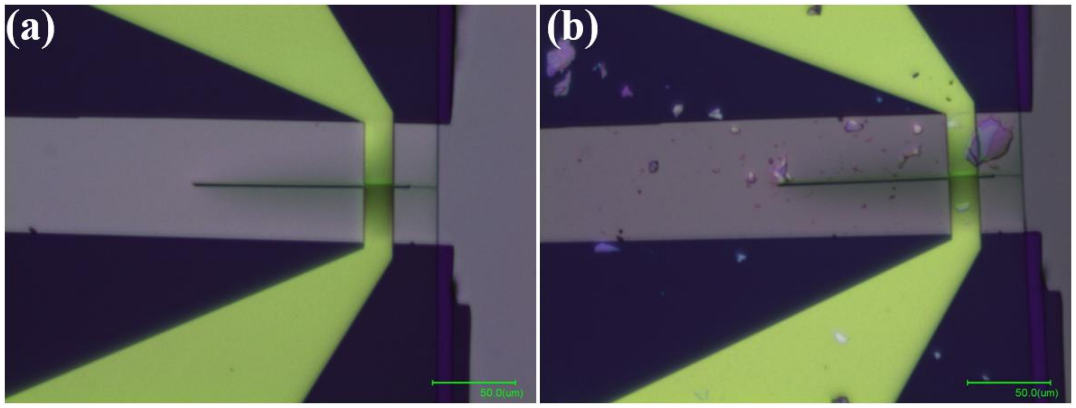

Figure 2.12. Optical microscope images showing the Si/SiN_x chip (a) before and (b) after the dry transfer process. The MoS_2 flake was accurately positioned onto the membrane window of the chip.

2.3 Sample selection

2.3.1 Layer identification

In 2007, a study first reported that the optical contrast of graphene deposited on a SiO_2/Si substrate is strongly dependent on its thickness, particularly when observed under an optical microscope with a specific oxide thickness on the substrate[7]. Since then, similar contrast-

dependent optical behavior has been observed in other two-dimensional (2D) materials, such as WSe_2 and MoS_2[8–10]. This property enables quick and non-destructive identification of flake thickness using standard optical microscopy. The underlying mechanism, as illustrated in Figure 2.13, is attributed to interference effects in the reflected light. Specifically, the intensity of reflected light varies with the number of layers in the 2D material, governed by the following equation[7]:

$$I(n_1) = \left|\left(r_1 e^{i(\Phi_1+\Phi_2)} + r_2 e^{-i(\Phi_1-\Phi_2)} + r_3 e^{-i(\Phi_1+\Phi_2)} + r_1 r_2 r_3 e^{i(\Phi_1-\Phi_2)}\right) \times \left(e^{i(\Phi_1+\Phi_2)} + r_1 r_2 e^{-i(\Phi_1-\Phi_2)} + r_1 r_3 e^{-i(\Phi_1+\Phi_2)} + r_2 r_3 e^{i(\Phi_1-\Phi_2)}\right)^{-1}\right|^2, \quad (2.7)$$

Where

$$r_1 = \frac{n_0 - n_1}{n_0 + n_1},$$

$$r_2 = \frac{n_1 - n_2}{n_1 + n_2},$$

$$r_3 = \frac{n_2 - n_3}{n_2 + n_3} \quad (2.8)$$

Then the contrast C can be defined as the relative intensity of reflected light in the presence ($n_1 \neq 1$) and absence ($n_1 = n_0 = 1$) of 2D nanosheets,

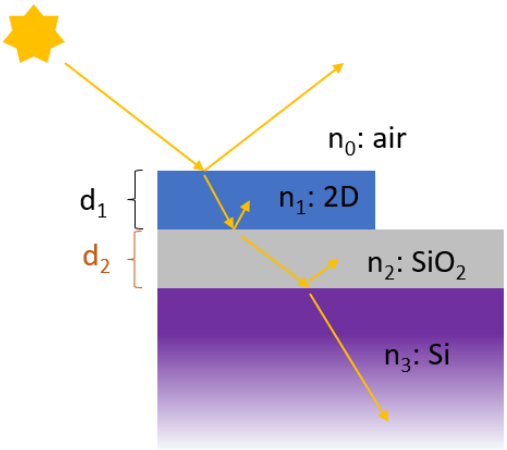

Figure 2.13 Reflective structure of multi-layer films formed by 2D material on silicon wafers.

$$C = \frac{I(n_1=1)-I(n_1)}{I(n_1=1)} \tag{2.9}$$

While numerous studies have validated the use of optical contrast for identifying the thickness of MoS_2 flakes, and many experimental results have been reported in detail[7-10], variations in optical microscopy setups necessitate the development of calibration standards that allow reliable layer-number identification independent of specific imaging conditions. To accurately determine the number of MoS_2 layers, a nanosheet exhibiting a step-terrace structure was first exfoliated and transferred onto a SiO_2/Si substrate, where the oxide layer was 285 nm thick. The flake was then imaged under an optical microscope, as shown in Figure 2.14(a). Multiple distinct color regions were observed, corresponding to different thicknesses within the same flake. To establish a reliable relationship between optical color and flake thickness, atomic force microscopy (AFM) measurements were performed on the selected regions marked by dashed-line squares. The measured thicknesses of the lower and upper terraces are presented in Figure 2.14(b) and Figure 2.14(c), respectively. The small arrow on the dashed square indicates the upward direction, consistent with the orientation of the AFM scan. The height profile obtained along the dashed line was superimposed onto the optical image to directly link the visual contrast with the physical thickness, facilitating the identification of MoS_2 layers based on optical appearance.

Atomic force microscopy (AFM) measurements revealed a stepwise increase in thickness along the red dashed line from right to left in Figure 2.14(b), corresponding closely with the contrast variations observed in the optical microscope (OM) image in Figure 2.14(a). The

height differences in the AFM image are consistent with the color contrast seen in the OM image, validating the use of optical microscopy as a qualitative tool for estimating flake thickness. From the AFM analysis, the height differences between adjacent contrast regions were determined to be approximately 0.75 nm and 1.50 nm, corresponding to one and two additional MoS_2 layers, respectively. The thinnest region, marked in green in Figure 2.14(b), exhibited a thickness of 2.86 nm. This region was later confirmed to be monolayer MoS_2 through Raman spectroscopy, as discussed in a subsequent section. Considering a previously reported instrumental offset of approximately 2.1 nm due to interactions between the AFM tip and substrate[11], the measured thicknesses within the dashed-line area in Figure 2.14(a) can be accurately correlated with specific layer numbers. These identified thickness values are labeled with white alphanumeric characters directly on the figure to facilitate interpretation.

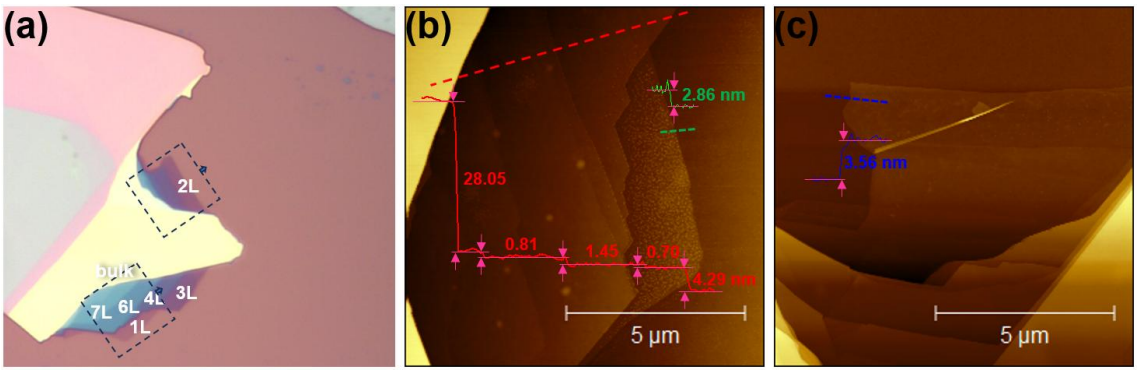

Figure 2.14 (a) Optical microscope image of terraced structural MoS_2 nanosheet with the layer number marked as 1L to bulk thickness, the dash line square outlined the area that measured by AFM. AFM results of (b) the lower dash line square and (c) the upper dash line square, with the height profile pasted on.

Figure 2.15(a) shows Raman spectra of MoS_2 with varying layers obtained using 532 nm laser line, the main Raman peaks in this spectrum correspond to the zone center first order E_{2g}^1 mode at ~384 cm^{-1} and the A_{1g} mode at ~409 cm^{-1}. The frequencies of A_{1g} and E_{2g}^1 peaks

excited by 532 nm laser line are illustrated in Figure 2.15(b). The wavenumber of the modes shows that the wavenumber of the A_{1g} mode decreases whereas that of E_{2g}^1 mode increases as the layer number is reduced when the number of the layer is less than 7, while both the frequencies of these two mode drift to the higher side in bulk result compared to the result of 7 layers (7L). A phenomenon observed in other literatures[12]. The peak frequency difference between the A_{1g} mode and E_{2g}^1 mode (Δ) was presented in Figure 2.15(c), corresponding to the number of layers. Regardless of the occurrence of drift, a consistent increasing trend is maintained. It is noteworthy that the Δ value for the monolayer is 18.1 cm^{-1}, aligning well with the result from the literature. This alignment suggests the successful exfoliation and acquisition of experimental data for a single layer MoS_2. Whatever the trend or the final calculation results, the difference between the A_{1g} mode and E_{2g}^1 mode (Δ) are generally in line with expectations and consistent with findings in the literature[12].

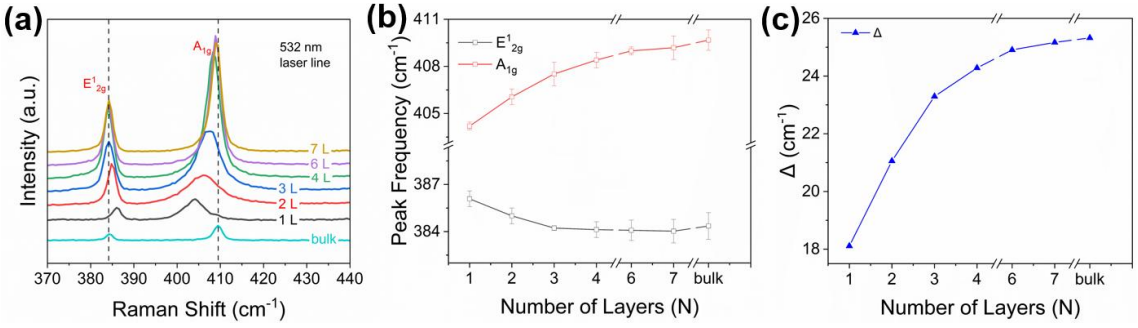

Figure 2.15 (a) Raman spectra of different thicknesses of MoS_2 nanosheet using 532 nm line. The right and left dashed lines indicate the position of A_{1g} and E_{2g}^1 peaks of bulk MoS_2, respectively. (b) Thickness-dependent A_{1g} and E_{2g}^1 peak frequencies. (c) Peak frequency difference between the A_{1g} mode and E_{2g}^1 mode (Δ) corresponding to the number of layers.

The aforementioned experimental results confirm the successful preparation of terrace-structured molybdenum disulfide (MoS_2) flakes with distinct thicknesses, including monolayer

(1L), bilayer (2L), trilayer (3L), four-layer (4L), six-layer (6L), seven-layer (7L), and bulk. Both atomic force microscopy (AFM) and Raman spectroscopy were employed to characterize and validate the thickness of these samples. Given that the present study focuses on monolayer and few-layer MoS_2, these characterized terrace samples serve as calibration standards. By analyzing and calibrating the optical contrast of the different thicknesses, we establish a reliable reference to determine the layer number in unknown samples based on optical microscopy (OM) images.

To quantify the optical contrast, OM images of MoS_2 flakes were processed using ImageJ software (version 1.46r), which is freely available online. For RGB-format color images, the contrast value (C) of each pixel—representing the brightness—was calculated based on the following equation[8]:

$$C = (C_R + C_G + C_B)/3 \tag{2.10}$$

In which, the C_R, C_G and C_B are the R, G and B values per pixel in color image, respectively; 0 is darkest, and 255 is brightest (saturation).

The grayscale images of R, G and B channels can be extracted by using “Split channels” commend in the menu bar. In the images we want to acquire the contrast value, we can choose one area by dragging a rectangular box across the area and then press “K” to obtain the contrast profile automatically, plot by taking the mean of the pixel values row by row, in the selected area. Then the detailed optical contrast value can be read by analyzing the profile we obtained.

The color OM image of MoS_2 nanosheet and its split channel images (R, G and B images)

were shown in Figure 2.16(a)-(d), with the split channel images labeled as R, G and B, respectively. To ensure comprehensive data coverage while streamlining the collection, four distinct areas (area 1, area 2, area 3, and area 4) were selected for gathering contrast values of 1L, 2L, 3L, 4L, 6L, 7L, and bulk. The specific positions of these areas are marked in (a)-(d). Notably, area 1 spans the substrate and 1L, area 2 spans the substrate and 2L, area 3 spans the substrate, 3L, 4L, and 6L, while area 4 has the widest range, capturing contrast values of the substrate, 4L, 6L, 7L, and bulk. However, within the areas, 1L and 3L width only contains few hundreds nm, which means only few rows of pixels were calculated in contrast values. The contrast values collected in area 1 are inserted into Figure 2.16 (a)-(d) accordingly, Light blue dotted lines in the contrast curve images denote the contrast value platform of the substrate (C_A), and light purple dotted lines mark the value platform of the MoS_2 nanosheet contrast (C_B). To describe the optical identification method, the contrast difference (C_Z) is obtained by subtracting C_A from C_B. Similarly, for the contrast values of split images, the contrast of the substrate was defined as C_{AR}, C_{AG} and C_{AB}, respectively. Correspondingly, the contrasts on MoS_2 nanosheet are defined as C_{BR}, C_{BG} and C_{BB}, the contrast differences are then defined as C_{ZR}, C_{ZG} and C_{ZB}, as shown in the following equations.

$$C_Z = C_B - C_A$$

$$C_{ZR} = C_{BR} - C_{AR}$$

$$C_{ZG} = C_{BG} - C_{AG}$$

$$C_{ZB} = C_{BB} - C_{AB} \tag{2.11}$$

The contrast profiles for these four areas are illustrated in Figure 2.16, the result of the area 1 incorporated into the MoS_2 nanosheet images in Figure 2.16(a)-(d), correspondingly. The results for area 2 are presented in Figure 2.16(e)-(g), followed by Figure 2.16(i)-(l) for area 3 and Figure 2.16(m)-(p) for area 4. To enhance the credibility of the data, contrast values were selected from the data platform away from the regional boundary. This choice is made to mitigate the impact of boundary unevenness on data accuracy, particularly evident in Figure 2.16(h). As can be seen from the following diagrams, a distinct contrast differentiation platform is discernible between layers of different thicknesses. Even in instances with relatively close values, such as 4L and 6L in Figure 2.16(j), there are noticeable contrast differences in other channels, such as Figure 2.16(i), (k), (l). Moreover, the substrate contrast values in different areas fall within a controllable error range, further affirming the credibility of the data.

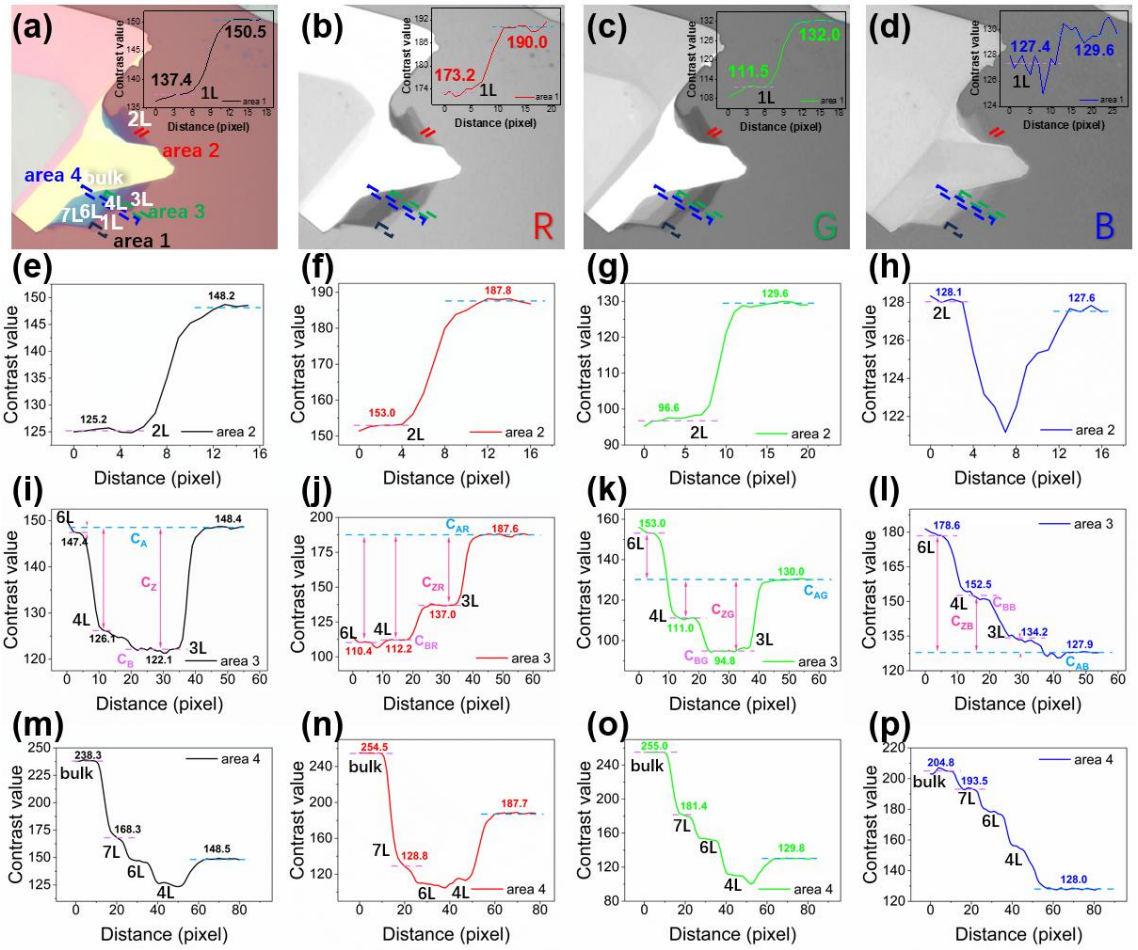

Figure 2.16 OM image (a) with the white alphanumeric digitals correspond to the corresponding number of layers of the MoS_2 nanosheet and split channel of (b) red, (c) green, and (d) bule. Insert pictures are the corresponding contrast profiles of the area 1. (e)-(f) Contrast profile of the area 2 shown in (a)-(d). (i)-(l) Contrast profile of the area 1 shown in (a)-(d), C_A: contrast of 285 nm SiO_2/Si substrate. C_B: contrast of MoS_2 nanosheet. C_Z: the contrast difference between MoS_2 nanosheet and substrate. C_{AR}: contrast of 285 nm SiO_2/Si substrate of red channel image. C_{BR}: contrast of MoS_2 nanosheet of red channel image. C_{ZR}: the contrast difference between MoS_2 nanosheet and substrate of red channel image. C_{AG}, C_{BG}, C_{ZG}, C_{AB}, C_{BB}, C_{ZB} and so on. (m)-(p) Contrast profile of the area 4 shown in (a)-(d).

In Figure 2.17(a) and Figure 2.17(b), the plotted values represent C_{ZR}, C_{ZG}, and C_{ZB} for 1L-4L, 6L, 7L and bulk MoS_2 nanosheet, respectively. It is evident that the thickness of 2L-4L MoS_2 nanosheet based solely on C_Z values proves challenging, as the contrast difference from -22.3 to -26.3, which is too small for accurate distinction. Conversely, more pronounced contrast difference results are observed for 1L, 6L, and bulk MoS_2 nanosheets. In order to

effectively and accurately distinguish 2L-4L, the optical contrast differences measured from their split channel images of R, G, and B (C_{ZR}, C_{ZG}, and C_{ZB}) were plotted. As shown in Figure 2.17(b), the C_{ZR} values of 2L-3L MoS_2 nanosheets are sufficient for layer identification. Therefore, by combining the contrast difference value of C_Z and C_R, we can easily find out the actual thickness of the MoS_2 nanosheet under 4L, providing ample information for our research.

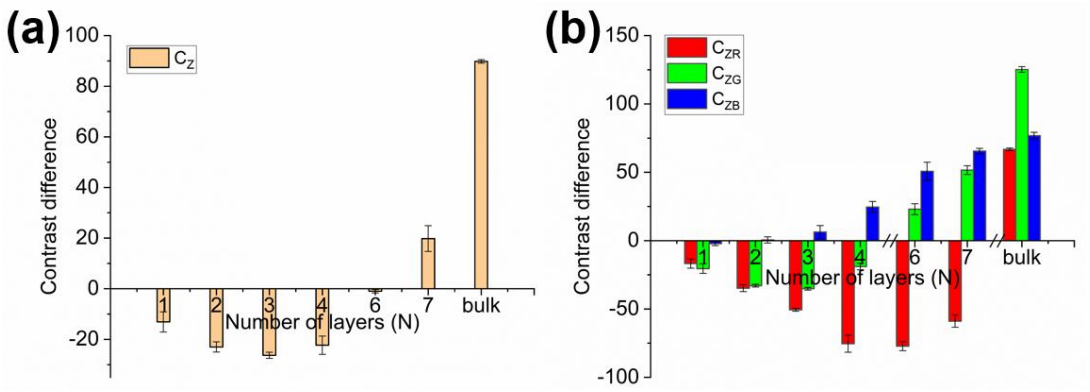

Figure 2.17 (a) Plot of C_Z values of 1L-4L, 6L, 7L and bulk MoS_2 nanosheet. (b) C_{ZR}, C_{ZG}, and C_{ZB} values of 1L-4L, 6L, 7L and bulk MoS_2 nanosheet.

To further facilitate rapid thickness identification during the transfer process, an additional top-view image of the terrace-structured MoS_2 flake was acquired using the camera mounted on the transfer stage. As shown in Figure 2.18(a), this camera setup exhibits distinct imaging characteristics due to differences in sensor response and illumination conditions compared to the calibration optical microscope. Consequently, the contrast in the acquired image cannot be directly interpreted using the previously established calibration. To address this, a new calibration was performed to correlate the observed contrast with the known thicknesses of the MoS_2 flake. The resulting calibrated contrast values are presented in Figure 2.18(b),

demonstrating that even under different imaging conditions, accurate thickness assignment can still be achieved. This approach allows for fast layer identification during manipulation and ensures effective integration of the flake onto the desired substrate.

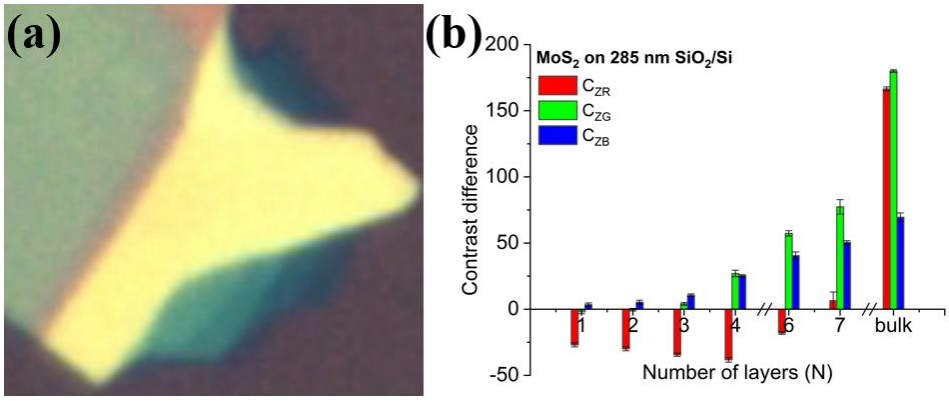

Figure 2.18 (a) Top-view image of a terrace-structured MoS_2 flake captured using the transfer-stage camera. Due to differences in camera sensor and lighting conditions, the image contrast varies from that of the standard optical microscope. (b) Calibrated contrast value of the flake in (a), where the different contrast corresponds to a specific number of MoS_2 layers.

2.3.2 Orientation Selection of Zigzag (ZZ) Edge in Exfoliated MoS_2

The crystallographic orientation of MoS_2 plays a crucial role in determining its physical and mechanical properties, particularly when conducting edge-sensitive characterizations and in-situ mechanical tests. Among the two principal edge types—zigzag (ZZ) and armchair (AC)—the ZZ edge has been observed to exhibit enhanced cleavage behavior and stability under mechanical stress. As reported by Guo et al.[13], exfoliated MoS_2 flakes demonstrate a strong preference for long smooth cleaving along the ZZ direction due to its lower edge energy, resulting in more stable and smoother terminations.

Figure 2.19 presents an optical microscope image of multiple exfoliated MoS_2 flakes on a SiO_2/Si substrate. Several flakes show distinctly flat edges, which are highlighted with yellow

dashed lines. These linear and smooth boundaries are indicative of cleavage along specific crystallographic orientations. The pronounced regularity of these edges implies a preferential exfoliation along the ZZ direction, offering a simple yet effective method for edge identification.

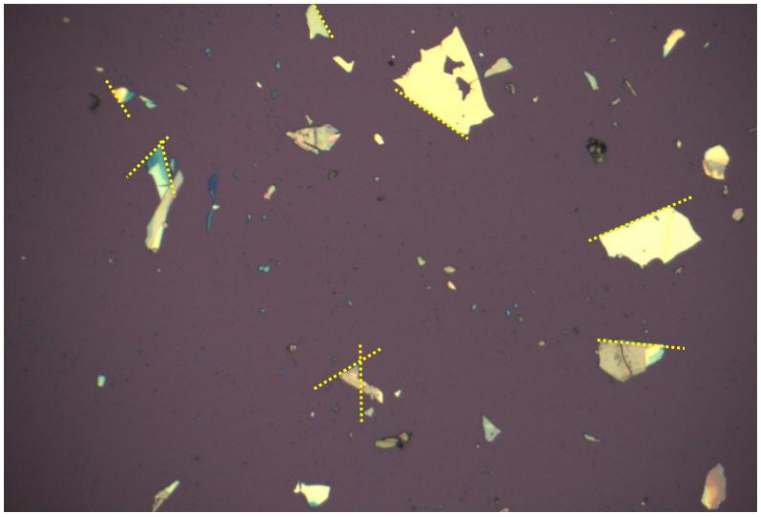

Figure 2.19 Exfoliated MoS_2 flakes on Si chip, with flat edges marked with yellow dashed line

To further validate this approach, high-resolution evidence from both optical and transmission electron microscopy was collected, as shown in Figure 2.20. By aligning the MoS_2 flake such that its smooth edge corresponds with the transfer direction, we successfully confirmed that the chosen edge aligns with the zigzag orientation. This confirmation was achieved through the analysis of diffraction patterns and lattice alignment in TEM, corroborated by flake geometry observed in the optical microscope image.

Together, Figures 2.19 and 2.20 provide compelling experimental evidence that the natural cleavage tendency of MoS_2 can serve as a reliable guide for the selection of the ZZ edge. This edge-selective strategy is critical for the preparation of oriented samples, especially in studies

focusing on anisotropic fracture behavior or edge-related electronic properties.

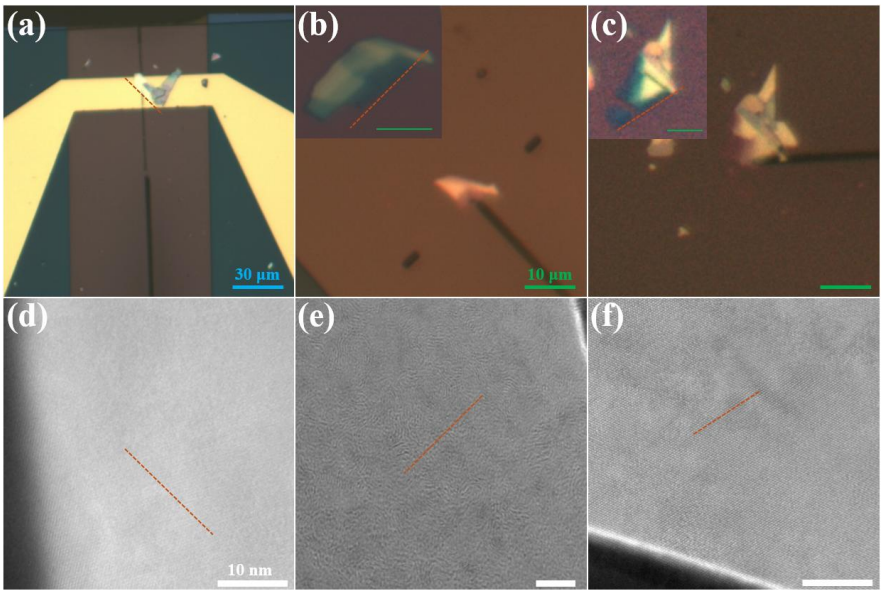

Figure 2.20 Successful selection of the zigzag (ZZ) orientation according to the arrangement of the smooth edge after the exfoliation.

Conclusion

In this chapter, we systematically described the instruments, materials, and techniques employed in the preparation and characterization of MoS_2 samples for in-situ transmission electron microscopy (TEM) analysis. We also introduced the JEOL 2100Plus TEM and its associated imaging configurations, laying the foundation for the high-resolution imaging work in subsequent experiments. The design and functionality of the custom-built in-situ stretching holder were illustrated, along with its actuation mechanism and mechanical performance.

To prepare high-quality MoS_2 samples, we employed a modified mechanical exfoliation method using PDMS, followed by a dry transfer process facilitated by a PDMS/PPC stamp. The precision of this method enables accurate placement of the MoS_2 flakes onto Si/SiN_x chips, critical for successful in-situ observation.

We further explored the optical contrast-based thickness determination method, supported by atomic force microscopy (AFM) and Raman spectroscopy, verifying the number of MoS_2 layers and establishing a contrast-thickness correlation. This enabled the calibration of OM contrast using RGB image processing through ImageJ. Additionally, we demonstrated that such contrast calibration is extendable to alternative imaging systems, including the transfer-stage camera, ensuring real-time thickness recognition during manipulation.

Finally, we addressed the orientation selection of MoS_2 flakes, focusing on identifying the zigzag (ZZ) edge direction, which is critical for anisotropic mechanical studies. Based on the natural cleavage behavior and smooth edge features observed in optical microscopy, and

supported by detailed optical and TEM validation, we established a practical method for identifying and aligning ZZ edges during sample preparation.

Together, these experimental strategies and calibration procedures lay the foundation for high-precision in-situ TEM mechanical testing of 2D materials, ensuring both structural integrity and orientation-specific investigation.

References

1. D. B. Williams and C. B. Carter. *Transmission Electron Microscopy*. (Springer US, Boston, MA, 2009).
2. N. tanaka. *Structure and Imaging of a Transmission Electron Microscope (TEM), in Electron Nano-Imaging*. vol. pp. 17-28 (Springer Japan, Japan, 2017).
3. Hÿtch, M. J., Snoeck, E. & Kilaas, R. Quantitative measurement of displacement and strain fields from HREM micrographs. *Ultramicroscopy* **74**, 131–146 (1998).
4. Hÿtch, M. J., Putaux, J.-L. & Pénisson, J.-M. Measurement of the displacement field of dislocations to 0.03 Å by electron microscopy. *Nature* **423**, 270–273 (2003).
5. Kinoshita, K. *et al.* Dry release transfer of graphene and few-layer h-BN by utilizing thermoplasticity of polypropylene carbonate. *Npj 2D Mater. Appl.* **3**, 22 (2019).
6. Fan, S., Vu, Q. A., Tran, M. D., Adhikari, S. & Lee, Y. H. Transfer assembly for two-dimensional van der Waals heterostructures. *2D Mater.* **7**, 022005 (2020).
7. Blake, P. *et al.* Making graphene visible. *Appl. Phys. Lett.* **91**, 063124 (2007).
8. Li, H. *et al.* Rapid and Reliable Thickness Identification of Two-Dimensional Nanosheets Using Optical Microscopy. *ACS Nano* **7**, 10344–10353 (2013).
9. Casiraghi, C. *et al.* Rayleigh Imaging of Graphene and Graphene Layers. *Nano Lett.* **7**, 2711–2717 (2007).
10. Li, H., Wu, J., Yin, Z. & Zhang, H. Preparation and Applications of Mechanically Exfoliated Single-Layer and Multilayer MoS_2 and WSe_2 Nanosheets. *Acc. Chem. Res.* **47**, 1067–1075 (2014).

11. Li, X. *et al.* Layer-Number Dependent Optical Properties of 2D Materials and Their Application for Thickness Determination. *Adv. Funct. Mater.* **27**, 1604468 (2017).

12. Li, H. *et al.* From Bulk to Monolayer MoS_2 : Evolution of Raman Scattering. *Adv. Funct. Mater.* **22**, 1385–1390 (2012).

13. Guo, Y. *et al.* Distinctive in-Plane Cleavage Behaviors of Two-Dimensional Layered Materials. *ACS Nano* **10**, 8980–8988 (2016).

Chapter 3 Development of in-situ stretching TEM chip for 2D materials

Introduction

Understanding the mechanical behavior of MoS_2 under tensile stress is critical for both fundamental research and device applications. *In situ* transmission electron microscopy (TEM) provides a powerful platform for capturing real-time structural evolution during deformation. However, the reliability and interpretability of such observations heavily depend on the design of the tensile testing chip. Conventional tensile chips often suffer from limitations such as poor mechanical stability, wide tensile gaps, and relatively high tensile rates, making it difficult to capture the tensile process under TEM. These issues are particularly pronounced when stretching 2D materials, where even a small tensile distance or a low tensile rate will hinder the obtain of the clear *in situ* TEM results. To address these challenges, we explored a new tensile chip design that emphasizes mechanical integration, alignment control, and compatibility with *in situ* TEM environments. The following sections will detail the rationale behind this design, with particular emphasis on the advantages of connected-end structures over traditional independent-end setups.

3.1 Limitations of the independent-end design

In earlier work conducted within our research group, *in situ* TEM tensile experiments were performed using two separately supported Si chips mounted on a titanium (Ti) plate. These structures, where the two ends of the sample were not mechanically connected, were used to suspend few-layer MoS_2 nanosheets across the gap between the chips. This configuration successfully enabled observation of structural phenomena such as the formation of ripple patterns under applied tensile strain, providing direct evidence of strain-induced out-of-plane deformations in two-dimensional materials. The corresponding experimental setup and schematic mapping of strain distribution on the Ti support are illustrated in Figure 3.1, which highlights the early sample rod design and the characteristic deformation field that develops during loading.

Despite the success of this approach in capturing ripple evolution[1,2], follow-up experiments revealed critical limitations of the independent-end configuration. Most notably, the Ti substrate exhibited slight but unavoidable bending and local deformation when tensile force was applied. In the absence of a mechanical connection between the two silicon chips, this deformation led to asymmetric height displacements at the sample ends and introduced significant uncertainty in the actual strain experienced by the MoS_2 flake. This substrate-induced distortion caused inconsistencies in strain transfer and frequently resulted in unstable or non-uniform mechanical loading across the suspended region.

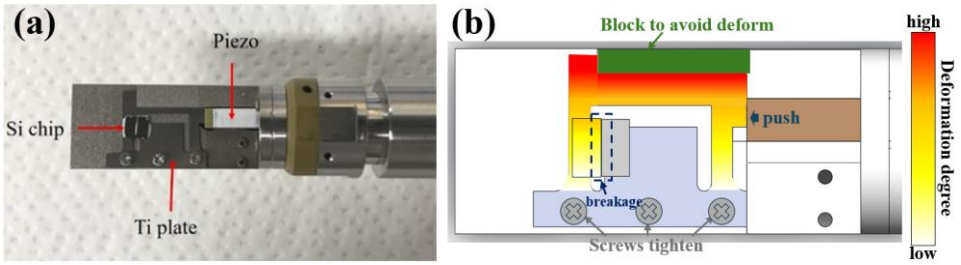

Figure 3.1 Top-view of the previously used sample holder structure and schematic strain mapping on the Ti support during tensile loading

A more pronounced issue emerged from the vertical mismatch introduced by the bending of the Ti support. During tensile loading, even a small out-of-plane deflection between the two silicon chips could result in substantial shifts in the TEM observation area, especially under high magnification. This effect is clearly illustrated in Figure 3.2, which presents a schematic side-view of the experimental configuration, highlighting the relative height changes between the two ends as a function of substrate deformation. Such misalignment frequently causes loss of focus or drift of the imaging window, thereby limiting the ability to track localized structural events such as fracture initiation or defect migration with temporal and spatial continuity.

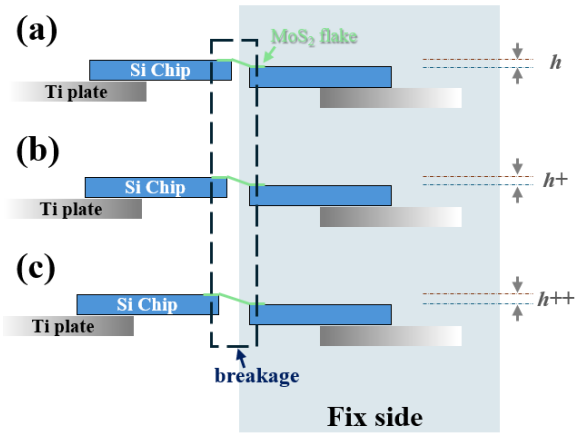

Figure 3.2 Schematic side view of the tensile setup showing relative height change between two unconnected silicon chips induced by deformation of the Ti support during stretching.

3.2 The design of the new in-situ stretching TEM chip

Building upon the limitations identified in Ti-supported, independent-end chip designs, we developed a new custom Si chip with an integrated, connected-end structure to improve mechanical stability and observational control during *in situ* TEM tensile testing. In this chip, a narrow slit (0.5 mm in length and 30 μm in width) is introduced on one side of the silicon substrate, defining a mechanically flexible zone where a thin silicon nitride (SiN_x) membrane is suspended.

The SiN_x layer, with a nominal thickness of 400 nm, is first deposited onto the silicon wafer—typically via chemical vapor deposition (CVD) or similar industrial thin-film methods. Following deposition, the silicon is etched away from the backside to form a freestanding SiN_x window in the region adjacent to the open slit. This area serves as the TEM observation window, enabling electron transparency while preserving sufficient mechanical strength for stretching experiments.

Figure 3.3(a) shows the schematic design and critical dimensions of the chip layout. The Si chips are designed to be rectangle shape of 2.5 × 3.0 mm in size, which is fully covered with 400 nm-thick SiN_x membrane and have gold electrodes as shown in Figure 3.3(a). In this slit, a narrow gap of about 100 nm in spacing is fabricated by focused ion beam (FIB) to suspend the MoS_2 nanosheet.

The Si chip is mounted on the Ti plate using silver paste as shown in Figure 3.3(b). The gap spacing gradually widens when increasing the applying voltage to the piezoelectric actuator.

Owing to the structural configuration, the change ratio of the gap spacing becomes reduced when the fixing position of the Si chip is close to the fixed side of the Ti plate. It means that the Ti plate is not deformed uniformly as shown in Figure 3.3(c). The fixing position of the Si chip can be determined depending on how much the gap spacing should be widened.

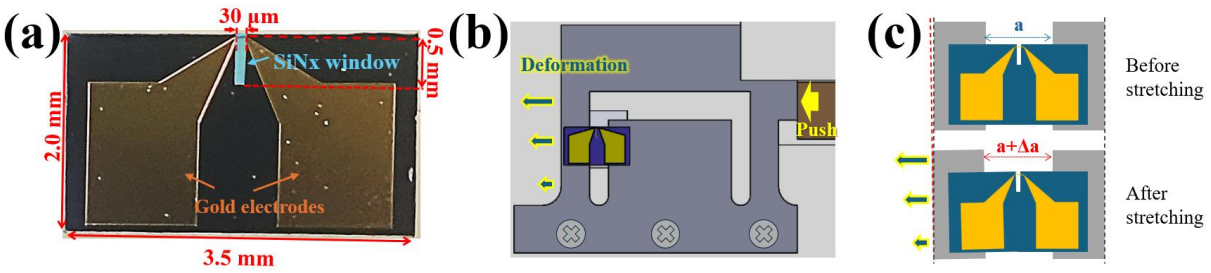

Figure 3.3 (a) Top-view image of the fabricated chip showing the physical layout. (b) Photograph of the chip mounted on a titanium support plate using silver paste. (c) Schematic picture of the Si chip before and after tensile loading.

To evaluate the actual tensile performance of the SiN_x window region under in situ conditions, we used focused ion beam (FIB) processing to mill a narrow gap, 0.5 mm in length, along the long axis of the membrane adjacent to the observation window (Figure 3.4(a)). This FIB-milled gap served as a direct mechanical readout for tracking the extent of strain during TEM tensile experiments.

By gradually increasing the voltage applied to the piezoelectric actuator, we were able to continuously record the elongation of the gap within the TEM. As shown in Figure 3.4(b), the gap maximum opening side stretching distance increased linearly with applied voltage, demonstrating the reliability and controllability of strain transfer through the chip structure. Importantly, this configuration allowed the minimum resolvable displacement to be reduced from ~4 μm in previous designs to less than 0.7 μm, enabling high-resolution control over local

tensile strain during real-time TEM imaging.

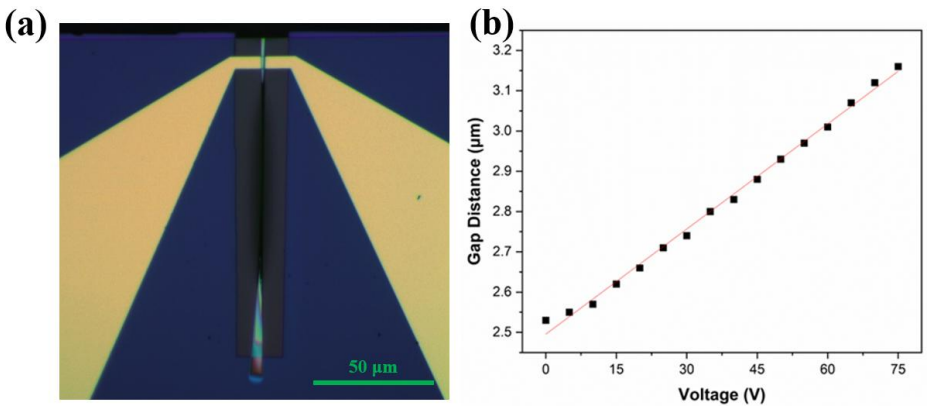

Figure 3.4 (a) Optical image of the SiN_x window region after focused ion beam (FIB) milling of a 0.5 mm slit aligned along the long axis. (b) Displacement of the FIB slit during *in situ* TEM stretching as a function of applied piezoelectric voltage, showing a linear relationship and demonstrating precise tensile control.

3.3 Design strategies for stretchable structures

3.3.1 Deformation response of hole(s) in SiN_x membrane

In this subsection, we explore the deformation behavior of a circular hole design that aligns with the practical machining resolution of our focused ion beam (FIB) system. Based on the minimum achievable milling precision, we designed a through-thickness hole with a radius of 0.5 µm at the center of the SiN_x membrane window to evaluate its mechanical response under tensile loading.

The simulation model, shown in Figure 3.5(a), includes the electrode region and suspended SiN_x layer. The area surrounding the hole is magnified in Figure 3.5(b) for clarity. Three distinct loading points were selected and marked with different colored lines to study the

sensitivity of the hole's deformation to tensile loading positions. These three distinct loading points represent the silver paste fixing process caused inhomogeneous binding strength, the stress concentrated on different positions when stretching.

The simulated strain distribution resulting from 1 mN force application at surface of position 1 is shown in Figure 3.5(c), with the right side of the chip fixed, then the same force was applied to the surface of position 2 and position 3, respectively. The maximum deformation and the minimum deformation of the hole while applying the forces were recorded in Figure 3.5(d), comparing the strain responses at all three loading positions. The results show that the deformation of the designed hole structure is too small to induce a considerable detectable strain when suspending the MoS_2 flakes on it after applying tensile loading, the largest deformation is smaller than 0.25 nm. In this simulation, we used an equivalent system to predict nanoscale changes.

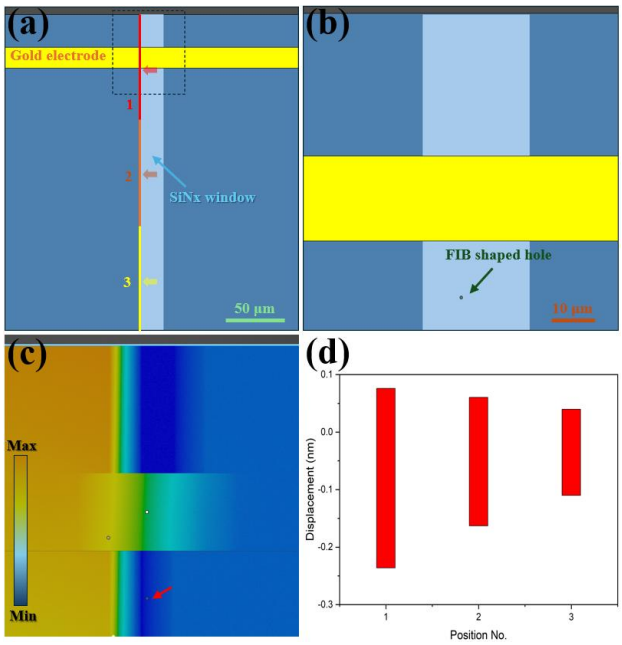

Figure 3.5 (a) ANSYS model of the SiN_x membrane and electrode region, with a circular hole (0.5 μm

radius) located ~25 μm below the electrode. The dashed box indicates the magnified region in (b). (b) Enlarged view of the hole region from (a). All scale bars are indicated in the lower right corner of each panel. (c) Simulated strain distribution resulting from a force applied at Point 1, as marked in (a). (d) Comparison of deformation ranges around the micro-hole under three different loading positions.

Given the limited strain localization observed with a single micro-hole structure, we further explored design strategies aimed at amplifying the stress concentration in the central sample region. Specifically, we investigated two modifications: (1) thinning the support region where the sample is mounted, and (2) introducing multiple serially connected holes to form a stress-guiding path. These measures were intended to enhance deformation localization in the functional area during tensile loading.

As shown in Figure 3.6(a), a serial-hole structure was fabricated by focused ion beam (FIB) milling in a thinned region of the SiN_x membrane. MoS_2 flakes were then transferred onto the designated mounting area. Upon applying tensile force, the chip fractured unexpectedly, as depicted in Figure 3.6(b). Interestingly, the crack did not propagate solely along the serial holes; instead, additional branching cracks appeared in multiple directions. We interpret this as indirect evidence of residual fabrication-induced stress[3], which likely contributed to the observed complex fracture patterns.

Figures 3.6(c) and 3.6(d) capture the TEM tensile testing process using the serial-hole design. The initial structural state prior to loading is shown in (c), while (d) reveals the final fractured state. Although some deformation near the thinned SiN_x region was observed, the lack of precise control during tensile loading highlights the need for more robust and controllable slit designs in future iterations. In addition, the fractured result also indicates the

need to add a protective structure at the bottom of the structure fabricated.

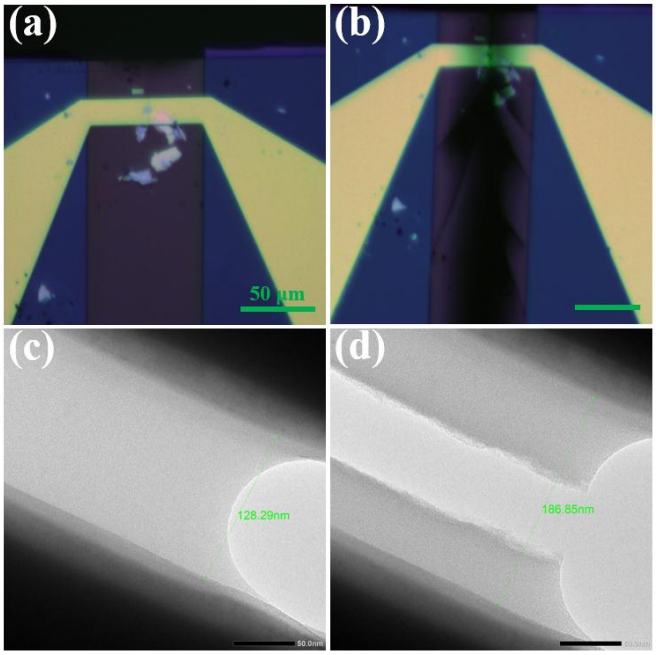

Figure 3.6 (a) FIB fabricated serial-hole structure in the thinned sample-support region of the SiN_x membrane. (b) Fracture morphology of the chip after tensile loading, showing both longitudinal and branching cracks. (c) TEM image of the serial-hole structure before in-situ tensile testing. (d) Post-stretching TEM image showing fracture formation and partial deformation near the thinned membrane region.

3.3.2 Evaluation of long gap designs for improved stretching performance

Building upon the promising stretching capability demonstrated by the previous chip design, we explored more effective slit geometries to enhance strain localization and structural controllability. Specifically, two configurations were investigated:

(1) Long gap starting from the front open edge of the SiN_x observation window, and

(2) Long gap initiated near the electrode region.

Both structures were fabricated using FIB milling and examined under an optical

microscope, as shown in Figures 3.7(a) and 3.7(b).

In the configuration shown in Figure 3.7(a), a MoS_2 flake was transferred onto the gap. However, severe downward deflection (sagging) was observed on both sides of the milled slit, particularly at the very tip of the open end. The slit, measuring 150 μm in length, exhibited a central deflection of up to ~4 μm. This large deformation caused significant challenges during sample transfer, especially in achieving uniform contact across both ends of the MoS_2 membrane, resulting in poor anchoring stability.

To address this, a second design was implemented with the gap milled starting from the electrode side (Figure 3.7(b)). While this approach aimed to mitigate sagging near the open edge, the gap-end near the exterior anchor point fractured during installation. Optical inspection revealed that a small section near the terminus of the gap remained structurally intact without visible deflection. To further reduce the likelihood of crack propagation during tensile testing, we introduced a T-shaped terminus structure at the slit endpoint to buffer the stress concentration.

We then quantitatively assessed the degree of sagging along the gap. A simplified analytical model was used to estimate the edge deflection of a rectangular SiN_x membrane with two fixed boundaries $b \times a$ (150 μm × 15 μm) under a built-in tensile stress (σ_0) of 100 MPa. The observation window was 30 μm wide.

The deflection of the membrane after the built-in tensile stress released can be evaluated by the following equations, let's describe the shape of the sagging membrane:

$$\omega(x,y) = \omega_0 \cdot (1 - \cos(\frac{\pi x}{2a})) \cdot (1 - \cos(\frac{\pi y}{2b})) \quad (3.1)$$

Where,

$\omega(x,y)$: $The\ deflection\ at\ the\ point\ (x,y), deformation\ are\ along\ z\ direction$

ω_0: $The\ maximum\ deflection, usually\ appears\ at\ one\ end\ of\ a\ diagonal\ line\ \ (in\ this\ case: a = 15\ \mu m, b = 150\ \mu m)$

The built-in tensile stress is common to be found in membranes like SiN_x after deposition or fabrication[3]. After the tensile stress is released, it is equivalent to generating an equivalent internal moment (M) in the cross section:

$$M = \sigma_0 \cdot \frac{h}{2} \cdot a \quad (3.2)$$

Where,

σ_0: $built - in\ tensile\ stress, in\ this\ case, we\ use\ 100MPa$

h: $thickness\ of\ the\ mambrane$

According to the thin plate bending theory, the maximum deflection ω_0 is:

$$\omega_0 = \frac{Mb^2}{2EI} \quad (3.3)$$

$$I = \frac{ah^3}{12} \quad (3.4)$$

Where,

σ_0: $built - in\ tensile\ stress, in\ this\ case, we\ use\ 100MPa$

b: $the\ deflection\ is\ dominated\ \ by\ the\ size\ on\ b$

E: $Young's\ modular, 250\ GPa\ for\ SiN_x$

h: $thickness\ of\ the\ mambrane$

The ω_0 can be estimated by the combination of formular (3.3) and (3.4), and then generalize to plates:

$$\omega_0 \approx \frac{\sigma_0 b^2}{Eh} \cdot \alpha \tag{3.5}$$

Where,

α: $empirical\ coefficienct, for\ SiN_x\ membrane, \alpha \sim 0.1 - 0.3,$

$in\ this\ case, we\ use\ \alpha = 0.2$

As shown in Figure 3.7(c), the open-end deflection ω_0 was calculated to be approximately 4.5 μm—consistent with experimental observation. A rough statistical analysis of the slit-edge deformation indicated that within the first 1.5 μm from the slit origin, see in the table 3-1, the edge remains extremely stable with only sub-nano deflection (~0.55 nm), which is fully compatible with TEM imaging requirements. This structurally optimized slit configuration was thus improved further for subsequent in-situ tensile testing experiments. While, of cause the deflection of the membrane might not only be caused by the built-in tensile stress, also the fabrication process of the FIB will induce Ga^{3+} that form the deflection, the mechanism of this process is complicated, what we can do to simplify the calculation is to measure the maximum deflection of the membrane and insert the value to the formular (3.1).

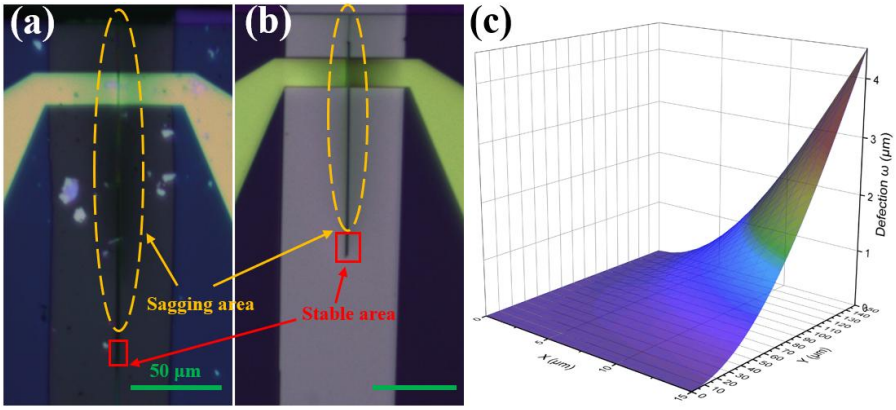

Figure 3.7 (a) Optical image of a FIB-fabricated slit starting from the front open edge of the observation window. Severe sagging is observed at the tip of the slit. (b) Slit structure fabricated from the electrode side, showing improved mechanical stability at the tip, but partial fracture near the outer anchoring region. A T-shaped terminus was designed to mitigate crack propagation. (c) Calculated deflection of a 150 μm × 15 μm SiN_x membrane under 100 MPa internal tensile stress, showing a 4.5 μm deflection at the open edge.

Table 3-1 Different deflection from y=0 to 150 μm, with the fixed x=15 μm

y (μm)	**Deflection *(μm)***
0.0	0.0
0.1	0.0000186
0.5	0.0000930
1.0	0.000278
1.5	0.000555
2.0	0.001019
5.0	0.0062
10.0	0.02468
50.0	0.40291

100.0	2.25002
150.0	4.50

3.3.3 Optimization of long gap geometry

To further improve the structural stability of the long gap design during in-situ tensile testing, we optimized the FIB milling process based on prior fabrication experience. The final result is shown in Figure 3.8(a), which presents an optical image of the observation window region after FIB processing. A magnified view of the mechanically stable region near the window is displayed in inset Figure 3.8(a). In this refined configuration, a T-shaped terminus was introduced at the end of the slit. This feature serves to prevent fracture of the SiN_x membrane under tensile stress, while also allowing the fabrication of narrower slit geometries suitable for varying experimental stress conditions.

Two square holes, also shown in Figures 3.8(a) and inset (a), were simultaneously fabricated during the FIB process. These serve as fiducial markers to assist with the precise positioning of the transferred sample in the central slit region.

To evaluate the tensile performance of the T-shaped gap, we conducted tensile loading tests in TEM. As shown in Figures 3.8(b) and 3(c), the gap expanded from 238 nm at 0 V to 261 nm under 75 V, yielding a total elongation of approximately 23.5 nm. The T-shaped gap remains clearly identifiable before and after tensile loading, confirming structural integrity. The elongation of the gap spacing versus the applied voltage relationship is plotted in Figure 3.8(d),

demonstrating a highly controllable and nearly linear response. For instance, applying voltage at 0.3 V/s results in a displacement rate of ~0.1 nm/s. This corresponds to a strain rate of approximately 0.042% per sec. for the gap with distance of 238 nm. Finer strain-rate such as 0.004% per sec. can be achieved by adjusting the voltage step. Such a strain rate is quite low compared with the previous studies (displacement rate over 5 nm/s, corresponding to strain rate over 0.17%). A 23.5 nm elongation corresponds to ~10% strain for a gap width of ~235 nm, and since FIB milling can produce sub-100 nm gaps, even higher strain levels are attainable with narrower structures.

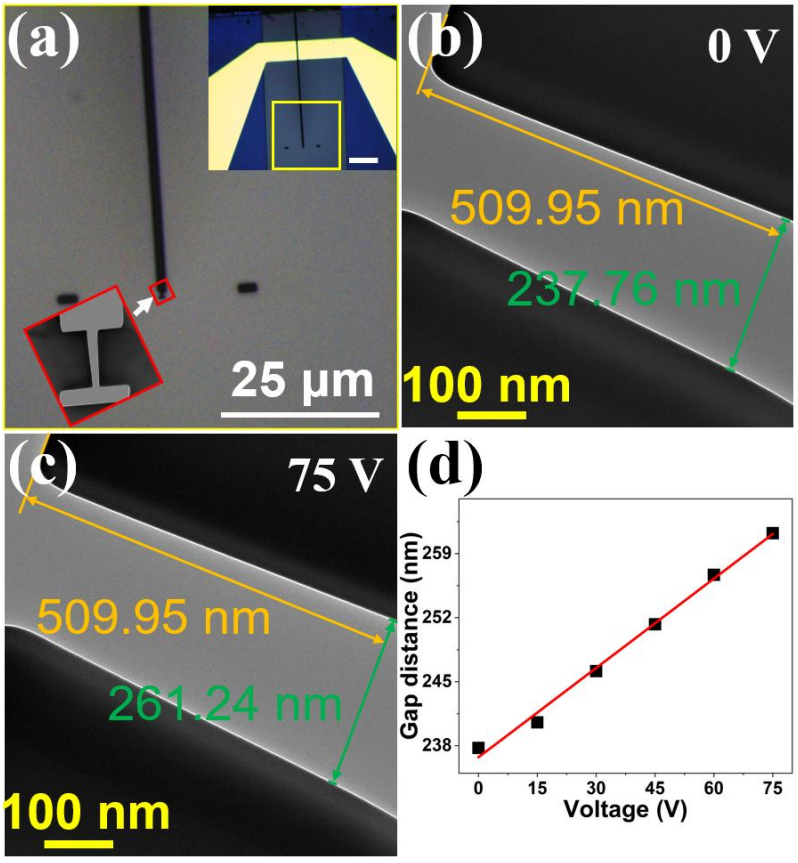

Figure 3.8 (a) Enlarged picture of the FIB shaped widow area marked with yellow rectangle in inset (a). (b) The gap distance in "T" structure (marked out with a white arrow in (a)) of 237.76 nm at 0V voltage, and (c) the distance of 261.24 nm with 75V voltages applied. (d) Measured displacement of the T-shape gap under increasing applied voltage, demonstrating a linear piezo response with a maximum elongation of ~23.5 nm.

3.4 In-situ tensile testing on the well-designed structures

To validate the tensile chip design, we conducted in situ tensile loading experiments on MoS_2 samples transferred onto the fabricated gap structures. Optical images of three representative samples over the T-shaped gap tips are shown in Figure 3.9 (a–c), with corresponding TEM images in Figure 3.9(d–f), confirming proper alignment and suspension.

The first two samples (Figures 3.9(a, d) and 3.9(b, e)) used the T-shaped gap design, demonstrating successful transfer and positioning for tensile testing. T-shaped gap is suitable for investigating the tensile deformation process. Furthermore, we found that a non-T-shaped gap is suitable for investigating not only tensile deformation process but also shear deformation process. The third configuration (Figures 3.9(c, f)) employed a non-T-shaped gap, enabling the narrowest gap width smaller than the nominal ~100 nm FIB resolution.

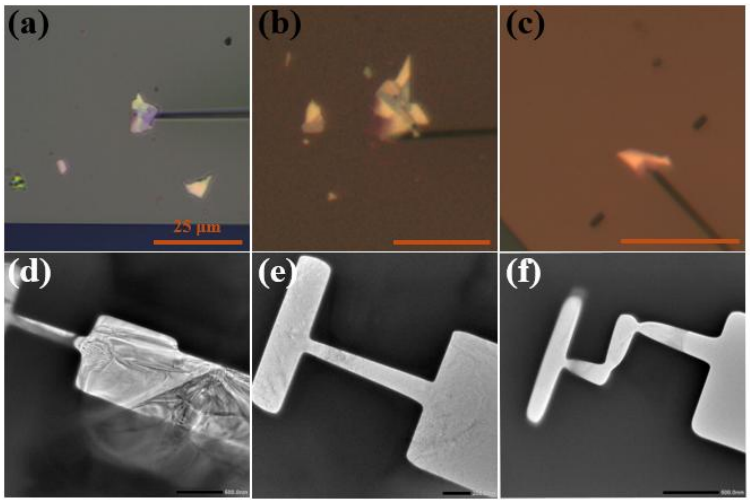

Figure 3.9 (a–c) Optical microscope images showing three MoS_2 samples transferred onto tensile chip structures. (d–f) Corresponding TEM images confirming successful suspension over the slits. The structure in (f) demonstrates a sub-100 nm slit width, with the narrowest point around 60 nm, enabling atomic-resolution imaging during in-situ tensile testing.

To further validate the effectiveness of our tensile chip design, Figures 3.10(a–c) shows atom-resolved TEM images of three different suspended MoS_2 nanosheet prior to tensile loading, while Figures 3.10(d–f) presents their corresponding states after tensile deformation. Notably, high-resolution atomic images could be acquired during the tensile loading process, indicating the mechanical stability and imaging compatibility of our tensile platform. This level of stability is critical, as it allows for real-time atomic-scale observation of fracture evolution in 2D materials. The fracture process can be clearly observed in the in situ videos.

Building on this capability, our observations reveal a extroadinary phenomenon from the conventional understanding of tensile fracture in MoS_2 flakes. Unlike the typically brittle behavior reported in prior studies[4–6] where cracks propagate along a single path with smooth and clean edges, and all layers rupture simultaneously. But, such fracture phenomena were not observed in our TEM observation. As shown in Figures. 3.10(d–f), the crack morphologies display features such as blunted or irregular tips, deflected paths, and the non-simultaneous rupture across layers, all indicative of ductile-like fracture behavior[7–9].

We think that the fracture mechanisms in the MoS_2 nanosheet may change from brittle-like to ductile-like, when tensile strain is applied at sufficiently low rates. In our tensile test, we observed void-to-void fracture process. The void-to-void fracture process originates from pre-existing or strain-induced defects that are randomly distributed within the nanosheet. Under applied tensile strain, these defects evolve into nanoscale voids, which tend to grow in a direction perpendicular to the loading axis due to local stress concentration. As deformation progresses, adjacent voids connecting or crack extension, eventually forming a connected

fracture path that leads to final fracture. Additionally, we didn't observe creep deformation during tensile loading. The deformation progressed continuously with the applied displacement, without any noticeable time-dependent strain accumulation or deformation lag. This indicates that the observed deformation behavior is not creep but rather a direct response to the applied tensile loading.

This ductile-like behavior under low-rate conditions has not been previously reported in tensile fracture studies. This reason may come from limitations in strain-rate control and lack of spatial resolution. Our method has an advantage of elucidating the mechanical response and failure mechanism of two-dimensional (2D) materials, since we can obtain the atom-resolved TEM images by controlling the strain rate during tensile loading.

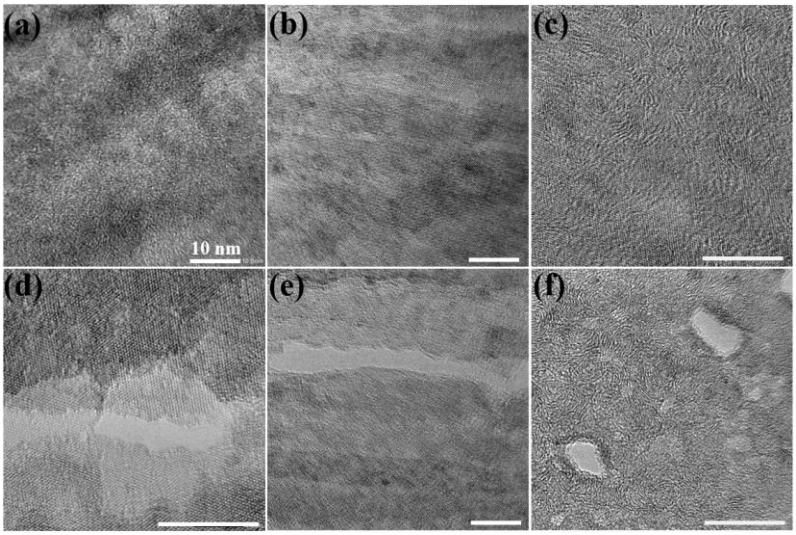

Figure 3.10 (a–c) Atomic-resolution TEM images of MoS_2 samples before stretching. (d–f) Corresponding post-stretching images, demonstrating structural stability and observation continuity at the atomic scale during in-situ tensile testing.

Conclusion

In this chapter, we introduced a newly developed in-situ tensile chip designed to improve mechanical stability and observation reliability during TEM-based tensile testing of two-dimensional materials. The work began with an analysis of the limitations associated with earlier structures—specifically, independent silicon pieces supported by deformable titanium plates—which often led to undesirable out-of-plane motion and compromised the accuracy of atomic-level observations. These drawbacks were visualized through top-view and side-view characterizations of the earlier design (Figure 3.1).

To address these challenges, we proposed a new chip layout featuring a connected silicon frame with a SiN_x window layer and strategically introduced slits for localized deformation control. The fabrication process and structural layout were detailed, supported by a series of optical and schematic illustrations (Figures 3.3 and 3.4), as well as mechanical performance validation based on in-situ TEM measurements. These measurements demonstrated a linear relationship between applied voltage and slit displacement, confirming controllable tensile actuation with sub-micron precision.

We further explored several stress-concentration strategies, including single and serial nano-holes as well as localized thinning of the SiN_x membrane. Although these approaches showed partial effectiveness, simulations and experimental data indicated limitations in mechanical reliability. Consequently, we transitioned to a long-narrow slit design, which proved to provide a more uniform and stable deformation field. Finite element simulations

(Figure 3.5) and systematic structural comparisons (Figures 3.6–3.8) demonstrated the advantages of this approach, particularly when combined with protective T-shaped termini to mitigate stress concentration at the slit ends.

Finally, successful transfer and atomic-resolution imaging of MoS_2 samples on the final chip design (Figures 3.9 and 3.10) validated the practical utility of this new tensile platform. The chapter lays a solid foundation for high-precision in-situ mechanical testing of 2D materials, enabling direct correlation between mechanical deformation and atomic-scale structural evolution.

References

1. Xie, L. & Oshima, Y. Quantitative estimation of atom-scaled ripple structure using transmission electron microscopy images. *Nanotechnology* **32**, 185703 (2021).
2. Xie, L. & Oshima, Y. Nonlinear mechanical response of rippled MoS2 nanosheets evaluated by in situ transmission electron microscopy. *Appl. Surf. Sci.* **597**, 153708 (2022).
3. Huff, M. Review Paper: Residual Stresses in Deposited Thin-Film Material Layers for Micro- and Nano-Systems Manufacturing. *Micromachines* **13**, 2084 (2022).
4. Li, P. *et al.* In situ nanomechanical characterization of multi-layer MoS_2 membranes: from intraplanar to interplanar fracture. *Nanoscale* **9**, 9119–9128 (2017).
5. Yang, Y. *et al.* Brittle Fracture of 2D $MoSe_2$. *Adv. Mater.* **29**, 1604201 (2017).
6. Li, B. *et al.* Anisotropic Fracture of Two-Dimensional Ta_2 $NiSe_5$. *Nano Lett.* **24**, 6344–6352 (2024).
7. Wang, G. *et al.* Engineering the Crack Structure and Fracture Behavior in Monolayer MoS_2 By Selective Creation of Point Defects. *Advanced Science* 2200700 (2022) doi:10.1002/advs.202200700.
8. Yang, Y. *et al.* Intrinsic toughening and stable crack propagation in hexagonal boron nitride. *Nature* **594**, 57–61 (2021).
9. Wang, S. *et al.* Atomically Sharp Crack Tips in Monolayer MoS_2 and Their Enhanced Toughness by Vacancy Defects. *ACS Nano* **10**, 9831–9839 (2016).

Chapter 4 Ductile-like fracture of MoS_2 nanosheets

Introduction

Exploring the atomic-scale mechanical properties of two-dimensional materials is limited due to the lack of experimental methods. In this study, we have investigated the fracture mechanism of few layers MoS_2 nanosheets at the atomic scale by *in situ* stretching transmission electron microscopy real time observation. In-situ stretching was achieved using a custom-designed stretching holder integrated with a specially engineered chip that ensures atomic resolution stability during experiment. We found that the few layers MoS_2 showed the formation of the stepped fracture structures when stretching along the direction near armchair orientation, and the results reveal that cracks propagated along zigzag edges at different locations across distinct layers. Furthermore, the fracture process exhibits characteristics of ductile-like behavior. These fracture behaviors, unreported before in MoS_2, highlight the new mechanism of the fracture process in few-layer MoS_2. The crack propagation can be distributed to the fact that zigzag edges have lower crack formation energy than armchair edges. We calculated the fracture width of few-layer MoS_2 and found that the width of the stepped structures is approximately 10 nm. Additionally, we conduct a zigzag direction's stretching of MoS_2 nanosheet, the results also exhibit ductile fracture. These results coincide with the former fracture structure observation. This finding provides new insights into the fracture mechanics

of 2D materials and has potential implications for their mechanical stability and device applications.

4.1 Stretching fracture of MoS_2 multilayer films

To clarify the fracture mechanism of 2D materials, several approaches, including experimental and theoretical methods, have been achieved. The fracture process has been directly observed by transmission electron microscopy (TEM) [1–3], while fracture model has been proposed by molecular dynamics (MD) simulation[4–6] and first-principle calculations[7,8]. Recently, *in situ* electronic microscopy method has been developed[3,9–15] and the fracture mechanism of 2D materials have been investigated at an atomic scale[1,11,16,17].

However, the aforementioned experimental results either involve fractures not induced by tensile loading, or the tensile-induced fractures lack atomically resolved characterization. Previous studies have shown that fracture behavior in monolayer MoS_2 is regulated by defects, with the fracture mechanism shifting from brittle to ductile-like as defect density increases. For layered TMD nanosheets, fracture typically remains brittle, often exhibiting atomically flat fracture edges[13,18]. Although strong interlayer coupling has been widely reported in 2D materials, particularly in transition metal dichalcogenides (TMDs)[19], which suggests that fracture in MoS_2 should be predominantly brittle.

When the MoS_2 multilayer film was broken by stretching, the fracture edges showed sawtooth pattern with the angle of about 120° as shown in Figure 4.1(a). Figure 4.1(b) and (c)

are TEM images of the areas shown in red and black frames, respectively, in Figure 4.1(a), and Figure 4.1(d)-(f) are atom-resolved TEM images of the areas shown in yellow, green and bule frames, respectively, in Figure 4.3(b). We found that several nanometer-scale steps were formed along the zigzag (ZZ) edge as shown in Figure 4.1(d)-(f) and they were bunched to form one large step as shown in Figure 4.1(b) and (c). The sawtooth pattern reflects the breakage at the ZZ edges. This result is consistent with the result of density functional theory (DFT) calculations[20]. The formation energy of the ZZ edg (0.90 eV/Å) is calculated to be lower than that of the armchair (AC) edge at 0.95 eV/Å. The interval between large steps was about 0.5 μm and more. On the other hand, the interval of the nanometer-scale steps was approximately 10-20 nm.

About fracture of a layer in the film, defects are thought to trigger the propagation of cracks along ZZ edges[16,21], forming elongated voids, which ultimately lead to the fracture of the entire layer. Since the fracture sites are approximately 10 nm apart between layers, it can be said that the fracture does not directly propagate to the adjacent layer such as intralayer fracture or interplanar[11]. Additionally, on a larger scale, such fracture processes triggered by defects are naturally considered to occur almost simultaneously in various locations within the film, and the fractures must continue until the film is completely broken.

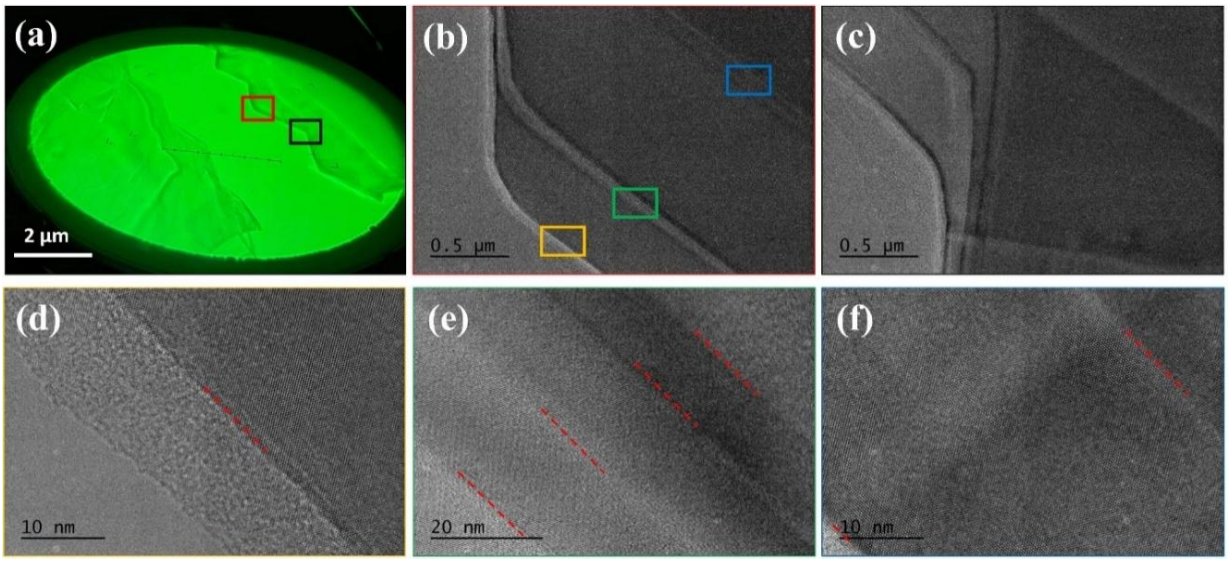

Figure 4.1. Images of MoS_2 nanosheet after the fracture. (a)The image of the fracture region at low magnification. (b)-(c)TEM images of the fracture regions marked by red and black frames in (a), respectively. (d)-(f) The TEM images of the fracture edges, correspond to the regions marked by yellow, green, and blue frames in (b), respectively. The red dashed lines indicate the edges of the different layers in the sample. [XIE Lilin, Doctor's thesis, JAIST, 2021, P62]

Furthermore, the fracture with stepped structures can be explained by the weak interlayer interaction of MoS_2. The interlayer binding energy of MoS_2, which is 0.55 ± 0.13 J m^{-2} obtained from the peeled flake[22], is significantly smaller than the surface energy, which is ~1.8 J m^{-2} estimated from the DFT calculation[13]. Thus, the interlayer fracture is preferred for the multilayer MoS_2 since it is difficult for the crack penetrates the layers through the interlayer interaction. Though, the previous report[2] observed by *in situ* TEM observation has shown that the fracture of 2D materials is almost identical for the bilayers and monolayer, and suggested that stress/strain could transmit through layers. While, such transmitted stress seems to be induced by coeffect of the irradiation deformation force and the defect migration. We should point out that the multilayer MoS_2 in our experiment was stretched with an in-plane tensile strain by the *in situ* TEM holder, so that we could observe the formation of the fracture with

atomically stepped structures.

4.2 Experimental setup

4.2.1 Thickness selection of MoS_2 flakes

Natural bulk MoS_2 (FUJI PHOTO FILM CO., LTD, JP) were used for preparation of mechanical exfoliated MoS_2 nanosheets, then the exfoliated MoS_2 nanosheets were deposited onto the cleaned 285 nm SiO_2-coated Si substrate.

The MoS_2 nanosheet selected for the experiment exhibited a stepped structure after exfoliation. Its suitability was confirmed by optical contrast analysis, ensuring that the thinner edge had a thickness of only a few layers[23]. The zigzag orientation was distinguished based on the flatness of the nanosheet edges.[21] The target MoS_2 nanosheet was then dry transferred by aligning the flat edge or its ±60° rotated direction perpendicular to the stretching direction, thereby ensuring that the zigzag orientation was oriented perpendicular to the applied strain.

In situ TEM experiment was then performed by JEM-2100plus (JEOL) with an accelerating voltage of 120 kV after mounting the stretching chip on the *in situ* stretching TEM holder[24] by silver paste. The tensile rate was controlled at approximately 0.1 nm/s.

Figure 4.2(a) shows the optical microscope image of mechanically exfoliated standard terraced structured MoS_2 flake. Figure 4.2 (b) illustrates Raman spectra of the MoS_2 flake with varying layers obtained using 532 nm laser line, the main Raman peaks in this spectrum

correspond to the zone center first order E_{2g}^{1} mode at ~384 cm^{-1} and the A_{1g} mode at ~409 cm^{-1}. The corresponding layer number can then be identified by calculating the position difference between the E_{2g}^{1} peak and the A_{1g} peak.[25] As marked on the Raman curves in distinct colors.

The method of calibrating the number of layers by contrast is considered to be a fast and efficient method for calibrating the number of TMDs layers, especially in the calibration of the number of layers of few-layer TMDs, such as MoS_2 and WSe_2.[23] According to the contrast calculate method. The contrast-layer number results of the standard flake can then be plotted in Figure 4.2(c), the plotted values represent C_{ZR} (contrast difference between sample and substrate in red channel), C_{ZG} (contrast difference between sample and substrate in green channel), and C_{ZB} (contrast difference between samples and substrate in blue channel) for 1L-4L, 6L, 7L and bulk MoS_2 nanosheet, respectively. Then C_{ZR} acquire from the areas marked out by red rectangular in 4.2 (d) is calculated. Due to the image resolution of target flake is not very high, the measured contrast value fluctuates greatly within the edge width. We calculate 3 contrast areas of the edge, and the calculated result is a range from -51 to -28. Although we cannot get an exact contrast value, this data still shows that the thickness of the edge structure is within 7 layers.

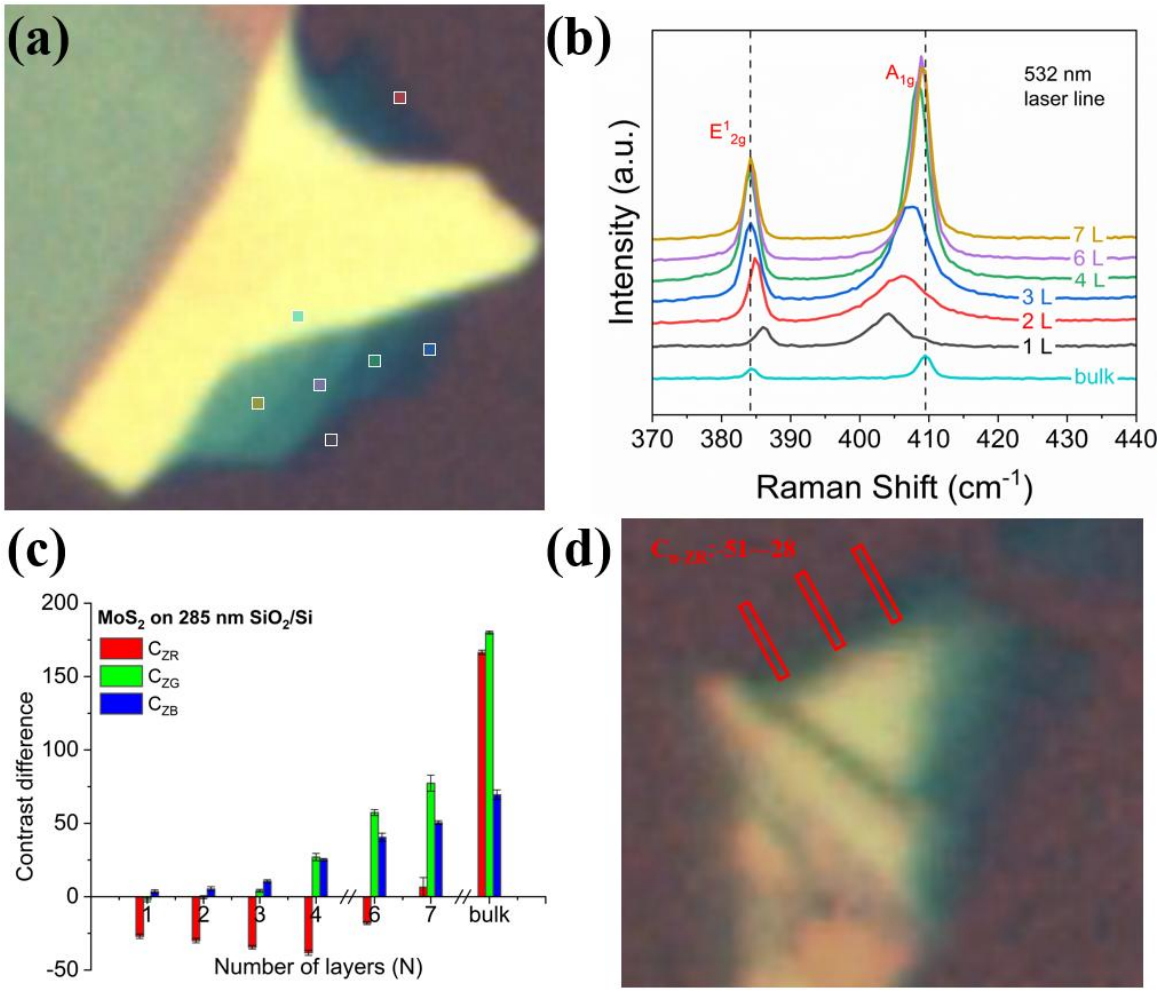

Figure 4.2 (a) Optical microscope image of terraced structural MoS_2 flake. (b) Raman spectra of different thicknesses of MoS_2 nanosheet using 532 nm line. The right and left dashed lines indicate the position of A_{1g} and E^1_{2g} peaks of bulk MoS_2, respectively. (c) Normalized contrast differences between samples and substrates C_{ZR}, C_{ZG}, and C_{ZB} values of 1L-4L, 6L, 7L and bulk MoS_2 nanosheet. (d) Selected MoS_2 flake with the C_{ZR} value of -51~-28.

4.2.2 In situ TEM experimental setup and pre-strain treatment

In our previous experiments, we found that the fracture of MoS_2 flakes is accompanied by a step-like fracture edge with a width of about 10-20 nm (Figure 4.1), arrange along zigzag (ZZ) direction. To better understand the formation of fracture edges in MoS_2 nanosheets under tensile loading, we performed an *in situ* stretching experiment, enabling real-time observation

of edge formation. Figure 4.3(a) shows the top view and corresponding 3D model of the holder used in the experiment. When a voltage is applied to the piezoelectric component, the customized chip undergoes a stretching motion. The resulting frame deformation is transferred to the nanosheet via a precisely designed slit on the chip.

The stretching performance of the slit was characterized, revealing a linear increase in the slit gap with increasing applied voltage. This relationship is shown in Figure 4.3(b), indicating a well-controlled and predictable stretching rate throughout the experiment. Figure 4.3(c) presents a MoS_2 flake with a terraced structure, imaged before and after the dry transfer process. The thinner edge of the flake was accurately cover the experimental area.

Figure 4.3(d) displays the suspended MoS_2 nanosheet across the slit, representing the entire stretching region. As seen in the figure, the MoS_2 flake was successfully transferred onto the stretching area. No significant contrast variation is observed across the region, indicating uniform thickness of the transferred nanosheet within the observation area.

The magnified TEM image of the region marked by the red square in Figure 4.3(d) is shown in Figure 4.3(e). The MoS_2 flake exhibits a relatively high-quality crystalline structure, as confirmed by the corresponding Fast Fourier Transform (FFT) pattern. These results indicate that the sample transfer was highly successful, with the stretching direction nearly perpendicular to the zigzag (ZZ) orientation. However, the amorphous contrast visible in the inset of Figure 4.3(e) indicates the presence of unavoidable surface contamination, likely introduced during the dry transfer process.

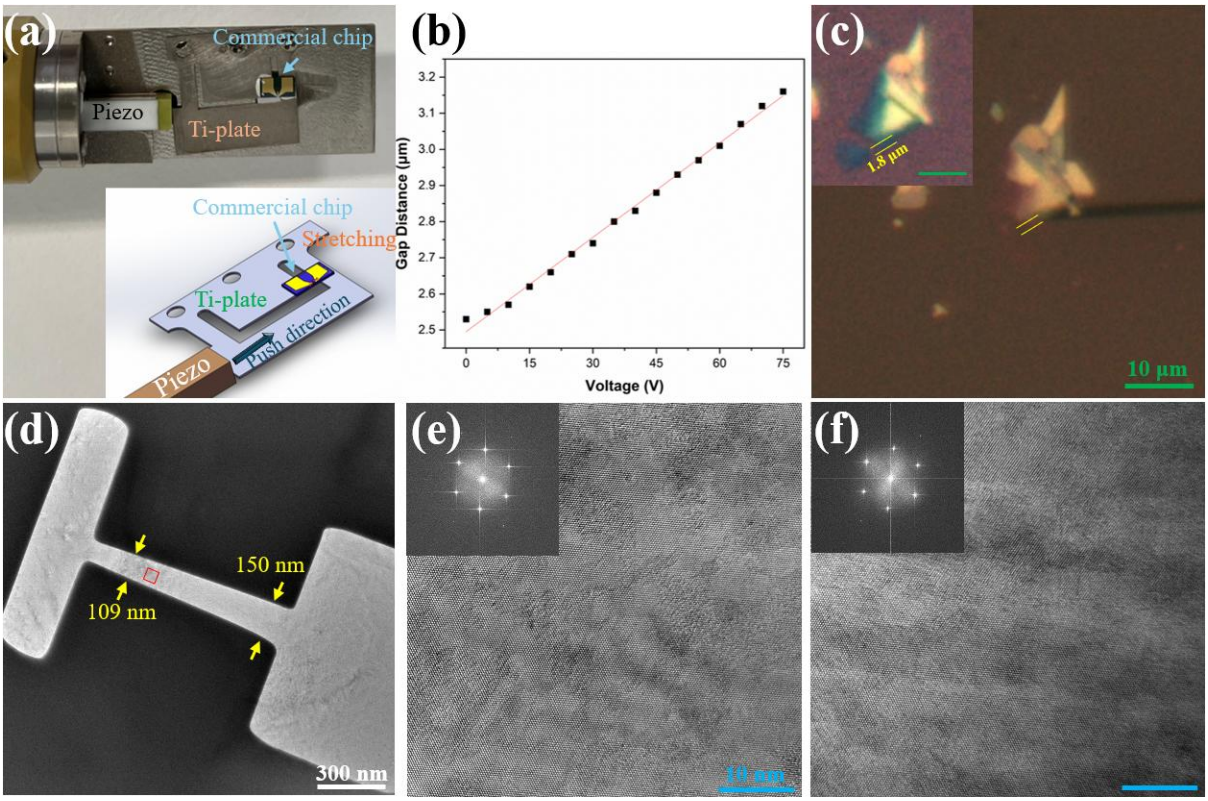

Figure 4.3 (a) Top view of the stretching holder, with an inset showing its 3D model diagram. (b) Linear relationship between the stretching capability of the holder and the applied voltage. (c) MoS_2 flakes before (inset) and after being transferred onto the designed slit. (d) TEM image of the designed stretching gap, with the gap distance indicated. The enlarged region marked by the red rectangle is shown in (e), along with the inserted Fast Fourier Transform (FFT) pattern. (f) MoS_2 flake after pre-strain treatment, along with the inserted Fast Fourier Transform (FFT) pattern.

As shown in Figure 4.3(d), due to the relatively large stretching region (~130 nm in width), it was challenging to accurately locate and capture atomic-resolution images of the crack propagation process during in situ stretching. This difficulty arises from the stochastic nature of crack propagation, which often occurs along one or several random paths within a narrow span of only a few dozen nanometers. To overcome this limitation, a pre-strain treatment was applied prior to the main stretching experiment. This treatment, performed under a carefully controlled strain magnitude of ~8% and without introducing any unexpected damage to the flake, was sufficient to generate local strain concentration regions without fracturing the entire

nanosheet. As a result, pre-cracks were introduced, which served as indicators for potential crack initiation sites. The results showed that the formed strips were concentrated in the middle region of the stretched sheet (see in Figure 4.8). After the pre-strain process, the stretching chip was relaxed to its original state. As shown in Figure 4.3(f), several pre-crack stripes can be observed on the MoS2 nanosheet, which greatly facilitated the identification of target regions for crack propagation observation.

4.3 *In situ* stretching of few-layer MoS_2 nanosheet

4.3.1 TEM results

Figure 4.4(a)–(h) present TEM images illustrating the evolution of a pre-strain-treated multilayer MoS_2 flake under increasing tensile strain. The strain was quantified based on the change in distance between pre-crack stripe No. 2 and pre-crack stripe No. 5, ranging from 0% to 51.58%, ultimately leading to crack formation. Red triangles in Figure 4.4(a) to Figure 4.4(h) mark a fixed reference position, indicating that the entire stretching process was conducted within the same observation area.

Following the pre-strain treatment, five pre-cracks with a spacing of 10 nm or 15 nm (pre-crack 4 and pre-crack 5)—appearing as brighter stripes in contrast (labeled 1 to 5)—were formed, as shown in Figure 4.4(a). These pre-cracks are oriented along the zigzag (ZZ) direction, which forms the maximum angle with the stretching direction. This alignment is consistent with the lower edge energy of the ZZ configuration compared to the armchair (AC)

structure, and the fact that directions more perpendicular to the stretching axis experience greater tensile strain.

The formation of multiple (five) pre-crack stripes indicates that the strain distribution within the flake is non-uniform during the pre-strain process, likely due to the presence of intrinsic vacancy defects commonly found in individual layers. Moreover, the existence of these multiple potential fracture paths suggests that crack propagation is not confined to a single dominant route. Instead, any of these five paths could facilitate crack growth, reflecting a more distributed stress response.

Such a behavior is characteristic of a ductile-like fracture mechanism, where crack initiation and propagation occur in a more progressive and multi-site manner, rather than via a singular, abrupt cleavage as typically seen in brittle materials[1,18]. Furthermore, pre-existing holes (crack nuclei) generated during the pre-strain process were identified and outlined with dashed polygons in different colors, each corresponding to holes within distinct pre-crack stripes. The stretching direction is indicated by the red arrow in Figure 4.4(a). The presence of these holes indicates that the fracture process is not purely brittle. In fact, previous studies have shown that increasing the vacancy defect concentration in front of a crack tip can lead to distinctly different crack propagation behaviors, often associated with more ductile-like fracture mechanisms[1]. In our case, the formation of these defect-induced nuclei under controlled pre-strain suggests a distributed stress response and supports the interpretation of a ductile-like fracture process.

As the tensile strain increased to 2.52% (Figure 4.4(b)), apart from the emergence of a new hole within pre-crack 3, the pre-existing holes expanded in size, The expansion, primarily observed as growth in width along the direction parallel to the ZZ edge, can be attributed to localized strain concentration induced by stretching. This directional expansion is further favored by the lower edge energy of the ZZ configuration compared to AC direction.

At 6.25% tensile strain (Figure 4.4(c)), additional holes (resulting from the localized fracture) appeared within pre-crack 2. Meanwhile, two new holes formed in pre-crack 4, and the dark blue dashed polygons marking holes in pre-crack 3 exhibited a faster growth rate in length compared to those in pre-crack 2.

With the strain increased to 11.57% (Figure 4.4(d)), a crack (crack 3), highlighted by the dark blue dashed line, formed within pre-crack 3 and began propagating through interlayer sliding. Additionally, a noticeable tendency for pre-crack 4 to extend in length was observed. Although the overall propagation direction of crack 3 remained linear, its edge morphology appeared irregular and uneven. This non-smooth crack profile further supports the conclusion that the fracture process is not purely brittle.

At a tensile strain of 14.26% (Figure 4.4(e)), crack 3 continued to widen, while the holes within pre-crack 2 expanded and merged. Meanwhile, pre-crack 4 extended horizontally across the entire image, and the formation of crack 5 within pre-crack 5 was observed, the propagation direction is marked out with a red dashed arrow, originating from the right side of the observation area. This contrasts with cracks 3 and pre-crack 4, which initiated from the left

side. Similar phenomena have also been reported in boron nitride (BN) in another scientific study[6]. As the tensile strain increased to 23.78% (Figure 4.4(f)), crack 3 widened further and pre-crack 2 and pre-crack 5 developed into a crack (crack 2 and crack 5).

The fully formed crack 2 and crack 5 with uneven edges are visible in Figure 4.4(g), 34.33% tensile strain, at which point the fracture structure of the nanosheets was nearly complete, with all cracks aligned along one of the ZZ directions of the nanosheets.

The corresponding TEM image of 51.58% tensile strain is shown in Figure 4.4(h), where the stepped fracture structure is clearly visible and generally arranged parallel to the ZZ structure. The fracture width measured approximately 10.3 nm at the upper edge and 15.0 nm at the lower edge. This significant discrepancy was attributed to the propagation of crack 5, which originated from the opposite end, causing the fracture ribbon between crack 2 and crack 5 to slide. The sliding of the lower part of the fracture edge also explains the upward shift of pre-crack 4. Additionally, the distance from the upper edge of pre-crack 4 to the fracture edge, marked in yellow, remained unchanged in (g) and (h), further supporting this observation (see in Figure 4.8(c)).

The observed stepped structures at the fracture edges suggest that the fracture of few-layer 2H-MoS_2 involves not brittle behavior—an aspect not reported in previous studies. The discrepancy between our results and earlier findings[1,18] is likely due to differences in sample structure, stretching rate, and fracture-inducing methods. Notably, the sample in mentioned report[18] does not have a pure 2H structure. In contrast, our samples are confirmed to be in the

pristine 2H phase, suggesting relatively homogeneous interlayer interactions. This may explain the non-brittle fracture behavior observed in our experiments, as the structural configuration promotes uniform stress distribution and mitigates localized stress concentrations. Furthermore, the stretching rate applied in our study (~0.1 nm/s) is much lower than the 20 nm/s used[18], which also affects fracture dynamics. Additionally, unlike previous study where fracture was induced by electron beam irradiation, our cracks were purely generated by mechanical stretching, avoiding localized, point-like damage.[1]

The in-situ stretching experiment provided intuitive evidence of interlayer fracture in multilayer MoS_2, with fractures occurring at different locations across the layers rather than simultaneously in a single crack. Stepped structures with preferred ZZ edges were observed, clearly demonstrating that the cracks contributing to the fracture did not form at the same time. This emphasizes the necessity of considering interlayer interactions and fracture behaviors in future studies on the mechanical properties of 2D materials.

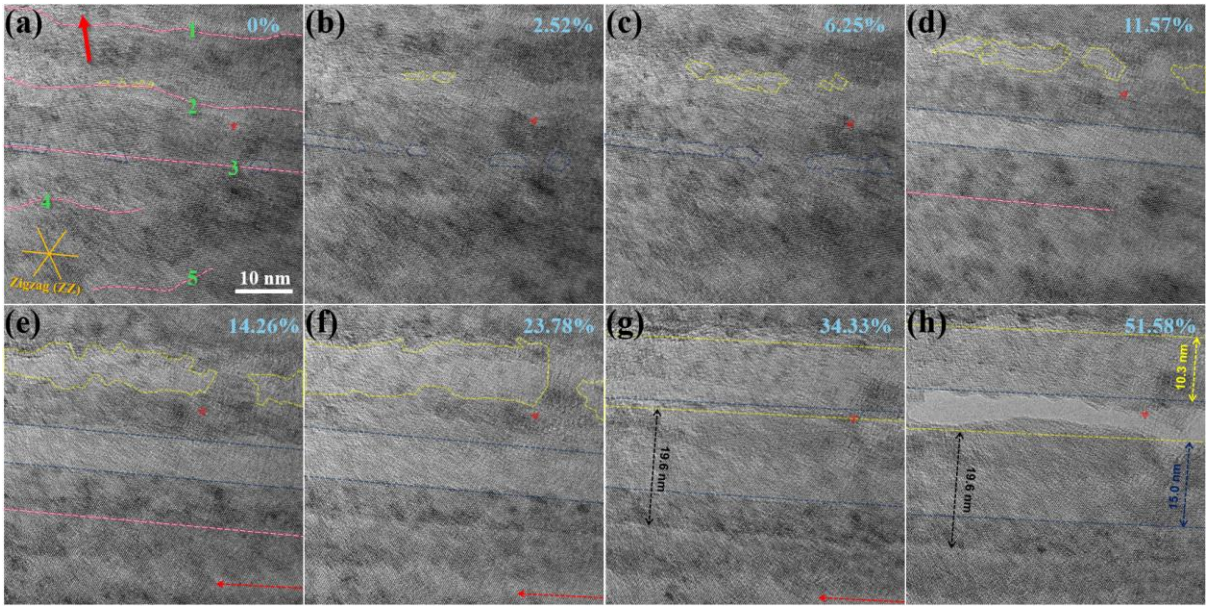

Figure 4.4 TEM images of multilayer MoS_2 under different strain levels: (a) 0%, (b) 2.52%, (c) 6.25%, (d) 11.57%, (e) 14.26%, (f) 23.78%, (g) 34.33%, and (h) 51.58%. In (a), the red arrow indicates the holder's stretching direction, while five stripe-like pre-cracks, labeled 1 to 5 from top to bottom, are marked with pink dashed lines. The dashed arrows in (e), (f), and (g) indicate the direction of crack formation. Dashed polygons, in distinct colors, outline the holes within individual pre-crack area, while dashed straight lines, also in distinct colors, denote the positions of cracks on the respective layers. The red triangle indicates the same reference position under different strain conditions.

To evaluate the strain in each TEM image, we measured the distance variation between the pre-crack stripe 2 to pre-crack stripe 5, as described in Figure 4.5 (a)-(h), each of the distance between the aforementioned was calculated and marked in Figure 4.5 (a)-(h) (unit: nm), respectively. The strain value of Figure 4.5 (a) was set as zero, So that the strain value can be acquire by using the basic strain formular:

$$\varepsilon = \frac{L - L_0}{L} \tag{4-1}$$

In this case, the L_0=32.899 nm and L are the corresponding value measured in (b)-(h), respectively.

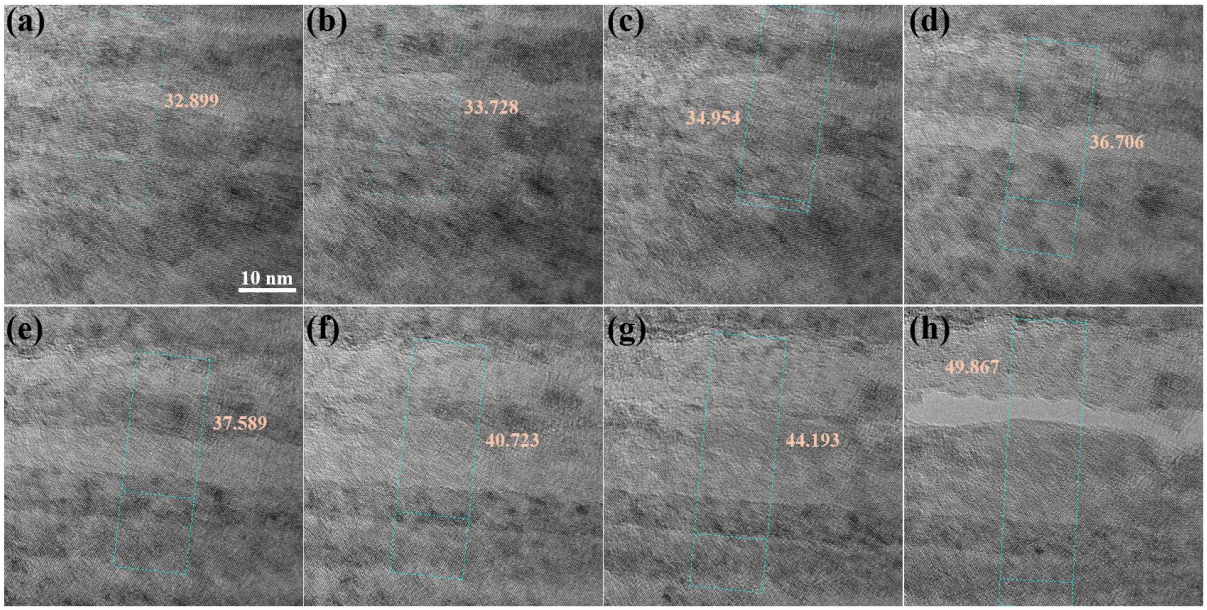

Figure 4.5 The measured distance between the pre-crack stripe 2 and 5 marked respectively. (a)

32.899, (b) 33.728, (c) 34.954, (d)36.706, (e)37.589, (f) 40.723, (g)44.193 nm, and (h)49.867. (unit: nm)

4.3.2 Strain behavior of few-layer MoS_2 nanosheet when stretching

To investigate the strain distribution in few-layer MoS_2 nanosheets under tensile loading, geometric phase analysis (GPA) was performed on TEM images acquired at different strain levels. The corresponding results are presented in Figure 4.6. The corresponding GPA mappings were obtained along the direction perpendicular to the fracture edge orientation (indicated by the yellow arrow in Figure 4.6(a)), as this direction best highlights the trend of stress evolution. In 2D materials, out-of-plane deformation is energetically favored over in-plane distortion, strongly influencing structural modifications[26]. Given that ripple structures preferentially propagate along the AC direction, fringe arrangement changes are more pronounced in this direction[9]. This directional preference makes the selection of the GPA strain reference along the AC direction more reasonable, ensuring a more accurate analysis of deformation characteristics. These results suggest, based on prior understanding, that the homogeneous compression regions likely correspond to out-of-plane deformations, such as ripples, bending, or folding.

As shown in Figure 4.6(a), at 0% tensile strain, following pre-strain treatment and relaxation, despite for a few localized strain concentration points remaining, the overall strain distribution exhibits no distinct transformation boundaries. However, the alternating distribution of tensile and compressive bands parallel to the pre-crack stripes indicates that the relaxation following pre-strain treatment is insufficient to fully release the internal stress within

the nanosheet.

As the tensile strain increases to 2.52% (Figure 4.6(b)), the strain bands become more pronounced, and their spacing decreases—from an initial interval of ~10 nm to ~5 nm. A region of intensified tensile strain emerges between pre-crack stripes 2 and 3, accompanied by localized stress concentration points. In contrast, no significant change in the strain distribution is observed in the area where the hole expands.

As the strain increases to 6.25% (Figure 4.6 (c)), the strain distribution across the image becomes more uniform, while the overall orientation remains parallel to the pre-crack stripes. No significant change is observed in the spacing of the strain bands. Notably, the holes along pre-crack stripes 2 and 3 expand rapidly, which may account for the homogenization of the strain field. Meanwhile, the previously prominent strain band between stripes 2 and 3 becomes less distinct.

At a strain of 11.57% (Figure 4.6 (d)), crack 3 has fully formed and exhibits lateral widening, indicating the onset of interlayer sliding. Simultaneously, the holes within pre-crack stripe 2 expand and coalesce; however, due to severe aberration in the TEM image above stripe 2, the strain distribution in this region cannot be accurately resolved. This limitation persists at higher strain levels, will be discussed in a later section.

Notably, new strain concentration bands emerge along a distinct ZZ direction within crack 3 and extend toward pre-crack stripe 4, with a spacing of ~5 nm. This phenomenon is very interesting, since the ripple-like strain concentration is often attributed to the tensile near the

arrangement of the strain bands,[9] can be ascribed to localized interlayer sliding around crack 3 at this strain. Additionally, the regions adjacent to the strain concentration bands within crack 3 predominantly exhibit compressive strain. The observed strain localization in stripe 4 is likely associated with the continued development of the pre-crack structure in that region.

In the strain distribution map at a tensile strain of 14.26% (Figure 4.6(e)), the strain within crack 3 is predominantly compressive. At this stage, pre-crack stripe 4 has extended across the entire observe area, and a series of strain concentration points appear approximately 5 nm below it, arranged roughly parallel to the direction of the pre-crack stripe. Additionally, the region surrounding crack 5 also exhibits a strain distribution dominated by compression. From this point onward, up to a strain of 51.58% (Figure 4.6(f)–(h)), the overall strain distribution remains consistent with this trend. Notably, the compressive strain in the crack 3 region persists throughout the process until the final fracture occurs. This sustained compressive stress, emerging in the midst of tensile deformation, suggests an irreversible local deformation mechanism likely associated with interlayer sliding or out-of-plane rearrangement.[9,26]

The presence of such compressive strain during crack propagation highlights internal energy dissipation mechanisms—contrary to the sudden and localized bond-breaking typical of brittle fracture. Together with the observed stepped fracture edges and non-linear crack front morphology, these findings strongly support the interpretation that the fracture behavior of few-layer 2H-MoS_2 under our experiment conditions are predominantly ductile-like in nature.

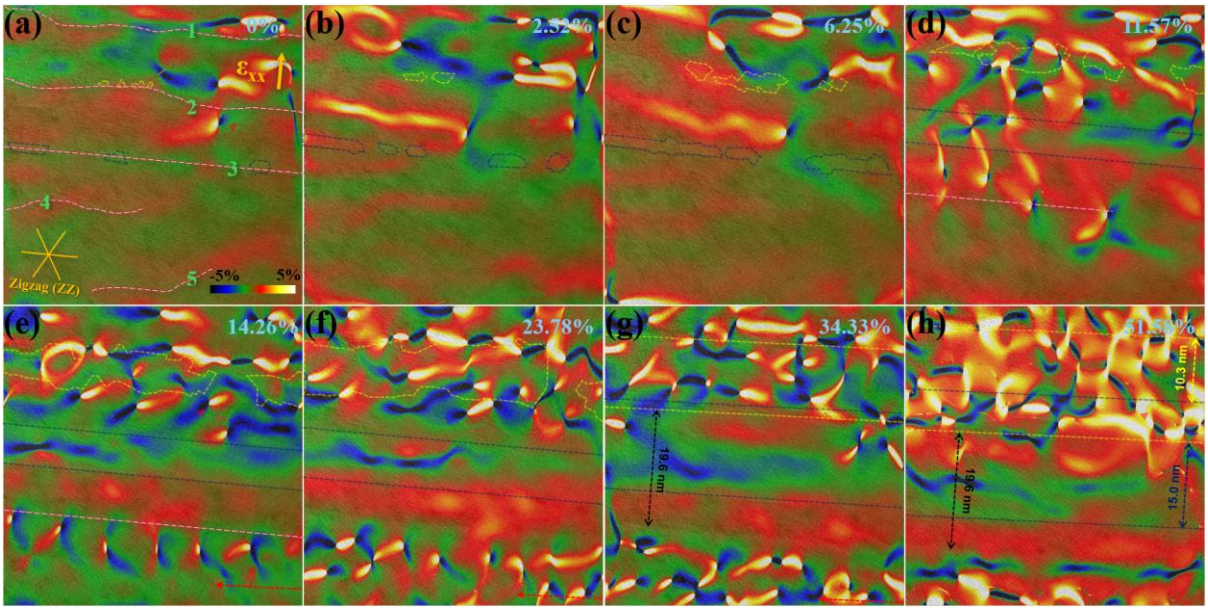

Figure 4.6 Geometric Phase Analysis (GPA) mappings on TEM images of few-layer MoS_2 nanosheet with the strain levels of: (a) 0%, (b) 2.52%, (c) 6.25%, (d) 11.57%, (e) 14.26%, (f) 23.78%, (g) 34.33%, and (h) 51.58%. Along the ε_{xx} direction marked with an orange arrow in (a) and five stripe-like pre-cracks, labeled 1 to 5 from top to bottom, are marked with pink dashed lines. The dashed arrows in (e), (f) and (g) indicate the direction of crack formation. Dashed polygons in distinct colors outline the holes within individual pre-crack, while dashed straight lines, also in distinct colors, mark the positions of cracks on their respective layers. The red triangle serves as a consistent reference point under different strain conditions. All markings accurately correspond to those in the respective TEM images.

4.4 Fracture mechanism approach

To gain deeper insight into the chaotic strain distribution, we examined the fracture edge structure in Figure 4.4(h), with a magnified view presented in Figure 4.7(a). A clear transition from thicker to thinner regions is observed, delineated by the dashed yellow line. Although some atomic-level details are lost due to imaging aberrations, meaningful structural information remains accessible. The TEM image reveals alternating blurry and sharp regions arranged along the ε_{xx}' direction, indicated by the orange arrow in Figure 4.7(a), with an

apparent periodicity of approximately 10 nm. This periodicity corresponds to a full cycle of a sine-like wave, which ideally spans from the middle of the first clear lattice fringe to the middle of the third clear lattice fringe. By tracking three adjacent regions with similar contrast states along the direction of lattice fringe propagation, we can confirm this periodic structure—further supported by the GPA map. However, the lack of complete symmetry information in both principal crystallographic directions may contribute to the observed chaotic strain field. To mitigate this, a spatial mask was applied to selectively extract the lattice fringe information from the well-resolved crystal plane direction, as shown in Figure 4.7(b).

The corresponding strain field derived from Figure 4.7(b), shown in Fig. 5(c), reveals a regular distribution of strain along the fracture edge. Higher tensile strain is localized at concave regions, while lower tensile strain is observed at convex regions. A similar phenomenon—though with an opposite strain distribution—has been reported in previous studies. This discrepancy may be attributed to the different fracture origins: in our case, the edge was generated by tensile failure, whereas in other reports, the edge formation may result from alternative mechanisms such as mechanical exfoliation or irradiation-induced damage.[27]

The formation of this ripple structure is reasonable, given that Poisson's ratio of MoS_2 is reported to lie between 0.2 and 0.44[28,29]. This implies that during uniaxial stretching, stress tends to concentrate in the suspended region of the nanosheet—approximately within half of the total stretched width—which aligns well with our experimental observations, the pre-crack stripes distributed mainly in the stress concentration area (see in Figure 4.8). Moreover, because out-of-plane deformation in two-dimensional materials is generally more energetically

favorable than in-plane deformation[26], This stress concentration is more likely to manifest as a ripple-like morphology, with the ripples preferentially forming along the direction perpendicular to the zigzag (ZZ) edges.[9] In other words, the ripple structure is more likely to form along the two ZZ orientations that are not aligned with the crack propagation direction. Generally, such corrugated structures tend to relax and disappear after crack formation due to stress release. However, in this case, the ripple-like morphology remains visible even after fracture. This persistence may be attributed to the irregular geometry of the crack edges, which helps retain the deformed configuration of the nanosheet.

Based on the above results, we can simply describe the tensile results of the experiment using the model in Figure 4.7 (d). As shown in the figure, during the stretching process, two sets of ripples (lines in distinct colors represent the respectively tensile strain area) with a periodicity of approximately 10 nm and propagate along ZZ arrangement directions intersect at an angle of about 60°. These ripple structures are primarily concentrated near the mid-width region of the stretched nanosheet—approximately at the half-width position—where tensile stress is expected to peak. The yellow arrow indicates the stretching direction. The ripple lines suggest that the structure is under stress, and their intersection marks the location of the highest stress concentration within the strain field.

Therefore, pre-cracks are likely to initiate at the intersections of these corrugated tensile stress fields. Due to the preferential fracture behavior along the ZZ direction, these cracks subsequently propagate along the same orientation. However, in our experimental observations, the spacing between adjacent pre-cracks is approximately twice the period of the tensile strain

ripples. This suggests that interlayer sliding occurs near the pre-crack regions, possibly released local stress over a distance of ~5 nm and thereby promoting crack initiation at intervals of ~10 nm. That is, after the stress-stretched hole appears, the stress concentration at 5 nm nearby is released. This well explains why we can see pre-cracks with a spacing of about 10 nm after pre-strain treatment, and the spacing between pre-crack 4 and pre-crack 5 is about 15 nm.

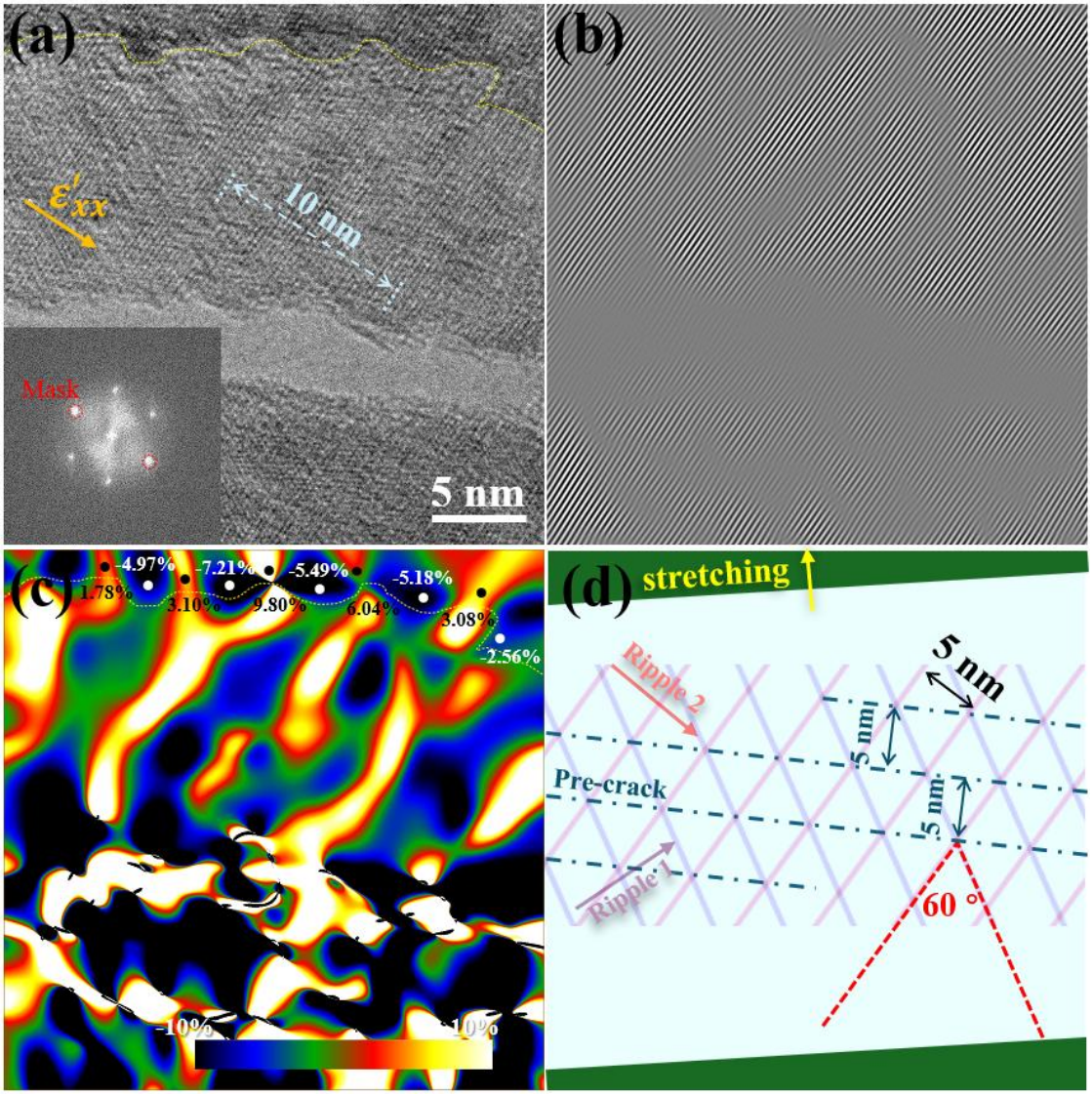

Figure 4.7 (a) TEM image of the fractured edge (indicated by the yellow dashed line) between MoS_2 layers of different thicknesses, with the corresponding FFT pattern inserted in. (b) Lattice fringes obtained by filtering along the marked ε_{xx}' direction. (c) Strain map showing the strain distribution and discrepancies across the region. (d) Schematic illustration of ripple formation in a MoS_2 nanosheet stretched along a direction nearly perpendicular to a zigzag edge, the lines in different colors indicating tensile strain line of

the ripples.

4.5 MoS_2 flake at different stages in TEM

Figure 4.8(a) shows the MoS_2 flake before the pre-strain treatment, where the flake exhibits a homogeneous structure with no noticeable contrast differences. Figures 4.8(b) and 4.8(c) illustrate the gap distance change at the initial stage of the fracture process after pre-strain treatment, from the beginning (b) to the end (c).

In Figure 4.8(b), brighter stripes appear after the pre-strain treatment, corresponding to pre-fractures captured by TEM. The stretching direction for this experiment is indicated by the brown arrow in Figure 4.8(a). In Figure 4.8(c), with the positioning clearly marked, we highlight the observation area of the stretching experiment with dashed square. Additionally, two intersecting fractures, labeled fracture 2 and fracture 5, are directly visible.

A sliding ribbon, further analyzed to explain the inequivalent crack width between fracture 2 and fracture 3, reveals a 4.7 nm discrepancy, which aligns with our amplified TEM results in Fig. 3(h). The presence of this ribbon also supports the observed sliding of crack 4 during the stretching experiment. The fracture edge sizes of these two intersecting cracks were measured and found to be approximately 10.3 nm for both.

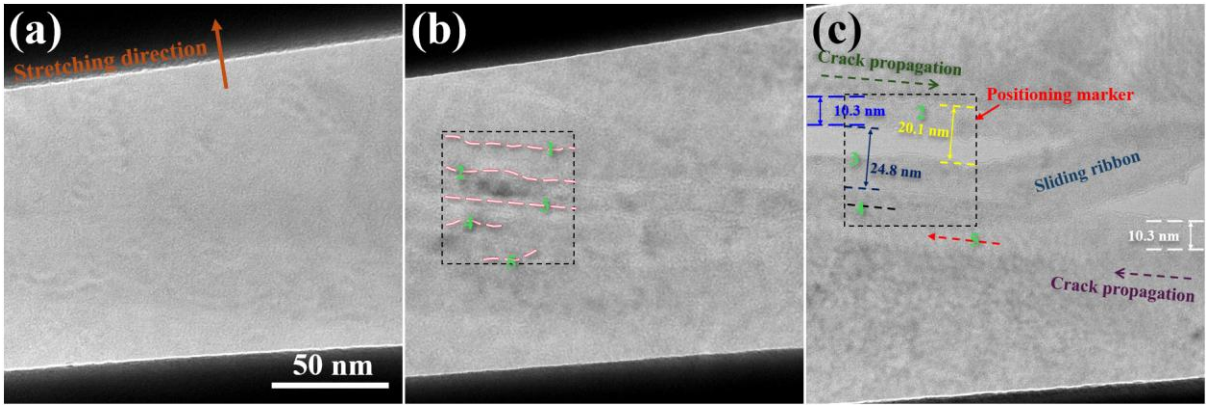

Figure 4.8 (a) MoS_2 flake on the gap before pre-strain treatment. (b) and (c) are the flake after the pre-strain treatment, (b) 0% tensile strain and (c) 51.58% tensile strain, the black dashed square highlights the observation area, the markings add inside the square correspond to those in the respective TEM images.

4.6 Ductile-like fracture in MoS_2 nanosheet with the stretching direction along the zigzag orientation

In addition to the above experiments, we performed in-situ tensile tests on MoS_2 nanosheets along the zigzag (ZZ) crystallographic direction, with the results shown in Figure 4.9. As illustrated in Figure 4.9(a), following tensile deformation along the ZZ direction and the formation of primary cracks, residual nanosheet fragments with significantly reduced thickness can still be observed bridging the gap between the cracked regions. This observation suggests that the fracture process is not purely brittle, and instead, strongly supports the occurrence of interlayer sliding during deformation.

To better illustrate this, the boundaries of regions with distinct thicknesses are highlighted with color-coded lines, while the thinner nanosheet segments that remain connected across the crack are marked in green. The red arrow denotes the stretching direction, and the current frame is taken as the reference state of 0% applied tensile strain.

We then performed geometric phase analysis (GPA) on the TEM image shown in Figure 4.9(a), with the corresponding strain map presented in Figure 4.9(b). In this figure, the yellow arrow indicates the direction of strain measurement, which corresponds to the armchair (AC) orientation of the MoS_2 lattice. All other annotations are consistent with Figure 4.9(a). The strain distribution reveals that regions delineated by lines of different colors exhibit distinct strain characteristics. Specifically, the uppermost region appears predominantly red, indicating significant tensile strain. In contrast, the regions between the yellow and blue lines—particularly the thin bridging nanosheet—primarily show compressive strain, while the areas between the yellow and orange lines, as well as below the blue line, display intermediate strain levels.

Given that the GPA was conducted along the AC direction—where out-of-plane rippling is generally absent—the observed strain contrast can be reliably attributed to variations in atomic spacing, i.e., intrinsic lattice deformation. Furthermore, the spatial correlation between strain distribution and image contrast differences supports the interpretation that regions of different thicknesses exhibit distinct mechanical responses under tensile stress. In particular, the thinner nanosheet segments are more prone to lattice distortion, despite the uniform lattice constant of 2H-MoS_2, reinforcing the notion that thickness plays a critical role in the local strain accommodation behavior.

With increasing strain (Figure 4.9(c)), the sheet exhibited severe plastic deformation, formation of multiple crack paths, and appearance of new holes—all of which are hallmark characteristics of ductile-like fracture. Even up to the point of complete failure, the crack

propagation process remained consistent with ductile-like deformation behavior.

These observations provide compelling evidence that few-layer MoS_2 nanosheets stretched along the ZZ direction can also undergo ductile-like fracture, further corroborating the conclusion that interlayer sliding and thickness-dependent strain localization are critical mechanisms governing the ductile-like response in 2D MoS_2 under tensile loading.

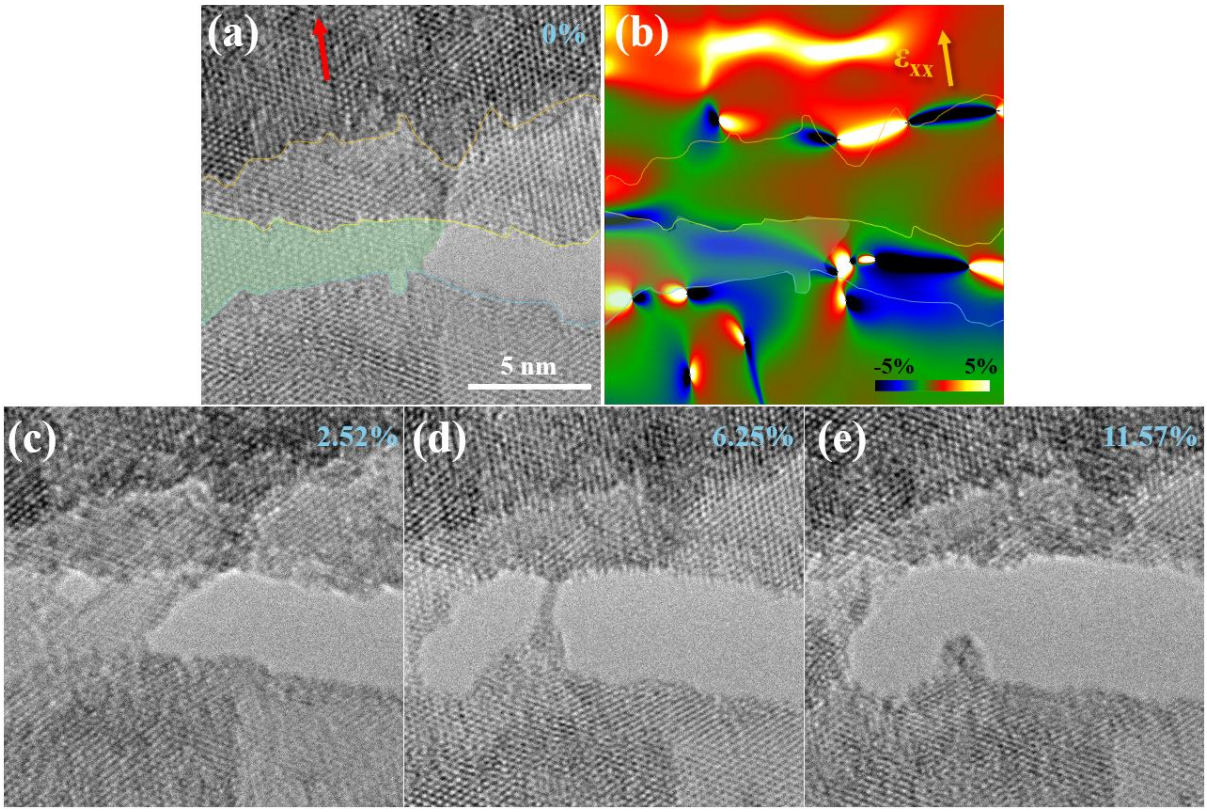

Figure 4.9 TEM images of MoS_2 nanosheet under different strain levels: (a) 0%, (c) 2.52%, (d) 6.25%, and (e) 11.57%. The red arrow indicates the holder's stretching direction, the lines, in distinct colors, outline the positions of cracks on the respective layers. The light green area in (a) marked out the whole suspended nanosheet we observed. (b) Geometric Phase Analysis (GPA) mappings on TEM images of few-layer MoS_2 nanosheet with the strain of (a) 0%. Along the ε_{xx} direction marked with an orange arrow in (a). All markings accurately correspond to the respective TEM image (a).

Conclusion

In this study, we systematically investigated the tensile fracture behavior of few-layer 2H-MoS_2 nanosheets using a custom-designed in situ TEM tensile testing platform, combined with a controlled pre-strain treatment. Our experiments reveal that, unlike previously reported brittle fracture behavior, few-layer MoS_2 exhibits distinct characteristics of ductile-like fracture, including stepped edge morphologies, uneven crack edges, and the presence of compressive strain within the fracture zones. Through geometric phase analysis (GPA), we mapped the strain evolution at various tensile stages, identifying localized strain concentration bands and regions of interlayer sliding that contribute to energy dissipation during fracture.

We discovered that pre-existing holes and pre-fracture stripes, induced by the pre-strain treatment, serve as precursors to crack initiation. The spacing and propagation of these cracks are strongly influenced by ripple-like stress fields formed perpendicular to the ZZ direction—attributable to the Poisson effect and stress redistribution in ultrathin 2D membranes. Additionally, the fracture process showed clear stress modulation patterns, including persistent compressive strain zones near crack tips, which further support a ductile-like mechanism.

Our findings also highlight the ductile-like features in samples stretched along the near AC direction and near ZZ direction at low strain rates. This comprehensive investigation provides new insight into the fracture mechanics of 2D materials and emphasizes the critical role of interlayer interactions and structural imperfections in determining their mechanical resilience.

References

1. Wang, S. *et al.* Atomically Sharp Crack Tips in Monolayer MoS_2 and Their Enhanced Toughness by Vacancy Defects. *ACS Nano* **10**, 9831–9839 (2016).
2. Huang, L. *et al. In Situ* Scanning Transmission Electron Microscopy Observations of Fracture at the Atomic Scale. *Phys. Rev. Lett.* **125**, 246102 (2020).
3. Jung, G. S. *et al.* Interlocking Friction Governs the Mechanical Fracture of Bilayer MoS_2. *ACS Nano* **12**, 3600–3608 (2018).
4. Jiang, J.-W., Park, H. S. & Rabczuk, T. Molecular dynamics simulations of single-layer molybdenum disulphide (MoS_2): Stillinger-Weber parametrization, mechanical properties, and thermal conductivity. *J. Appl. Phys.* **114**, 064307 (2013).
5. Lorenz, T., Joswig, J.-O. & Seifert, G. Stretching and breaking of monolayer MoS_2 —an atomistic simulation. *2D Mater.* **1**, 011007 (2014).
6. Yang, Y. *et al.* Intrinsic toughening and stable crack propagation in hexagonal boron nitride. *Nature* **594**, 57–61 (2021).
7. Xiong, S. & Cao, G. Molecular dynamics simulations of mechanical properties of monolayer MoS_2. *Nanotechnology* **26**, 185705 (2015).
8. Liu, J., Šesták, P., Zhang, Z. & Wu, J. Brittle and ductile behavior in monolayer MoS2. *Mater. Today Nano* **20**, 100245 (2022).
9. Xie, L. & Oshima, Y. Nonlinear mechanical response of rippled MoS2 nanosheets evaluated by in situ transmission electron microscopy. *Appl. Surf. Sci.* **597**, 153708 (2022).
10. Hou, Y. *et al.* Tuning instability in suspended monolayer 2D materials. *Nat. Commun.* **15**,

4033 (2024).

11. Li, P. *et al.* In situ nanomechanical characterization of multi-layer MoS_2 membranes: from intraplanar to interplanar fracture. *Nanoscale* **9**, 9119–9128 (2017).

12. Liu, C., Hongo, K., Maezono, R., Zhang, J. & Oshima, Y. Stiffer Bonding of Armchair Edge in Single-Layer Molybdenum Disulfide Nanoribbons. *Adv. Sci.* 2303477 (2023) doi:10.1002/advs.202303477.

13. Yang, Y. *et al.* Brittle Fracture of 2D $MoSe_2$. *Adv. Mater.* **29**, 1604201 (2017).

14. Cao, C. *et al.* Nonlinear fracture toughness measurement and crack propagation resistance of functionalized graphene multilayers. *Sci. Adv.* **4**, eaao7202 (2018).

15. Li, B. *et al.* Anisotropic Fracture of Two-Dimensional Ta_2 $NiSe_5$. *Nano Lett.* **24**, 6344–6352 (2024).

16. Wang, G. *et al.* Engineering the Crack Structure and Fracture Behavior in Monolayer MoS_2 By Selective Creation of Point Defects. *Adv. Sci.* 2200700 (2022) doi:10.1002/advs.202200700.

17. Ly, T. H., Zhao, J., Cichocka, M. O., Li, L.-J. & Lee, Y. H. Dynamical observations on the crack tip zone and stress corrosion of two-dimensional MoS_2. *Nat. Commun.* **8**, 14116 (2017).

18. Li, P. *et al.* In situ nanomechanical characterization of multi-layer MoS_2 membranes: from intraplanar to interplanar fracture. *Nanoscale* **9**, 9119–9128 (2017).

19. Duan, X., Wang, C., Pan, A., Yu, R. & Duan, X. Two-dimensional transition metal dichalcogenides as atomically thin semiconductors: opportunities and challenges. *Chem. Soc. Rev.* **44**, 8859–8876 (2015).

20. Qi, Z., Cao, P. & Park, H. S. Density functional theory calculation of edge stresses in monolayer MoS $_2$. *J. Appl. Phys.* **114**, 163508 (2013).

21. Guo, Y. *et al.* Distinctive in-Plane Cleavage Behaviors of Two-Dimensional Layered Materials. *ACS Nano* **10**, 8980–8988 (2016).

22. Fang, Z. *et al.* Interlayer Binding Energy of Hexagonal MoS_2 as Determined by an *In Situ* Peeling-to-Fracture Method. *J. Phys. Chem. C* **124**, 23419–23425 (2020).

23. Li, H. *et al.* Rapid and Reliable Thickness Identification of Two-Dimensional Nanosheets Using Optical Microscopy. *ACS Nano* **7**, 10344–10353 (2013).

24. Castellanos-Gomez, A. *et al.* Deterministic transfer of two-dimensional materials by all-dry viscoelastic stamping. *2D Mater.* **1**, 011002 (2014).

25. Li, H. *et al.* From Bulk to Monolayer MoS_2 : Evolution of Raman Scattering. *Adv. Funct. Mater.* **22**, 1385–1390 (2012).

26. Choi, J. S. *et al.* Correlation between micrometer-scale ripple alignment and atomic-scale crystallographic orientation of monolayer graphene. *Sci. Rep.* **4**, (2015).

27. Tinoco, M., Maduro, L., Masaki, M., Okunishi, E. & Conesa-Boj, S. Strain-Dependent Edge Structures in MoS $_2$ Layers. *Nano Lett.* **17**, 7021–7026 (2017).

28. Zhang, C. *et al.* Strain distributions and their influence on electronic structures of WSe2–MoS2 laterally strained heterojunctions. *Nat. Nanotechnol.* **13**, 152–158 (2018).

29. Trainer, D. J. *et al.* The Effects of Atomic-Scale Strain Relaxation on the Electronic Properties of Monolayer MoS_2. *ACS Nano* **13**, 8284–8291 (2019).

Chapter 5 Summary

This thesis presents a comprehensive investigation into the tensile fracture behavior of few-layer 2H-MoS_2 nanosheets, integrating advanced sample preparation, precise mechanical loading, and in situ atomic-scale imaging.

In Chapter 1, we introduced the motivation behind studying mechanical and fracture properties of two-dimensional (2D) materials, emphasizing the importance of MoS_2 due to its tunable bandgap and application potential in flexible electronics. We reviewed current experimental and theoretical methods for stress regulation and crack investigation, pointing out their limitations, particularly the lack of atomic-level insights under controlled uniaxial loading. These gaps shaped the objectives of this work: to develop improved in situ tensile platforms, optimize sample preparation, and explore intrinsic fracture mechanisms.

Chapter 2 detailed the experimental framework and techniques used throughout the study. We described the instrumentation and provided a step-by-step account of MoS_2 sample preparation via modified exfoliation and dry transfer methods. Emphasis was placed on layer-thickness verification, optical contrast calibration, and precise orientation selection, especially the identification of zigzag (ZZ) edges, which are critical for direction-dependent mechanical studies.

In Chapter 3, we designed and validated a novel PTP-based in situ tensile chip that

addressed the shortcomings of earlier designs. By replacing deformable titanium support plates with a connected Si chip frame incorporating SiN_x windows and long-narrow gaps, we achieved stable, uniform deformation with sub-micron resolution. We evaluated several stress localization strategies and confirmed the effectiveness of the final design through finite element simulations and successful atomic-resolution imaging, establishing a reliable platform for high-precision fracture testing.

Chapter 4 presented our main findings on the tensile fracture behavior of few-layer MoS_2. Contrary to the traditionally reported brittle failure, our results revealed ductile-like characteristics—including stepped and uneven crack edges, localized strain bands, and persistent compressive zones—particularly under low strain rates along the ZZ and near-AC directions. Pre-strain treatments introduced ripple-like stress fields and defect precursors, which influenced crack initiation and propagation. These observations underscore the role of interlayer sliding, stress redistribution, and structural inhomogeneity in enhancing energy dissipation and mechanical resilience.

Together, these studies offer new insights into the fracture mechanics of 2D materials and provide a robust experimental foundation for future exploration of atomistic failure processes in layered systems.

Acknowledgements

First and foremost, I would like to express my sincere gratitude to my advisor, Professor Yoshifumi Oshima. His insightful design of the tensile chip played a pivotal role in the successful implementation and advancement of this study. From the early conceptual stages to the continual refinement of the experimental platform, Professor Yoshifumi Oshima provided invaluable guidance that laid the foundation for this work. His rigorous academic attitude, deep expertise, and sharp scientific insight not only shaped the direction of this research but also greatly enriched my thinking and problem-solving abilities. Throughout the project, his encouragement and dedicated mentorship have been a constant source of motivation for me.

I would also like to thank my senior colleagues Chen Tongmin, Xie Lilin, Zhang Jiaqi and our lab's lecturer Kohei, Aso for their invaluable support throughout my experimental work. Whether it was Xie's assistance with experimental construction and his unreserved sharing of theoretical knowledge, Chen's patient and reliable guidance during technical challenges, or Zhang's thoughtful input that helped shape my experimental thinking—all of their support was indispensable.

I am equally grateful to my classmate Chen Limi for her help with experimental techniques, and to Xu Yuanzhe and Liu Xiaopeng for their encouragement and assistance, which helped ease the pressure during critical moments of this project.

Special thanks go to my friends Liu Ruian and Hu Jiali, who provided me with very valuable test results and offered crucial help in the course of my experiments. Their support significantly contributed to the success of this work.

My thanks also go to my friends Tang Bowen, Yuan Lishuai, Gao Xiangjie, Ma Yingshu, Gelan, Zhang Yuanhao, Sun Haoran, Xu Guojuan and Lu Yufeng, for encouraging me and giving me the motivation to move forward when I was struggling. They not only provided emotional support but also shared valuable life experiences and broadened my horizons by introducing me to many new ideas and perspectives.

I would like to extend my sincere thanks to my minor research supervisor, Professor Goro Mizutani, for his rigorous academic attitude and thoughtful guidance throughout the research process. His careful feedback and consistent encouragement have deeply influenced the way I approach scientific problems, and I have benefited greatly from his mentorship.

Finally, I would like to express my deepest gratitude to my parents and my brother for their unconditional support and understanding, especially for the sacrifices they have made to support my education. As someone pursuing a Ph.D. at a relatively advanced age, I often feel ashamed of continuing to rely on them financially and emotionally. I regret not being able to give back as much as I should have, and I am truly sorry for having asked so much while offering so little in return. Their love and patience have been my strongest source of strength, and I hope to make them proud one day.

List of publications

1. Xiong, Wei, Xie, Lilin, and Oshima, Yoshifumi. Development of an in-situ TEM method for elucidating tensile fracture processes of 2D materials at atomic scale. *Jpn. J. Appl. Phys.* (2025) doi:10.35848/1347-4065/ade945.

2. Xiong, Wei, Xie, Lilin, and Oshima, Yoshifumi. “Thinning-toughening mechanism of the fracture in MoS_2” (preparing)

Presentation

- International Conference (Poster)

1. Wei Xiong, Limi Chen, Lilin Xie, Kohei Aso and Yoshifumi Oshima, “Precise measurement of ripple structure of MoS_2 nanoribbon when stretching”, 20th International Microscopy Congress (IMC20), 10-15 September 2023, Korea

- Domestic Conference

1. Wei Xiong, Lilin Xie and Yoshifumi Oshima, “Ripple structure of MoS_2 nanosheets evaluated by in situ stretching transmission electron microscopy”, 9th International Symposium on Organic and Inorganic Electronic Materials and Related Nanotechnologies, 5-8 June 2023, Ishikawa. (Oral)

2. Wei Xiong, Limi Chen, Lilin Xie, Kohei Aso and Yoshifumi Oshima, “Precise measurement of ripple structure of MoS_2 nanoribbon when stretching”, JAIST International symposium of Nano-Materials for Novel Devices, 11-12 January 2024, Ishikawa. (Poster)

3. Wei Xiong, Lilin Xie and Yoshifumi Oshima, “Interlayer fracture of multilayer MoS_2 evaluated by in situ transmission electron microscopy”, 10th International Symposium on Organic and Inorganic Electronic Materials and Related Nanotechnologies, 11-14 June 2025, Fukui. (Poster)